Delft University of Technology

Towards intrinsically safe microstructures in resistant spot welded advanced and ultra high strength automotive steels

Eftekharimilani, Parisa

Important note
To cite this publication, please use the final published version (if applicable).
Please check the document version above.

Towards intrinsically safe microstructures

in resistant spot welded advanced and ultra
high strength automotive steels

Parisa Eftekharimilani

Towards intrinsically safe microstructures in resistant spot welded advanced and ultra high strength automotive steels

Parisa Eftekharimilani

Towards intrinsically safe microstructures in resistant spot welded advanced and ultra high strength automotive steels

Dissertation

For the purpose of obtaining the degree of doctor
At Delft University of Technology,
By the authority of the Rector Magnificus Prof.dr.ir. T.H.J.J. van der Hagen
Chair of the Board for Doctorates,
To be defended publicly on
Wednesday 2nd October 2019 at 15:00

by

Parisa Eftekharimilani
Master of Science in Metallurgy and Materials Engineering,
University of Tehran, Tehran, Iran
Born in Tabriz, Iran

An electronic version of this dissertation is available at:
http://repository.tudelft.nl

To Maryam Mirzakhani and
All the inspiring women in my life.

Table of contents

CHAPTER 1

Introduction

1.1 Introduction

The emission of CO_2 and other particulates from vehicles is a major issue for global warming. The automotive industry needs to reduce the CO_2 emissions of vehicles, which drives the necessity for weight reduction [1]. Weight reduction can be obtained by using lighter materials and/or increasing the strength of the materials, which allows thinner sections to be used. Crash worthiness for passenger safety is another important aspect to be considered in automotive design. For each location in a car body, the most suitable steels are selected to optimise passenger safety.

Novel key materials for the design and production of light-weight car body structures are Advanced High Strength Steels (AHSSs). These steels offer high strength and ductility combinations compared with conventional steels. Based on their microstructural aspects AHSSs are classified as Dual Phase steels, Complex phase steels, Martensitic steels, Transformation-Induced Plasticity steels, Twining-Induced Plasticity steels, Quench and Partitioning steels or Boron-based hot-formed steels. A modern body-in-white (*i.e.* the body shell of a vehicle before component assembly or painting) is composed of a wide variety of these AHSSs, as shown in Fig. 1.1 [2].

The components of the car body-in-white need to be joined. Resistance spot welding (RSW) is the predominant joining technique in the automotive industry. A typical vehicle contains between 2000-4000 spot welds [3].

In the RSW process applied to steel sheets, the parts to be joined are mechanically pressed together by two electrodes and an electric current is passed through the faying sheets. Joule heating is generated specifically at the interface of the two sheets, where melting occurs, forming a weld pool. When the electric current is switched off, the weld pool solidifies and a resistance spot welded joint is produced. A typical RSW process involves a mechanically constrained thermal cycle with heating and cooling rates in the order of 1000-5000 Ks^{-1}. The vehicle safety is to a large extent controlled by the performance of these resistance spot welds. A major concern regarding the performance of spot welds in AHSSs is the susceptibility to weld metal failure, referred to as interfacial or partial interfacial failure. The AHSSs are more susceptible to this unfavourable failure mode than conventional mild steels, due to their relatively high alloying levels. In addition, for AHSS welds, relatively low mechanical strength levels are often reported [4, 5]. For the introduction of these new steel grades issues regarding the poor mechanical performance of the welds need to be overcome.

The key question is how to obtain intrinsically safe microstructures and therefore improved mechanical performance of the AHSSs welds. To be able to answer this, the complex relationships between processing conditions, the materials response to the thermal-mechanical cycle imposed and the final mechanical properties of the weld should be established.
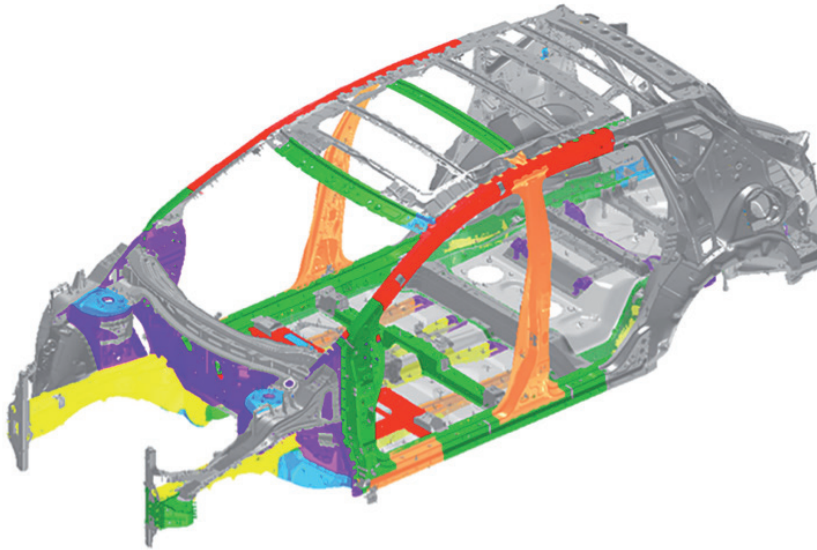
COLOR	MPa	
🟥	1180	COMPLEX PHASE (MARTENSITE+FERRITE+BAINITE+RETAINED AUSTENITE)
🟧	980	DUAL PHASE (MARTENSITE+FERRITE)
🟨	780	DUAL PHASE (MARTENSITE+FERRITE)
🟩	590	DUAL PHASE (MARTENSITE+FERRITE)
🟦	440	QUASI HIGH STRENGTH
🟪	390	QUASI HIGH STRENGTH
⬜	MILD	SHOWN IN GREY (IN PICTURE) SHOWN IN WHITE (ON DISPLAY VEHICLE)

Fig. 1.1. A representation of the materials to be used in the body-in-white of the Nissan Murano [2].
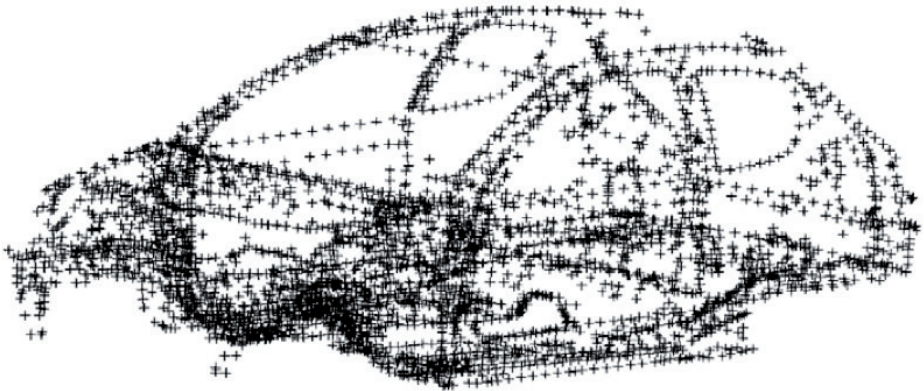
Fig. 1.2. Resistance spot welds in a body in white structure [3].

A characterisation of the as-received material is required. This includes the chemical composition of the steel, the as-received microstructure and the mechanical properties. A second important aspect is the characterisation of the welding process. Process parameters have to be selected to generate an appropriate weld, according to standards [6]. Electrode force, welding current and weld and hold times are the key parameters, that determine the creation of the weld.

The material to be welded is subjected to a thermal-mechanical cycle. The localised heating creates a weld pool, which starts to solidify when the current is switched off. During solidification the solid grains grow in the direction of the maximum temperature gradient and elemental segregation can take place. Upon further cooling solid-state phase transformations occur, affected by the cooling rate and the load applied by the electrodes. As steep temperature gradients exist over the weld region, a heterogeneous microstructure is to be expected. The mechanical performance is determined by the combined effect of the base material properties, the weld geometry, and the weld and HAZ microstructures.

Another aspect to be considered is the introduction of stresses during the welding process. The thermal-mechanical cycle will cause localised expansion and contraction. Volume changes also occur as a result of solid-state phase transformations and local plastic deformation. The indentation of the electrodes in combination with the low yield strength at elevated temperatures has a large influence on the development of plastic strains. When a weld has cooled to room temperature residual stresses are inevitably present in the component.

The combined effect of microstructural characteristics and the residual stress field determine the mechanical performance of the weld. In the automotive industry, a number of standard tests [6] are available to test the performance of resistance spot welds, including the Cross Tension Strength (CTS) test and the Tensile Shear Strength (TSS) test.

In this investigation, strategies to improve the mechanical performance of resistant spot welds in advanced high strength steels are considered. Applying a second welding current pulse in the welding sequence may result in microstructural improvements, as it acts as a heat treatment on the already solidified weld metal and the heat affected zone. Furthermore, the effect of a post weld heat treatment, *i.e.* a paint bake cycle is addressed. Such a thermal cycle is in general used for curing the paint on a body-in-white; however strength improvements of welds are also reported due to this cycle [7], although the reason for this improvement is not mentioned in the literature.

1.2 Research objective and approach

The aim of this research is to understand the underlying mechanisms of microstructural evolution in advanced high strength steels under the extreme thermal and mechanical conditions that prevail during resistance spot welding. This understanding permits the development of new strategies to achieve intrinsically safe microstructures and improved mechanical performance of welds in advanced high strength steels.

To achieve this aim, the following approach is pursued:

The current work focuses on a new generation 1 GPa AHSS CR700Y980T-DH-GI according to VDA 293-100 norm [8], with a sheet thickness of 1.3 mm. The steel is received in a cold-rolled and galvanised condition. A conventional resistance spot weld of this steel shows weld metal failure during mechanical testing. In order to improve the mechanical performance of the CR700Y980T-DH-GI resistance spot welds, alternative welding schedules are applied to modify the microstructure of the welds.

To further improve mechanical behaviour, the application of a typical paint baking cycle after welding is also considered and the effects on the microstructure and the mechanical performance of the welds are studied. Furthermore, the fracture toughness of a thin sheet AHSS after a baking cycle is assessed.

The localised heating and subsequent cooling and simultaneous plastic deformation will introduce residual stresses in the welds and affect their mechanical performance. In order to better understand the process, a finite element model is employed to predict the temperature and stress evolution during welding. This model makes it possible to calculate the effects of welding conditions on the thermal and the stress fields in and around the welded area.

The melting and solidification, segregation, solid-state phase transformations and the plastic deformation as a result of the load applied play a role in the final microstructure and the mechanical performance of the spot welds. The effect of mechanical loading on the solid-state phase transformations of the steel is also studied.

1.3 Outline of the thesis

Chapter 2 provides an introduction to the developments of advanced high strength steels (AHSSs), the resistance spot welding (RSW) process and microstructures and mechanical properties of the welds. The main issues concerning the resistance spot weldability of these steels are failure behaviour and reduction in mechanical strength of the welds. During cross-tension strength testing of these welds, the crack can easily propagate through the weld causing brittle weld metal failure.

Chapter 3 contains an overview of the techniques applied to characterise the base material and weld metal and detailed experimental procedures employed to study the microstructure, mechanical behaviour and residual stress. The details of various welding sequences are provided in this chapter. Furthermore, the modelling approach to obtain the temperature and residual stresses distribution is presented.

Based on the literature review in chapter 2, double pulse welding schemes were examined to improve the mechanical behaviour of the AHSS spot welds. The effect of double pulse welding on the microstructure, elemental distribution and the mechanical response of the welds is discussed in chapter 4. Electron probe microanalysis (EPMA) and electron backscattered diffraction (EBSD) are used to study the elemental distribution and the microstructures of the welds. Mechanical tests such as cross tension strength and tensile shear strength tests are employed to evaluate the mechanical response of the welds.

Chapter 5 focuses on the effect of a paint bake cycle on the microstructure and the mechanical performance of the single and double pulse welds. TEM analyses are used to study the weld microstructures. The studies include an assessment of the fracture toughness of the martensitic and tempered martensitic microstructures.

In chapter 6, an evaluation of the residual stress of the welds discussed in chapter 4 and 5 based on synchrotron X-ray diffraction measurements is given. Results from a finite element model, validated by the measured residual stresses are also presented in this chapter. In addition, results from FIB ring-core measurements of the local residual stress at the weld edge are reported.

The mechanical loading by electrodes in resistance spot welding can affect the solid-state phase transformations during cooling. A study of the effect of plastic and elastic mechanical loading on the FCC to BCC phase transformations in an AHSS during cooling, using an *in-situ* synchrotron diffraction technique, is presented in chapter 7. Changes in martensite start temperature, phase transformation kinetics and retained austenite volume fraction and morphology are discussed.

In chapter 8, the most important aspects of this research are drawn together in a summary and general discussion. Finally, the conclusions of this research and suggestion for the future work are presented in chapter 9.

References

[1]   Regulation (EU) No 333/2014 of the European Parliament and of the Council of 11 March 2014: *Amending Regulation (EC) No 443/2009 to define the modalities for reaching the 2020 target to reduce CO_2 emissions from new passenger cars* (2014).

[2]   D. Coakley, *2015 Nissan Murano*, Great designs in steel seminar (2015) www.autosteel.org.

[3]   F. Rossillon, *Influence des conditions de soudage sur le comportement en fatigue d'un acier THR Dual Phase soudé par point*, PhD Thesis, Université Blaise Pascal–Clermont II (2007).

[4]   S. Furusako, G. Murayama, H. Oikawa, T. Nose, F. Watanabe, H. Hamatani, Y. Takahashi, *Current Problems and the Answer Techniques in Welding Technique of Auto Bodies (First Part)* - Nippon Steel Technical Report 103 (2013) 69-75.

[5]   H. Oikawa, G. Murayama, T. Sakiyama, Y. Takahashi, T. Ishikawa: *Shinnittetsu Giho* 385 (2006) 36.

[6]   SEP 1220-2*: Testing and documentation guideline for the joinability of thin sheet of steel-part 2: resistance spot welding* Technical report 08 VDEh standard (2007).

[7]   Nick den Uijl, Toru Okada, Sullivan Smith, Masato Uchihara, Kiyoyuchi Fukui, *The effect of paint baking cycles on the spot weld strength of AHSS and consequences for testing procedures*, 8th International Symposium of Japan Welding Society, Kyoto, Japan (2008).

[8]   VDA 239-100 Material specification: *Sheet Steel for Cold Forming* (2016).

CHAPTER 2

2

Background

2.1 Developments in Advanced High Strength Steels

The demand for the development of lighter, safer, greener and more cost-effective vehicles leads to continued development of advanced high strength steels (AHSSs) that meet functional requirements on strength and formability. The total elongation versus the ultimate tensile strength for various types of steels is shown in Fig. 2.1. In this figure, three generations of AHSSs are indicated. The first generation has a typically martensitic microstructure, with one or more additional phases to improve the formability. The most commonly used AHSSs in this class is dual phase steel, which contains martensitic and ferritic phases to balance strength and formability. Complex phase steels, transformation-induced plasticity (TRIP) steels, martensitic steels and press hardened steels (also referred to as hot stamped steels) are included in this category. These classifications are based on metallurgical aspects and heat treatments applied during production [1].

The second generation AHSSs includes austenitic stainless steels, twinning-induced plasticity steels and lighter weight steels with induced plasticity. These steels show higher strength and formability compared to first generation AHSSs, but are relatively expensive due to their high cost alloying elements. As a result, demand has grown for a new generation of steels; *i.e.* 3rd generation AHSSs that have high formability and strength at a reasonable cost [1].

The 3rd generation AHSSs allow further weight reduction and provide good crashworthiness for automotive applications; they achieve their properties as a result of a careful selection of alloying elements and complex heat treatments. In these steels, the required properties are achieved by means of multi-phase microstructures. Although several alloying strategies for these steels exist, most of them have relatively high levels of carbon, manganese and/or silicon. Quenching and partitioning steels, TRIP assisted bainitic ferrite steels, TRIP assisted dual phase steels and Nano steels belong to this category [1-3].

Unfortunately, the relatively high amount of alloying elements have led to challenges during the welding of these 3rd generation steels. Undesirable microstructural changes, high residual stresses and crack formation are some of the issues affecting mechanical performance that need to be addressed [1].

2.2 Resistance Spot Welding Process

Resistance spot welding (RSW) was invented by Elihu Thomson in 1890 [4]. RSW is by far the most widely used joining method in the automotive industry due to the high operating speeds, low costs, the reliability of the process and the suitability for
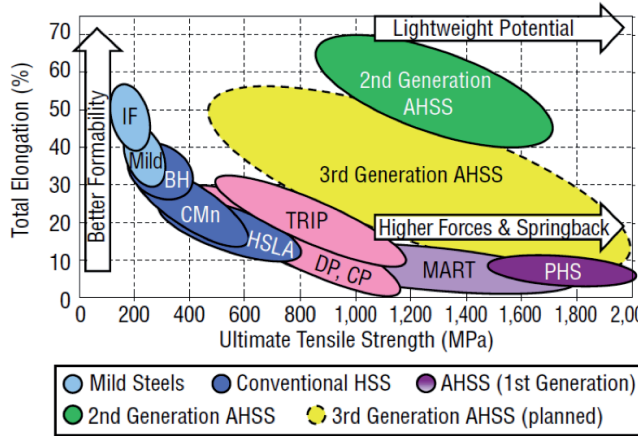
Fig. 2.1 Total elongation versus the ultimate tensile strength, for three generations of automotive steels [1].

automation [5–7]. RSW involves a complex interaction of the thermal, electrical and mechanical phenomena of the welding process as well as physical and metallurgical properties of the material to be welded. RSW is a fusion welding process in which heat is generated as a resistance to the flow of an electrical current. To ensure sufficient contact between the material parts being welded, a pressure is applied by two water-cooled electrodes. The physical principal for obtaining heat generation is defined by Joule's law, expressed by Eq. 2.1 [8-11]:

$$Q = RI^2 t$$
$$R = \sum_1^7 R_i \, ,$$
$$R_i = \frac{\rho_i L}{A} \, , \qquad\qquad\qquad\qquad \text{(Eq. 2.1)}$$

where Q is the amount of heat generated during the welding cycle, I is the applied current, R is the electrical resistance, t is the time over which the current is applied, $\sum_1^7 R_i$ refers to the sum of the resistances in different locations, ρ is electrical resistivity, L is the length and A is the cross sectioned area.

A schematic representation of RSW and various resistances as well as trends of electrical resistance and temperature in various components is shown in Fig. 2.2. The bulk resistance of the electrodes and the metal sheets (R_1, R_3, R_5 and R_7) and the sheet-sheet and sheet-electrode contact resistances (R_2, R_4 and R_6) add up to the entire resistance and all vary with temperature. Thus, the heat generated by the current flow is not uniform and the highest resistance and therefore the heating is obtained at the interface between the two metal sheets, where a weld pool is formed.
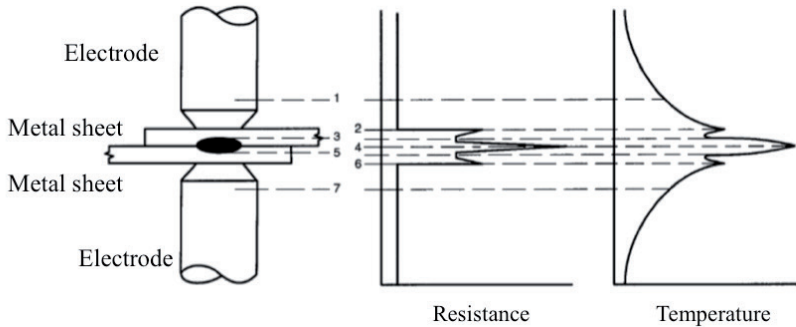
Fig. 2.2 Schematic representation of RSW set up and various existing resistances as well as trends of electrical resistance and temperature in various components. *R1* and *R7* refer to the resistance of electrodes, *R3* and *R5* refer to the resistance of the metal sheets and *R2*, *R4* and *R6* are contact resistances [12].

Due to the low electrical resistivity of copper, it is normally used as the material for the electrodes. These electrodes can conduct high currents to the metal parts without considerable Joule heating. The copper electrodes are water cooled to avoid fusion at the electrode-workpiece interface by the dissipation of heat generated at these locations [11].

A schematic overview of the RSW process sequence is shown in Fig. 2.3. Four stages during RSW can be identified. In the 'squeeze' time, the metal parts are pressed together mechanically by the force applied by the electrodes. In the 'weld' stage, the electrical current is passed through the faying interface resulting in melting and formation of a weld pool at the interface, as the resistance is highest (R_4) (Fig. 2.2). During the 'hold' time, the current is switched off. The heat is dissipated from the interface thereby reducing the temperature; typically, the cooling rates are high, in the order of 2000–4000 Ks^{-1} [2]. The weld pool solidifies and a weld nugget is produced. Finally, in the 'off' time, the electrodes are released.

The most important welding parameters include squeeze time, welding current, electrode force, welding time, holding time and the electrode geometry. The welding current, welding time and electrode force must be such that a weld nugget is formed.

The thickness of the sheets to be welded is an important parameter in assessing the resistance spot welds. The minimum accepted weld nugget size is 4√t (t is the sheet thickness) according to the VDEh testing and documentation guideline for the joinability of thin sheet steel [14]. In thick metal sheets, there will be more bulk material that conducts the heat away from the weld. More energy, *i.e.* a higher welding current, is required for the weld formation.

One of the complications of RSW is shunting. When multiple welds are made on the same sheets, the previous welds will function as short circuits (Fig. 2.4). At the required location of the weld to be made, the current will remain relatively small. Thus, higher
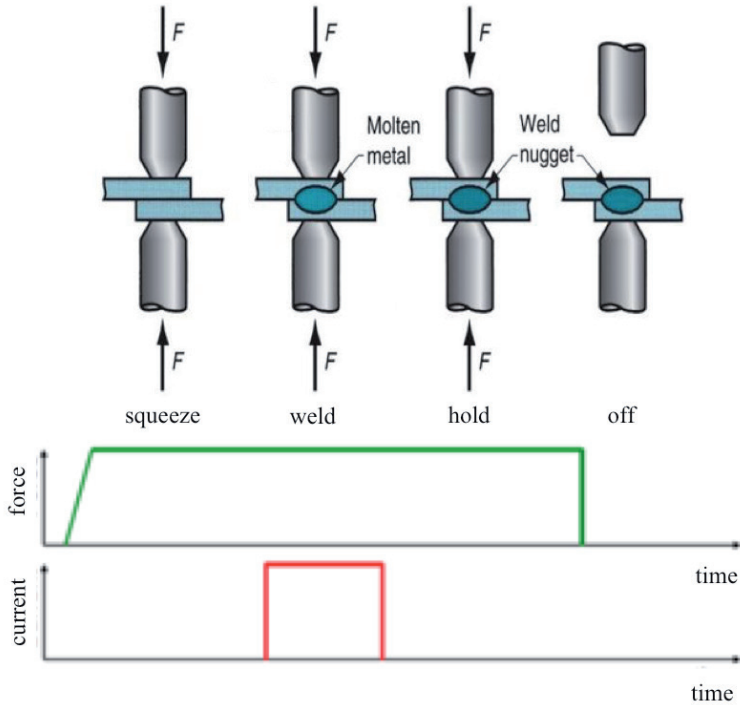
Fig. 2.3 Schematic of the resistance spot welding process, and the force and current time scheme [13].
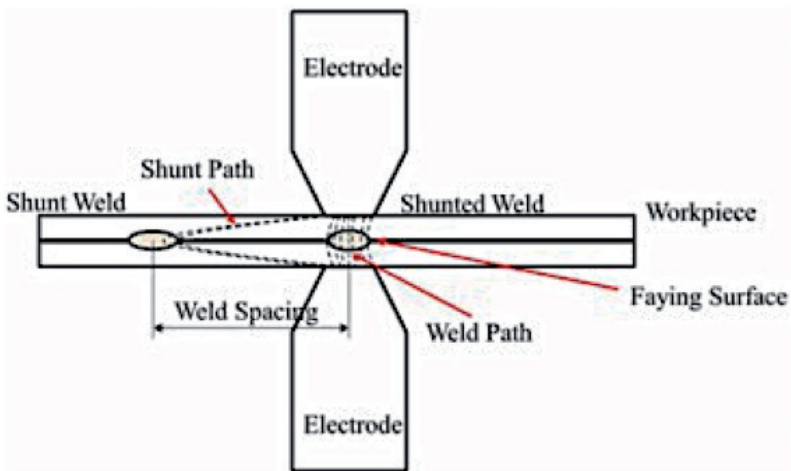
Fig. 2.4 Schematic representation of shunting in resistance spot welding [16].

current and/or longer time will be required to obtain the same size of weld [15]. The minimum reliable distance between two steel spot welds to avoid shunting is about 40 mm [14].
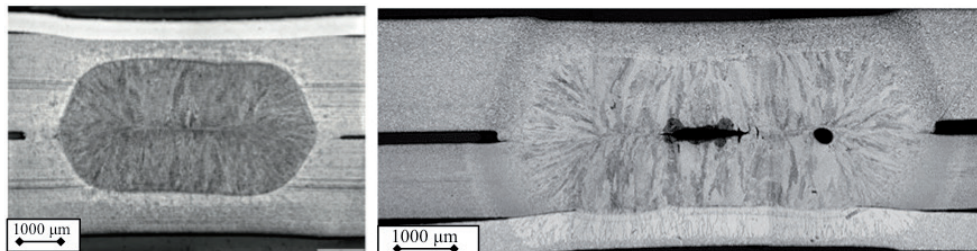
Fig. 2.5 Micrograph of a resistance spot weld of 3 sheets [17, 18].

In case of welding sheets with dissimilar thickness, the heat conducted away from the interfaces of the electrodes will be different for both sheets. The thinner sheet will melt preferentially, whereas the thicker sheet acts as a heat sink and melting is limited. Eventually, melting may occur in only one of the sheets and a weld between the two sheets will not be formed.

If the sheets to be welded have dissimilar materials, the electrical and thermal properties of the sheets are different and the thermal profile will vary in a similar manner to that described for different sheet thickness. Fig. 2.5 shows the cross section of a resistance spot weld of three sheets with different material and sheet thicknesses. RSW of more than two sheets makes welding more complicated as shown in Fig. 2.5 due to the differences in electrical and thermal properties of the sheets; cavities may be formed [17].

The surface of sheet metal used in the automotive industry is often coated. The coating affects the contact surface resistance. Zinc is the most common material for coating of automotive metal sheets. The electrical conductivity of the zinc coated sheet is higher than an uncoated sheet, therefore the interface resistance (R_4) reduces and a higher current and/or longer time should be applied for the welding of the zinc coated facing sheets [19].

The wear of the electrode tip is another issue that should be addressed in RSW. It leads to larger electrode tip and sheet contact, which decreases the current density and affects the nugget size obtained [9, 19]. The quality of the electrode tip after a certain number of welds can be improved by redressing, which is mechanical milling of the electrode tip to achieve its original geometry [20].

The quality of welds can be characterised by a number of parameters. The parameters considered include weld nugget size, electrode indentation, surface appearance porosity and/or voids and cracks [21]. Specific combinations of welding time and welding current define a weldability range, where appropriate welds can be achieved. Fig. 2.6 a and b show schematics of a weld nugget growth curve and a weldability range diagram, respectively. As shown in Fig. 2.6 a, at a constant weld time, a certain minimum current should be applied to form the minimum acceptable nugget size. If the current becomes
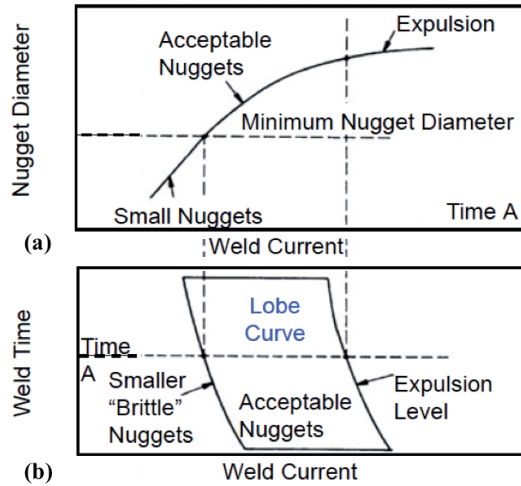
Fig. 2.6 Weld nugget growth curve and weldability range, (a) shows the change in nugget diameter as a function of the welding current for a fixed weld time A; indicating the optimal current range and (b) indicates how the required current range shifts when the weld time is varied [23].

too large and exceeds a threshold, expulsion or splashing will occur. Such splashes can lead to large cavities in the weld, and as a result, the load bearing capacity of the weld is reduced. Moreover, expulsion of molten metal causes a deep indentation at the metal surface, which decreases the metal thickness, resulting in diminishing the load bearing capacity of the weld. Welds that are obtained between the minimum acceptable weld diameter and the expulsion limit meet the requirements set for spot welds. If the weld time is decreased, the current should be increased to obtain an acceptable weld nugget diameter; conversely when the weld time increases, the weld current applied should decrease, as shown in Fig. 2.6 b.

Den Uijl *et al.* [22] reported that pores within a weld are not necessarily detrimental for the mechanical performance of the welds. If the joint fails outside the weld zone, then the pores do not contribute to the weld failure.

2.3 Microstructures of AHSS Resistance Spot Welds

A typical cross section of a resistance spot weld in an AHSS is shown in Fig. 2.7. These steels are in general produced via a specific thermal mechanical cycle. The thermal-mechanical cycle during resistance spot welding destroys the carefully designed multi-phase microstructures of AHSSs, mentioned in section 2.1. The resulting weld microstructure is both chemically and mechanically heterogeneous [24]. The microstructure of the welded region consists of a Fusion Zone (FZ) ($T > T_{Liquidus}$), a
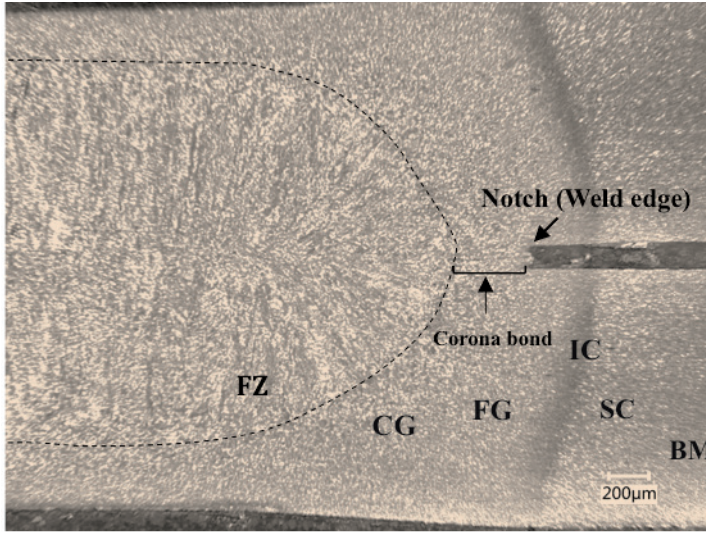
Fig. 2.7 Cross section of a resistance spot weld.
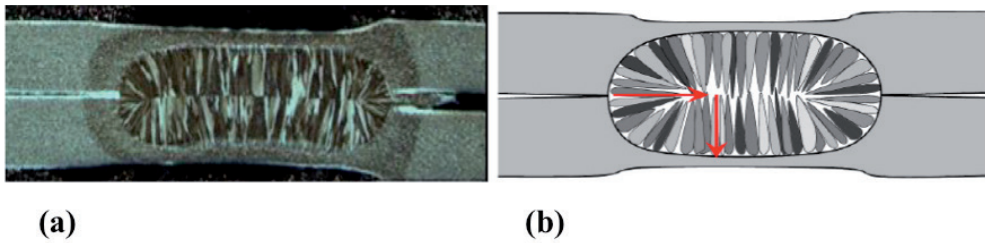
Fig. 2.8 (a) An example of typical solidification grain orientation in a resistance spot weld and (b) a schematic representation of the solidification structure direction, which is dictated by the maximumm temperature gradient [28].

Coarse-Grained Heat Affected Zone (CGHAZ) ($A_{C3} < T < T_{Liquidus}$), a Fine-Grained HAZ (FGHAZ) ($T > A_{C3}$), an Inter-Critical HAZ ($A_{C1} < T < A_{C3}$), a Sub-Critical HAZ (600 °C $< T < A_{C1}$) and the Base Metal (BM), which is not affected during the welding process. In the HAZ, the temperature will not reach the liquidus, but grain growth, grain refinement and phase transformations affect the microstructure [25, 26].

As shown in Fig. 2.7, due to the interface between the two welded parts, there is a notch (natural crack) at the weld edge. Some welds also show a diffusion-bonded zone, known as the corona bond. In this area, the material is joined under the influence of high temperature and pressure, without melting and it is a part of the HAZ. The corona bond can be opened at relatively low loads, after which it acts as a pre-crack during mechanical testing [27]. The microstructure in front of this natural crack is of significant importance in determining the mechanical performance of spot welds.

During cooling of the fusion zone, a typical epitaxial solidification of dendrites with directional growth towards the centreline (direction of highest cooling rate) is observed. Fig. 2.8 shows this directional solidification structure in a resistance spot weld [28]. The presence of a relatively high percentage of alloying elements in combination with the high cooling rates of the welding process leads to the formation of a martensitic microstructure.

Alloying elements like silicon, manganese and phosphorous tend to segregate to the grain boundaries during solidification [29, 30]. Furthermore, the formation of non-metallic and complex inclusions is reported in the fusion zone of welded AHSSs [24, 31-32]. Apart from the martensite, the segregation of the alloying elements and inclusions are factors that considerably influence the performance of spot welds.

2.4 Residual stresses of the welds

Residual stresses are internal stresses that remain in balance within the material after external forces are removed [33]. During welding, residual stresses are generated within the work piece that influence the mechanical behaviour of the material. The source of the residual stress can be elastic misfits, elastic-plastic misfits, temperature gradients and phase transformations [34].

Residual stresses are classified into three groups, type I, type II and type III [33]. A schematic representation of these types is shown in Fig. 2.9. Type I represents a macro-stress. The macro-stress acts over a long range of least several grains. Type II is a micro-stress, which covers a distance of one grain or even smaller. Type III is the residual stress on an atomic scale. In this work, the focus is on the types I and II [33].

In the literature, data presented on residual stress introduced by resistance spot welding is limited. The residual stresses within the welds can be measured using destructive or non-destructive techniques [35]. Destructive techniques include hole drilling, ring core
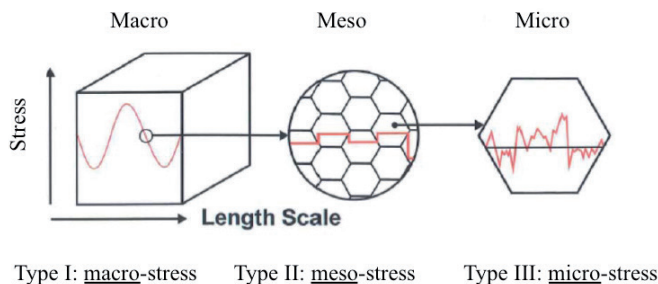
Fig. 2.9 Classification of residual stresses [35].

and deep hole drilling, block removal splitting and layering (BRSL) and slotting and contour mapping. Details about these techniques can be found elsewhere [35].

Non-destructive techniques include laboratory X-ray diffraction, synchrotron X-ray diffraction, neutron diffraction, ultrasonic wave velocity and magneto-acoustic emission [35]. In this work, *ex-situ* synchrotron X-ray diffraction was used to measure the residual stresses of the welds. Synchrotron X-rays have a higher energy and will penetrate deeper compared with Laboratory X-rays. In this technique, the distances between the crystallographic planes of the material are measured. The elastic deformations are measured and residual strain and stresses can be calculated. Details of the measurements and the data analysis are provided in chapter 3.

2.5 Mechanical Properties of Spot Welds

The mechanical properties of resistance spot welds are in general evaluated via Tension Shear Strength (TSS), Cross Tension Strength (CTS), Coach Peel (CP) and chisel tests. Fig. 2.10 shows a schematic of the sample and stress state for these loading conditions. These tests apply shear loading, normal tensile loading and bending tensile loading, respectively. Chisel tests are intended to reveal weld nugget size [36].

During mechanical testing, load-displacement diagrams can be obtained. Fig. 2.11 presents a typical TSS, CTS curve of a spot weld. During loading, the load and displacement increases and when a crack initiates and propagates, the load level decreases. Peak load (P_{max}), displacement at the peak load (L_{max}) and failure energy (W_{max}) can be extracted from these curves (Eq. 2.2) [36]. It should be mentioned that there is a direct relationship between the weld nugget size and P_{max} and L_{max}. A larger weld nugget shows improved mechanical performance such as a larger load bearing capacity and an increased displacement.

$$W = \int P.dL. \qquad\qquad\qquad \text{(Eq. 2.2)}$$

A qualitative measure of mechanical properties of a resistance spot weld can be obtained by investigating its failure mode. Fig. 2.12 shows schematic fracture surfaces of spot welds for different failure modes during mechanical testing. Modes of failure in resistance spot welds are classified as follows [36]:

1. Interfacial Failure (IF): In this failure mode, the crack originating from the notch propagates through the fusion zone and the mechanical properties are poor.
2. Partial Interfacial mode (PIF): Fracture starts in the fusion zone and the crack path is then deflected and propagates in the thickness direction of the sheet.
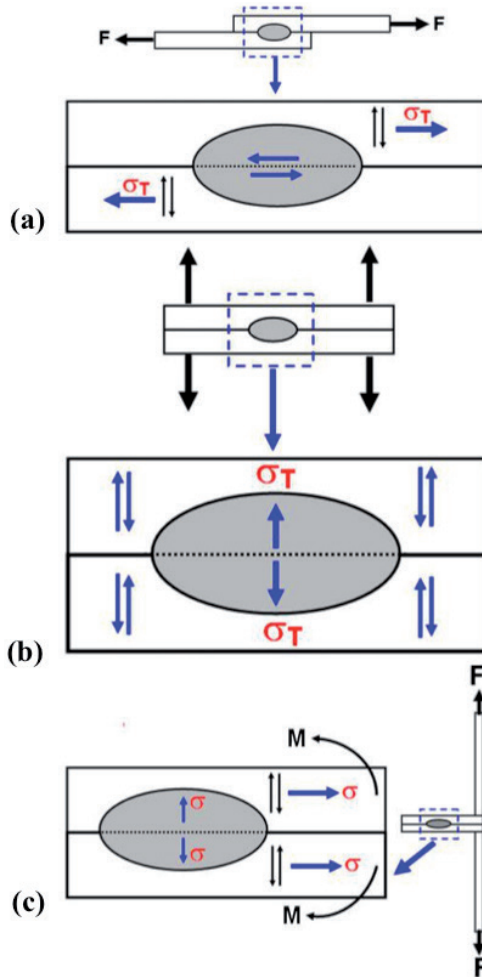
Fig. 2.10 Schematic cross-sectioned view of the loading conditions (a) TSS, (b) CTS, (c) CP tests (σT represents tensile stress) [36].

3. Partial Thickness-Partial Plug mode (PT-PP): A slant crack propagates into the fusion zone. In the final stage of the failure, the remaining sheet metal will fail.
4. Plug Failure (PF): Plug failure occurs when the weld nugget detaches from one of the sheets. In this case, depending on the loading condition and geometrical and metallurgical features of the weld, fracture may start from the base metal, HAZ or fusion line. The PF mode presents appropriate mechanical properties of a spot weld. It should be mentioned that plug failure is the most favorable failure mode that relates to high plastic deformation as well as high energy absorption of the weld [36].
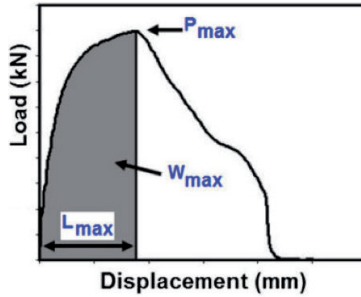
Fig. 2.11 Typical load-displacement diagram of a TSS or CTS test [36].
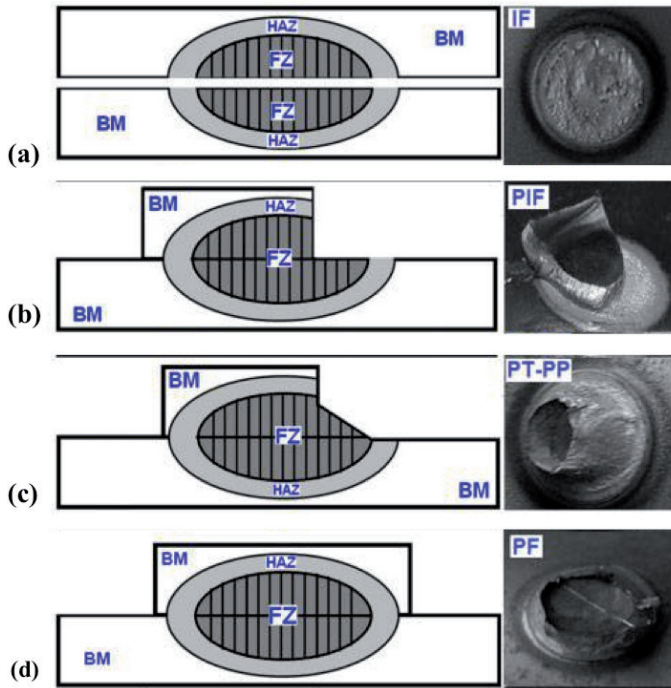
Fig. 2.12 Schematic picture of (a) interfacial failure (IF), (b) partial interfacial failure (PIF), (c) partial thickness-partial plug (PT-PP) failure and (d) plug failure (PF) modes [36].

Generally in RSW, there is a critical weld nugget size where the failure changes from interfacial to plug failure mode. However, in the newest generation of AHSSs, even the largest weld nugget sizes (before splashing occurs) have the tendency to show failure modes other than the desirable full plug failure when subjected to cross tension strength (CTS) testing [36, 37].

Mechanical properties of resistance spot welded AHSSs have been extensively investigated [38-45]. A plot of measured tension shear (TSS) and cross tension (CTS) strengths as a function of base material strength and a schematic representation of
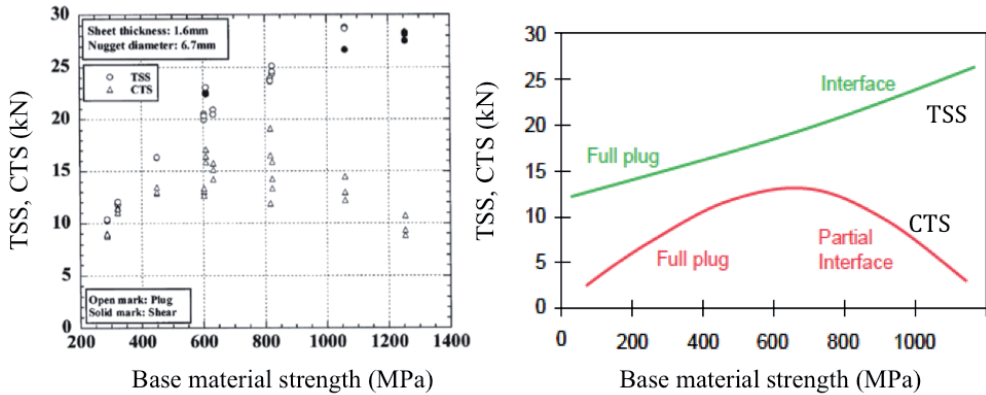
Fig. 2.13 (a) measured and (b) schematic representation of TSS (green-coloured) and CTS (red-coloured) versus base material strength [18].

the same plot are shown in Fig. 2.13 [18]. For base materials with a tensile strengths higher than 800 MPa, the CTS strength decreases, whereas for a TSS loading condition, strength continues to increase. Tumuluru [46] also reported this effect and attributed it to the relatively high alloying element content in AHSSs and high cooling rates that results in a fully martensitic microstructure of the weld nugget. The brittle martensitic microstructure of the weld leads to a brittle fracture during CTS testing [47-50].

The main issue affecting RSW of AHSSs/UHSSs is the poor mechanical performance of the welds, including the unfavorable failure modes and low mechanical strength and ductility of the welds. This needs to be solved to obtain acceptable resistance spot weldability in these materials.

2.6 Post pulsing of resistance spot welds

One of the efficient means of modifying the microstructure and thus the mechanical performance of resistance spot welds is re-heating of the weld by application of a second current pulse, known as post pulsing [50-58]. In the literature, various welding schemes are mentioned to improve the mechanical properties of the spot welds.

Hernandez *et al.* [53] have studied the effect of a second pulse current during resistance spot-welding of TRIP steels with respect to the microstructure and its relation to the mechanical properties of the material. Three different post pulse schemes were applied during RSW of TRIP700 steel with a sheet thickness of 1 mm as shown in Fig. 2.14. The calculated thermal histories of the weld nugget show that the post pulse of 5 kA leads to heating below the A_{C1} temperature; thereby annealing the martensitic weld nugget. A post pulse of 7 kA results in full re-austenisation of the weld nugget and due to the high cooling rate, a martensitic microstructure after welding. The 9 kA post pulse leads
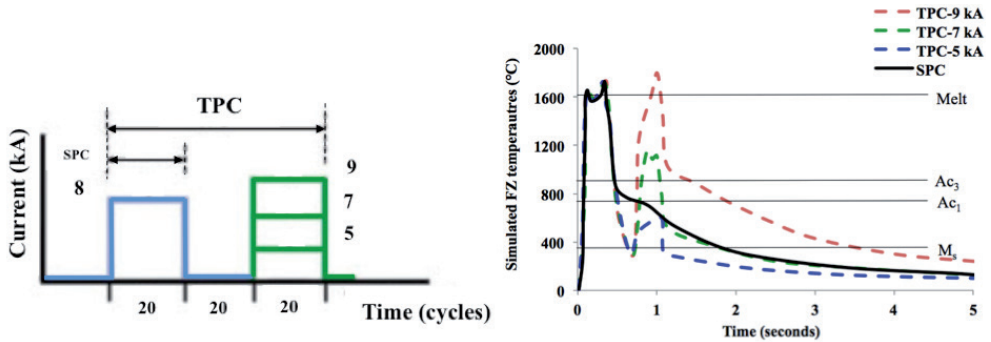
Fig. 2.14 (a) Schematic representation of the welding schedule applied to TRIP700 steel (each cycle is 16.67 ms) and (b) the calculated thermal histories in the weld nugget. SPC refers to single pulse current and TPC refers to two pulse current [53].

to re-melting of the entire primary weld nugget. According to hardness measurements and TSS tests, the optimum performance for the condition studied, in terms of failure mode and strength levels was obtained for the weld with a post pulse of 7 kA. This improvement was attributed to the grain orientation improvement at the weld edge [53].

Based on this experimental observation, it appears that post pulsing can be an appropriate solution for modifying the microstructures of resistance spot welded AHSSs. Post pulsing can improve the microstructure at the weld edge. It should be mentioned that post pulsing extends the weld cycle and therefore the welding time, which could be a drawback for this solution for industrial application.

Another approach to consider is to temper the martensitic microstructure of the weld by post weld heat treatment to increase the ductility [59, 60]. This will be explained in the next section.

2.7 Paint bake cycle effect on resistance spot welds

In automotive manufacturing, after assembly, the welded car bodies (body-in-white) are subjected to a paint bake cycle. The typical paint bake cycle heats the material to approximately 453 K (180 °C) for 20 min in order to bake the paint layers on the structure as well as hardening and curing the coatings and adhesives. It is known that a typical paint bake cycle increases the yield strength of steel similar to the yield strength increment in bake hardenable steel grades [61, 62]. The thermal cycle may also temper the martensite [60]. Depending on the alloying content of the base material, the paint bake cycle could lead to different stages of martensite tempering [63]. Tumuluru [64] has reported the effect of a baking cycle on the structure and properties of resistance

spot welds in 780 MPa dual phase and TRIP steels. It is reported that post weld baking increased the load bearing ability of the weld in shear tension by about 6% compared with the as welded condition. This increase was attributed to the strain aging of ferrite and tempering of martensite after baking in DP and TRIP steels, respectively.

The typical paint bake cycle is a low-temperature post-weld heat treatment that can affect the microstructure and mechanical performance of spot welds. The metallurgical changes due to this thermal cycle can help to improve the mechanical properties of the welds. Although it is known that the baking cycle improves the mechanical properties of the base material such as yield strength, the effect of baking cycle on the resistance spot welds of AHSSs is not yet studied in detail.

Concluding remarks

Resistance spot welding is a complex process, where high currents are passed through the workpiece and melting occurs at the faying interface of the sheets to be welded. The process does not allow direct observation of the formation of the weld nugget.

The mechanical performance of resistance spot welded AHSSs is a crucial issue in the automotive industry. The relatively high alloying element content of AHSSs and ultra fast cooling rates during the resistance spot welding result in a fully martensitic weld nugget microstructure. During mechanical testing of these welds, cracks easily propagate within the brittle weld metal and result in weld metal failure (interfacial failure), which is not a favourable failure mode. Improving the microstructure of the weld nugget and HAZ can help to improve the mechanical performance of these welds. Strategies such as double pulse welding and application of a paint bake cycle have been studied and results indicate that the mechanical behaviour can be improved by such technique. However, detailed information on how to obtain optimal welding condition is still lacking. Such strategies will be discussed in this thesis to improve the mechanical response of the resistance spot welded AHSSs. The results contribute to a better understanding of the mechanical response of the spot welds.

References

[1]   E. Billur, J. Dykeman, T. Altan. *Three generations of advanced high-strength steels for automotive applications*, Part I, II and III, Stamping Journal, www.stampingjournal.com, 2013-2014.

[2]   S. Keeler, *Advanced high strength steels (AHSS) guidelines.* Technical Report Version 4.1, World auto steel, World steel association (2015).

[3]   N. Baluch, Z.M. Udin, C.S. Abdullah, *Advanced high strength steel in auto industry: An overview*, Eng. Tech. Appl. Sci. Res. 4 (2014) 686–689.

[4]   G. Thomson, *Method of electric welding*, United States patent 451345, patented on 28th April 1890.

[5]   S.K. Khanna, X. Long, *Residual stresses in resistance spot welded steel joints.* Sci. Technol. Weld. Join. 13(3) (2008) 278–288.

[6]   S.S. Nayak, Y. Zhou, V.H. Baltazar Hernandez, E. Biro, *Resistance spot welding of dual-phase steels: heat affected zone softening and tensile properties.* Proceedings of the 9th International Conference on Trends in Welding Research, Chicago, Illinois, United States (2012) 641–649.

[7]   M. Janota, H. Neumann, *Share of spot welding and other joining methods in automotive production*, IIW Annual Assembly, Dubrovnik, Croatia, 2007, document number: III- 1423-07.

[8]   W.H. Kearns, *Resistance and solid state welding and other joining processes,* Welding Handbook, Seventh edition, volume 3, American Welding Society, ISBN 0-87171-188-5, (1980).

[9]   H. Zhang, J. Senakara, *Resistance welding: fundamentals and applications*, CRC Press, ISBN 0-8493-2346-0 (2006).

[10] N. T. Williams, J. D. Parker, *Review of resistance spot welding of steel sheets: Part 1 – Modelling and control of weld nugget formation*, Int. Mater. Rev. 49 (2004) 45–75.

[11] A.C. Davies, *The science and practice of welding, volume 2, The practice of welding*, Cambridge University Press, ISBN 0 521 27840 6 (1986).

[12] WeldCor, WeldCor Supplies Inc., 2013. Available: https://www.weldcor.ca/index. php/encyclopedia.html?alpha=R&per_page=3.

[13] M. Enami, M. Farahani, M. Sohrabian, *Evaluation of mechanical properties of resistance spot welding and friction stir spot welding on aluminum alloys*, International conference on researches in science and engineering, Istanbul university, Turkey, 28th July 2016.

[14] SEP 1220-2: *Testing and documentation guideline for the joinability of thin sheet of steel-part 2: resistance spot welding*. VDEh Standard; (2007) (Technical Report 08).

[15] P.T. Houldcroft, *Welding Process Technology*, Cambridge University Press, ISBN 0-521-21530-7 (1977).

[16] B. Xing, Y. Xiao, Q.H. Qin, *Characteristics of shunting effect in resistance spot welding in mild steel based on electrode displacement*, Measurement 115 (2018) 233-242.

[17] N.J. Den Uijl, *Resistance spot welding of a complicated joint in new advanced high strength steel*, Proceedings of the 6th International Seminar on Advances in Resistance Welding, Hamburg, Germany, Sep. 2010.

[18] S. Furusako, G. Murayama, H. Oikawa, T. Nose, F. Watanabe, H. Hamatani, Y. Takahashi, *Current Problems and the Answer Techniques in Welding Technique of Auto Bodies (First Part)* - Nippon Steel Technical Report 103 (2013) 69-75.

[19] A. Madsen, K.R. Pedersen, K.S Friis, N. Bay, *Analysis and modelling electrode wear in resistance spot welding*, Proceedings of the 6th International Seminar on Advances in Resistance Welding, Hamburg, Germany, Sep. 2010.

[20] K. Chan, N. Scotchmer, J.C. Bohr, IA. Khan, M. Kuntz, N. Zhou, *Effect of Electrode Geometry on Resistance Spot Welding of AHSS*, 4th International Seminar on Advances in Resistances in Resistance Welding, Wels, Austria; Nov. 2006.

[21] O. Anderson, *Process planning of resistance spot welding*, Master Thesis, Department of production engineering, Royal Institute of Technology, Stockholm, Sweden (2013).

[22] N.J. Den Uijl and S. Smith, *Resistance Spot Welding of Advanced High Strength Steels for the Automotive Industry*, Proceedings of the 4th International Seminar on Advances in Resistance Welding, Wels, Austria, Nov. 2006.

[23] P.K. Mallick, Material, *Design and Manufacturing for Lightweight Vehicles*, Woodhead Publishing, ISBN 978-1-84569-463-0 (2010).

[24] M. Amirthalingam, *Microstructural Development during welding of TRIP steels*, Ph.D. thesis, Delft University of Technology, ISBN 978-9-77172-99-5 (2010).

[25] K. Easterling, *Introduction to the Physical Metallurgy of Welding 2nd edition*, Butterworth Heinemann, ISBN 0-7506-0394-1 (1992).

[26] D. Radaj, *Heat Effects of Welding, Temperature Field, Residual Stress, Distortion*, Springer Verlag, ISBN 3-540-54820-3 (1992).

[27] K. Sonoya, K. Fukui, M. Suzuki, *Effect of welding conditions of spot welded zone on the tensile strength about aluminum alloy (A6061)*, Universal Journal of Mechanical Engineering 4(1) (2016) 8-18.

[28] E.M. van der Aa, *Failure of advanced high strength automotive steel resistance spot welds subjected to mechanical loading, a literature review*, Internal report Tata Steel (2015).

[29] M. Amirthalingam, E.M. van der Aa, N.J. den Uijl, M.J.M. Hermans, I.M. Richardson, *Phosphorous and boron segregation during resistance spot welding of advanced high strength steels.* Proceedings of the 9th International Conference on Trends in Welding Research, Chicago, Illinois, United States (2012) 217–226.

[30] M. Amirthalingam, E.M. van der Aa, C. Kwakernaak, M.J.M. Hermans, I.M. Richardson, *Elemental segregation during resistance spot welding of boron containing advanced high strength steels*, Weld. World 59 (2015) 743–755.

[31] A. Grajcar, M. Rozanski, M. Kaminska, B. Grzegorczyk, *Study on non-metallic inclusions in laser-welded TRIP-aided Nb microalloyed steel*, Arch. Metall. Mater. 59 (2014) 1163–1169.

[32] J.E. Ramirez, *Characterization of high-strength steel weld metals: chemical composition, microstructure, and non-metallic inclusions.* Weld. J. 87 (2008) 65s–75s.

[33] P.J. Withers, H.K.D.H. Bhadeshia, *Overview-Residual stress part 2-Nature and origins.* Mater. Sci. Technol. 17(4) (2001) 366-375.

[34] C. Ohms, *Residual stresses in thick bi-metallic fusion welds*. PhD thesis, Delft University of Technology (2013).

[35] H. Gao, *Residual Stress Development due to High-Frequency Post Weld Impact Treatments for High-Strength Steels*. PhD thesis, Delft University of Technology (2014).

[36] M. Pouranvari, S.P.H. Marashi, *Critical review of automotive steels spot welding: process, structure and properties*, Sci. Technol. Weld. Join. 18(5) (2013) 361-403.

[37] M. Pouranvari, H.R. Asgari, S.M. Mosavizadch, P.H. Marashi, M. Goodarzi, *Effect of weld nugget size on overload failure mode of resistance spot welds*, Sci. Technol. Weld. Join. 12(3) (2007) 217–225.

[38] Y.J. Chao, *Failure mode of spot welds: interfacial versus pull out*, Sci. Technol.Weld. Join. 8(2) (2003) 133–137.

[39] F. Nikoosohbat, S. Kheirandish, M. Goodarzi, M. Pouranvari, S.P.H. Marashi, *Microstructure and failure behaviour of resistance spot welded DP980 dual phase steel*, Mater. Sci. Technol. 26 (2010) 738–744.

[40] S. Dancette, V. Massardier-Jourdan, D.F.J. Merlin, T. Dupuy, M. Bouzekri, *HAZ microstructures and local mechanical properties of high strength steels resistance spot welds*, ISIJ Int. 51 (2011) 99–107.

[41] S. Sam, M. Shome, *Static and fatigue performance of weld bonded dual phase steel sheets*, Sci. Technol. Weld. Join. 15 (2010) 242–247.

[42] M. Pouranvari, S.P.H. Marashi, *Key factors influencing mechanical performance of dual phase steel resistance spot welds*, Sci. Technol. Weld. Join. 15 (2010) 149–155.

[43] M. Pouranvari, S.P.H. Marashi, S.M. Mousavizadeh, *Failure mode transition and mechanical properties of similar and dissimilar resistance spot welds of DP600 and low carbon steels*, Sci. Technol. Weld. Join. 15 (2010) 625–631.

[44] V.H. Baltazar Hernandez, S.K. Panda, Y. Okita, N.Y. Zhou, *A study on heat affected zone softening in resistance spot welded dual phase steel by nanoindentation*, J. Mater. Sci. 45 (2010) 1638–1647.

[45] W. Tong, H. Tao, N. Zhang, X. Jiang, M.P. Marya, L.G. Hector Jr., X.Q. Gayden, *Deformation and fracture of miniature tensile bars with resistance-spot-weld microstructures*, Metall. Mater. Trans. A 36 (2005) 2651–2669.

[46] M.D. Tumuluru, *Resistance spot welding of coated high-strength dual-phase steels*, Weld. J. 85 (2006) 31–37.

[47] M. Pouranvari, S.P.H. Marashi, S.M. Mousavizadeh, *Dissimilar resistance spot welding of DP600 dual phase and AISI 1008 low carbon steels: correlation between weld microstructure and mechanical properties*, Ironmak. Steelmak. 38 (2011) 471–480.

[48] S. Dancette, D. Fabrègue, V. Massardier, J. Merlin, T. Dupuy, M. Bouzekri, *Experimental and modeling investigation of the failure resistance of advanced high strength steels spot welds*, Eng. Fract. Mech. 78 (2011) 2259–2272.

[49] C. Sawanishi, T. Ogura, K. Taniguchi, R. Ikeda, K. Oi, K. Yasuda, A. Hirose, *Mechanical properties and microstructures of resistance spot welded DP980 steel joints using pulsed current pattern*, Sci. Technol. Weld. Join. 19(1) (2014) 52–59.

[50] N.J. Den Uijl, S. Smith, T. Moolevliet, C. Goos, E.M. van der Aa, T. van der Veldt, *Failure modes of resistance spot welded advanced high strength steels*, 5th International Seminar on Advances in Resistance Welding, Toronto, Canada, (2008).

[51] N.J. Den Uijl, H. Nishibata, S. Smith, T. Okada, M. Uchihara, F. Fukui, *Prediction of post weld hardness of advanced high strength steels for automotive application using a dedicated carbon equivalent number*, IIW Annual Assembly, Dubrovnik, Croatia, document number: III- 1444-07 (2007).

[52] E.M. Van der Aa, M. Amirthalingam, J. Winter, D.N. Hanlon, M.J.M. Hermans, M. Rijnders, I.M. Richardson, *Improved resistance spot weldability of 3rd generation AHSS for automotive applications*, 11th International Seminar on Numerical Analysis of Weldability, Graz, Austria (2015).

[53] V.H. Baltazar Hernandez, Y. Okita, Y. Zhou, *Second pulse current in resistance spot welded TRIP steel—effects on the microstructure and mechanical behavior*, Weld. J. 91 (2012) 278–285.

[54] M. Matsushita, K. Taniguchi, K. Oi, *Development of next generation resistance spot welding technologies.* JFE Technical Report. 18 (2013) 111-117.

[55] N.J. Den Uijl, *Resistance spot welding of advanced high strength steels*, Dissertation, Delft University of Technology (2015).

[56] A. Peer, Y. Lu, T. Abke, M. Kimchi, W. Zhang, *Deformation behaviors of subcritical heat-affected zone of ultra-high strength steel resistance spot welds*, 9th International Seminar and Conference on Advances in Resistance Welding. Miami, USA (2016).

[57] Y. Lu, A. Peer, T. Abke, M. Kimchi, W. Zhang, *Heat-affected zone microstructure and local constitutive behaviors of resistance spot welded hot-stamped steel*, Sheet Metal Welding Conference XVII. Livonia, MI (2016).

[58] C. Wakabayashi, S. Furusako, Y. Miyazaki, *Strengthening spot weld joint by autotempering acceleration at heat affected zone*, Sci. Technol. Weld. Join. 20 (6) (2015) 468–472.

[59] M. Mimer, L.E. Svensson, R. Johansson, *Process adjustments to improve fracture behavior in resistance spot welds of EHSS and UHSS*, Weld. World. 48 (2004) 14–18.

[60] X. Liao, X. Wang, Z. Guo, M. Wang, Y. Wu, Y. Rong, *Microstructures in a resistance spot welded high strength dual phase steel*, Mater. Charact. 61 (2010) 341–346.

[61] *ASM handbook. Heat Treating.* Volume 4. ASM International ISBN-13: 978-0-87170-379-8.

[62] I.B. Timoknina, P.D. Hodgson, S.P. Ringer, R.K. Zheng, E.V. Pereloma, *Understanding Bake-Hardening in Modern High Strength Steels for the Automotive Industry Using Advanced Analytical Techniques*, New Developments on Metallurgy and Applications of High Strength Steels Conference, Buenos Aires, Argentina, 26-28, May 2008.

[63] G.R. Speich, W.C. Leslie, *Tempering of steel*, Metal. Trans. 3(5) (1972) 1043-1054.

[64] M. Tumuluru, *Effects of Baking on the Structure and Properties of Resistance Spot Welds in 780 MPa Dual-Phase and TRIP Steels*, Weld. J. 89 (2010) 91s-100s.

CHAPTER 3

Experimental and modelling methods and procedures

This chapter provides an overview of all analysis techniques applied to characterise the base metal, heat affected zone and weld metal of resistance spot welds. In the first part (section 3.1), the general experimental methods employed to study the microstructure, mechanical behaviour and residual stresses are described. In the next part (section 3.2), the characterisation of the base material is discussed. The base materials studied are a 3rd generation 1 GPa AHSS CR700Y980T-DH-GI and a hot stamping boron steel, 22MnB5 steel. In section 3.3, details of various welding sequences are provided. All the experimental procedures to study the welds are described in section 3.4. In order to predict the residual stresses of resistance spot welds, models are constructed. The modelling approach to obtain the temperature distribution and residual stresses is presented in section 3.5.

3.1 General characterisation techniques

3.1.1 Optical microscopy and scanning electron microscopy

For optical microscopy analysis, the sheets were cross-sectioned, polished and etched with 4% Nital solution for 5 s. To reveal dendrites and prior austenite grain boundaries in the weld nugget and HAZ of the welds, an etchant consisting of 1% aqueous solution of sodium dodecylbenzenesulfonate and 4% picric acid in ethanol (Béchet-Beaujard reagent) was used. Microstructural analyses were carried out using a Keyence VHX Multi Scan Digital microscope.

For scanning electron microscopy (SEM), the samples were polished and etched with 4% Nital for 5 s. Microscopy was performed using a JEOL JSM-6500F field emission gun (FEG) scanning electron microscope operating at 15 kV.

3.1.2 Elemental analysis

Quantitative elemental distributions at the weld edges of resistance spot welds were determined by electron probe microanalysis (EPMA at Tata steel). The measurements were performed with a Cameca SX100 microprobe, using an electron beam with an energy of 15 keV and a beam current of 100 nA, employing wavelength dispersive spectroscopy (WDS). The composition at each analysis location was determined using the X-ray intensities of the constituent elements after background correction relative to the corresponding intensities of reference materials. The intensities were processed with a phi-rho-z matrix correction program from Cameca. Analyses were made on 200×200 μm^2 areas near the weld edges with a spot size of 1 μm, a step size of 1 μm and a counting time of 1 second per point.

3.1.3 Orientation contrast microscopy

Electron backscatter diffraction (EBSD) data were acquired using a FEI-Quanta 450 scanning electron microscope equipped with a field emission gun (FEG). The microscope settings were as follows: an accelerating voltage of 20 kV, a beam current of ~2.4 nA, corresponding to a spot size of 5 μm at a 40 μm aperture. The EBSD scans were acquired over areas of 200×200 μm^2 in square scan grid mode with a step size of 0.15 μm at a working distance of 16 mm and a 70° sample tilt to the horizontal axis. The EBSD data was post processed by means of TSL®- orientation image microscopy (OIM™) data analysis software. Post processing omitted the points with confidence index (CI) lower than 0.1 from the EBSD maps. To reconstruct the prior austenite grain boundaries, APRGE™ software was used [1]. The block width was estimated by drawing misorientation profile lines along various parallel block batches. Measurements were made along a line perpendicular to the long axis of the blocks and more than 500 blocks were considered to obtain an average block width.

3.1.4 Transmission electron microscopy

For transmission electron microscopy (TEM) samples, conventional thin foils were extracted from the weld nugget and HAZ of the samples. The welds were cut to 0.2 mm thick sheets using a low-speed diamond-cutting wheel. The thickness of each sample was reduced mechanically to 0.1 mm. Disks with a diameter of 3 mm were punched from these foils. To reduce thickness further, the disks were electro-polished using an electrolyte of 15% hydrochloric acid, 82% ethanol and 3% glycerol and with a voltage of 11 V and a current of 60 mA at room temperature. Once the optical sensor in the polisher detected a hole in the centre of the sample, the polishing was stopped. Subsequently, the sample was immersed in ethanol. The TEM analysis was carried out using a JEOL JEM-2200FS transmission electron microscope with a field emission gun. The indexation of the TEM diffraction patterns was performed with CrysTbox™ software [2].

3.1.5 Laboratory X-ray diffraction (XRD) analysis

Laboratory X-ray diffraction (XRD) analysis was performed using a Bruker D8-Advance diffractometer in Bragg-Brentano geometry with a graphite monochromator equipped with a Vantec position sensitive detector using Co-Kα radiation. Measurements were performed in the 2θ range of 40° to 130° with a step size of 0.035° (2θ) and an acquisition time of 4 s per step.

3.1.6 Phase fraction determination with synchrotron X-ray diffraction

In order to study the effect of mechanical loading on the solid-state phase transformations of the AHSS, *in-situ* synchrotron X-ray diffraction experiments were conducted at the ID11 beamline of the European Synchrotron Radiation Facility (ESRF) in Grenoble,

France. A beam energy of about 80 keV (λ= 0.15582 Å) and a beam size of 300×300 μm² were used. To obtain diffraction data, a 2D CCD detector (FReLoN-fast readout low noise) camera system [3] was employed. CeO_2 calibrant was used on each sample to determine sample–detector distance, tilt of the detector, and the beam centre. Corrections were applied to omit dark field, flat field, and detector distortion during data analysis [4]. An Instron/ NPL electro-thermal mechanical testing (ETMT) machine was used.

3.1.7 Residual stress measurements with synchrotron X-ray diffraction

Stress measurements were carried out on the high-resolution powder diffraction beamline ID22 at the European Synchrotron Research Facility (ESRF) in Grenoble, France. A monochromatic 70 keV X-ray, providing a wavelength of 0.17709589 Å with a focal spot size of 150×50 μm² at the sample position was used to record the diffraction patterns of ferrite (200) planes in transmission mode. An analyser crystal was placed between the sample and the detector. A point detector placed behind the sample scanned the 2θ diffraction angle.

3.1.8 Characterisation of mechanical properties

The weld nugget size analysis was carried out for the spot welds using chisel test specimens. In chisel testing, samples as indicated in Fig. 3.1 a are broken (a kind of peel test). The weld nugget size and plug diameter were measured to obtain the weld growth curves and plug ratios, respectively. The plug ratio (ratio of plug diameter to weld nugget diameter) was calculated to analyse the partial plug failures.

Vickers microhardness measurements were conducted at 200 g load for 15 s loading time in a Buehler® micro-hardness testing machine. A schematic representation of the hardness measurement locations is shown in Fig 3.1 d.

Mechanical properties of the welds were evaluated by standard tensile shear strength (TSS) and cross tension strength (CTS) tests as described in chapter 2.4. The specimen dimensions of these tests are shown in (Fig. 3.1). The experimental set-up for TSS and CTS tests at Tata Steel Europe are shown in Fig. 3.2. The TSS and CTS tests were repeated twice and three times, respectively, for each welding sequence. The ductility ratio (ratio of the CTS to the TSS) [5] was calculated for each weld. The weld nugget size and plug ratio (ratio of plug size to weld nugget size) were measured for CTS samples with a Vernier calliper with an accuracy of ±0.01 mm.

Finally, the microstructures of the fractured CTS samples were investigated by optical microscopy and SEM to reveal the crack path.
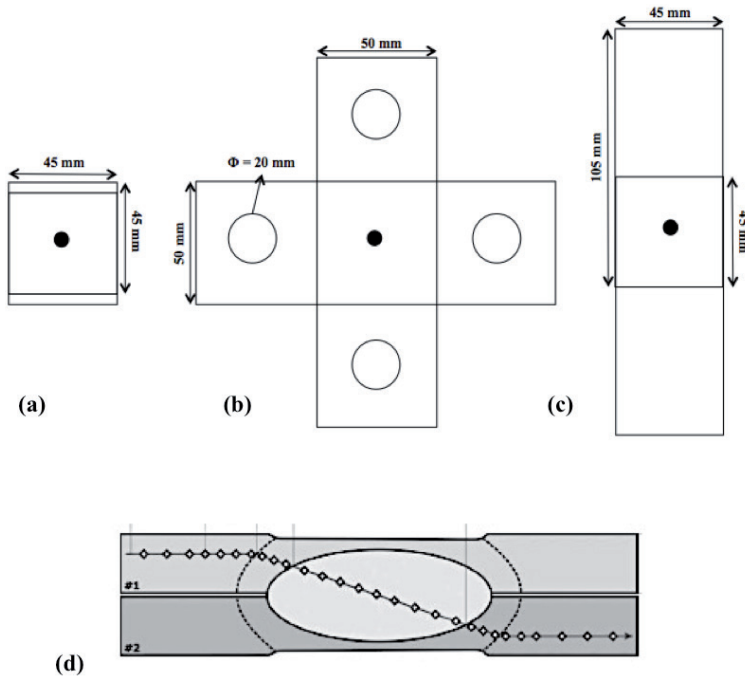
Fig. 3.1 Schematic representation of the samples for (a) chisel test, (b) cross tension strength (CTS) test and (c) tension shear strength (TSS) test and (d) microhardness measurement, the diamonds indicate the locations, where the microhardness was measured, details are mentioned in [6].
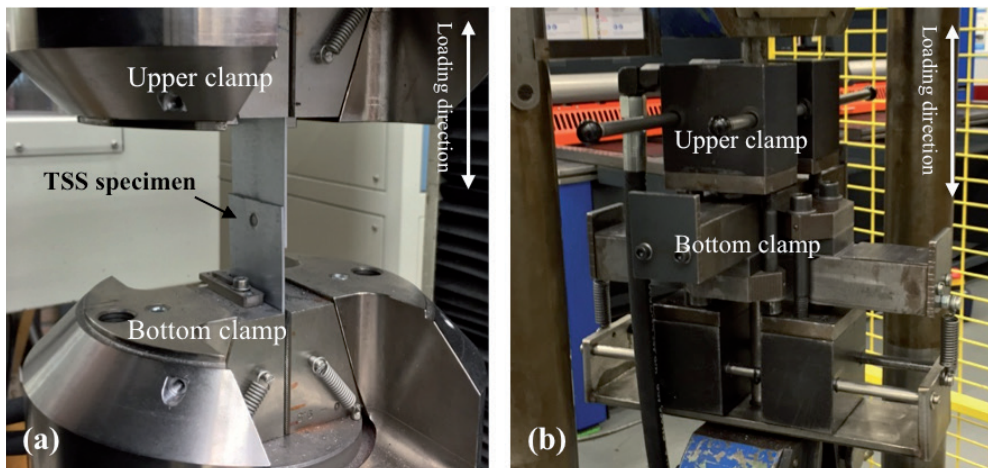
Fig. 3.2 Experimental set-up for (a) TSS and (b) CTS tests at Tata Steel.

3.2 Characterisation of the base material

The current work focuses on a 3rd generation 1 GPa AHSS CR700Y980T-DH-GI with a sheet thickness of 1.3 mm. The steel was received in a cold-rolled and galvanised condition (Zn surface density of 50 gm^{-2}). Material characteristics and chemical composition are according to the VDA (German Association of the Automotive Industry) chemistry for CR700Y980T-DH in the recently drafted VDA specifications [7], as listed in Table 3.1. The initial microstructure of CR700Y980T-DH-GI steel is shown in Fig. 3.3.

The equilibrium phase diagram of the CR700Y980T-DH-GI steel was calculated using a commercial thermodynamic database Thermo-Calc (TCFE7) (Fig. 3.4). The chemical composition of 0.22 wt.% C, 2.11 wt.% Mn, 0.95 wt.% Si, 0.02 wt.% Ni and 0.03 wt.% Al was used as an input for the calculation. The calculated liquidus and solidus temperatures, A_{C1} and A_{C3} are shown in Table 3.2. The martensite start temperature (M_s) in Kelvin was calculated using the equation presented by Andrews (Eq. 3.1) [9].

$$Ms = 539 - 423C - 30.4Mn - 17.7Ni - 12.1Cr - 11.0Si - 7.5Mo \ , \qquad \text{(Eq. 3.1)}$$

where elemental terms signify wt.%.

The measured XRD pattern for the as-received CR700Y980T-DH-GI steel is shown in Fig. 3.5. From the peak intensities of the indicated FCC peaks, the retained austenite content is obtained. The calculated retained austenite (γ) phase fraction obtained from peak intensities is about 4.3±0.2 vol.%.

Elemental maps obtained by Electron Probe Microanalysis (EPMA) of the as-received CR700Y980T-DH-GI steel are shown in Fig. 3.6. The map of Fe (Fig. 3.6 a) shows a banding structure. As can be seen in Fig. 3.6 b and c, Mn and Si are segregated and also appear in the form of banded structures. The elemental maps of P and Al (Fig. 3.6 d and e) show that these elements seem to be present predominantly as inclusions indicated by areas with a high content of these alloying elements.

An ultra high strength hot stamping boron steel, 22MnB5 was also studied. Uncoated 22MnB5, which was heat treated at 925 °C for 6 minutes, and then quenched between two flat sheets (hot pressing simulation). After hot pressing, the sheets were sandblasted to remove excessive oxides, in order to allow RSW. This steel was received as an uncoated sheet with the sheet thickness of 1.5 mm in a hot pressed condition with ultimate tensile strength of 1500 MPa. The chemical composition of this steel is shown in Table 3.3. The initial martensitic microstructure of 22MnB5 steel is shown in Fig. 3.7.

Table 3.1 Material characteristics for CR700Y980T-DH-GI [8].

VDA 239-100 classification	Coating [g/m²]	Yield strength (MPa)	Ultimate tensile strength (MPa)	Elongation at fracture $L_0 = 80$ mm (%)	C (wt.%)	Mn +Cr+ Mo (wt.%)	Si+ Al (wt.%)
CR700Y980T-DH	GI (galvanised) 50	650- 850	980- 1180	13	0.18- 0.22	1.8- 2.3	0.8-1.2

Table 3.2. Calculated transformation temperatures for the steel under investigation based on chemical composition

	Liquidus temperature K	Solidus temperature K	AC1 K	AC3 K	MS K
CR700Y980T-DH-GI	1796 (1523 °C)	1773 (1500 °C)	982 (709 °C)	1072 (799 °C)	618 (345 °C)
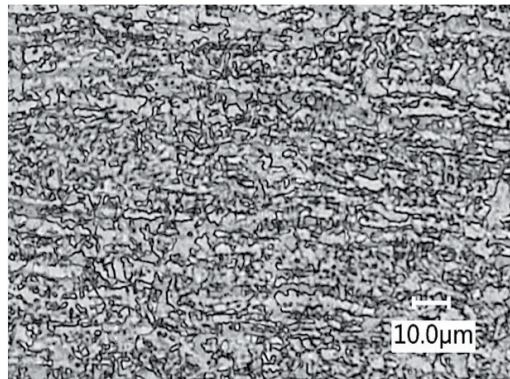
Fig. 3.3 Microstructure of the CR700Y980T-DH-GI steel in as-delivered cold rolled condition.
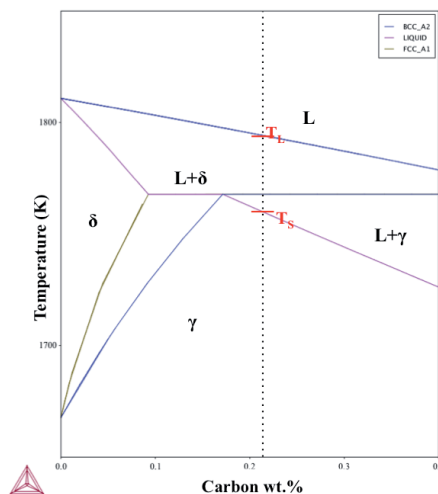
Fig. 3.4 Calculated phase diagrams using Thermo-Calc software for CR700Y980T-DH-GI. The dotted line represents the carbon content of the steel.
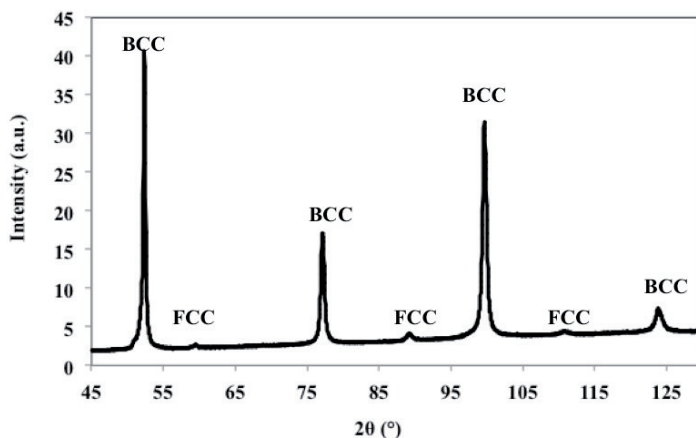
Fig. 3.5 The XRD pattern for the as-received CR700Y980T-DH-GI steel (base material).
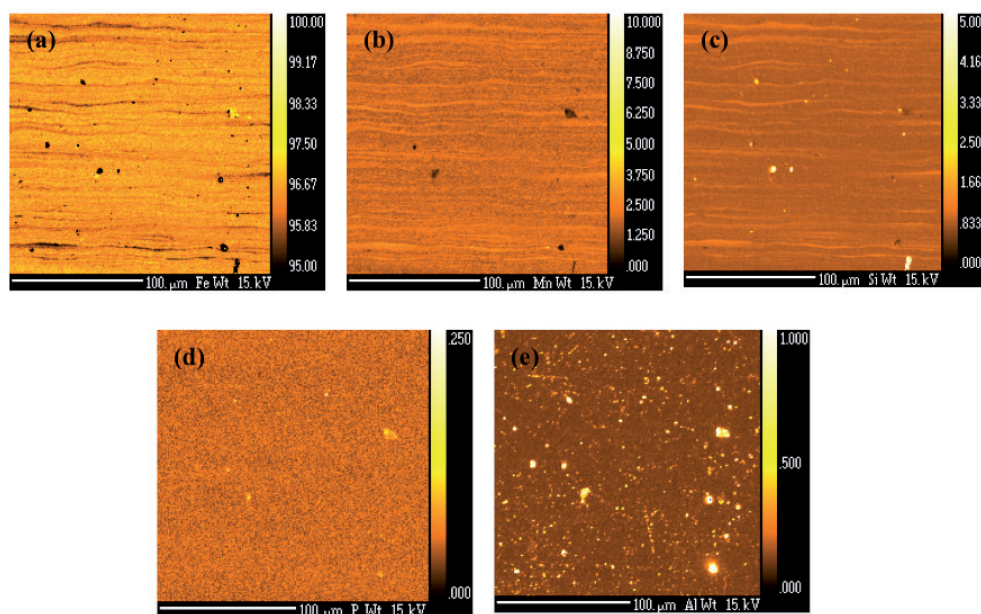
Fig. 3.6 EPMA maps for (a) Fe, (b) Mn, (c) Si, (d) P and (e) Al for the as-received CR700Y980T-DH-GI steel.

Table 3.3 Chemical composition of hot stamping boron steel (22MnB5)

22MnB5	C	Mn	Si	Al	B	P	Cr	Ni	N	Fe
wt.%	0.22	1.187	0.253	0.038	3×10^{-3}	0.007	0.196	0.022	4.9×10^{-3}	Bal.

The measured XRD pattern for the as-received 22MnB5 steel is shown in Fig. 3.8, from which the retained austenite (γ) phase fraction is calculated to be about 1.9±0.2 vol.%.

48
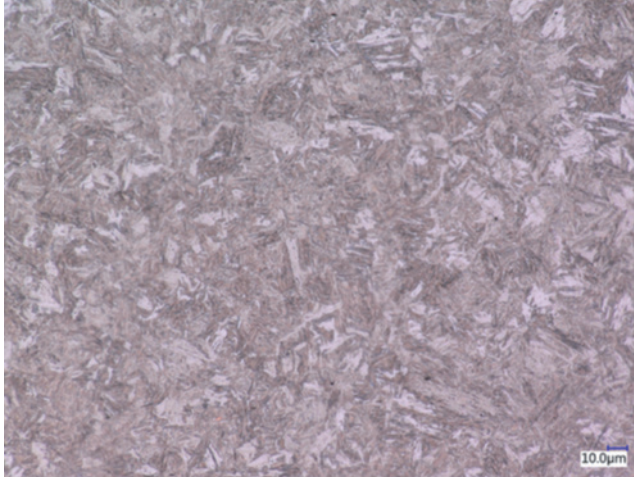
Fig. 3.7 Martensitic microstructure of the hot pressed, un-welded 22MnB5 steel.
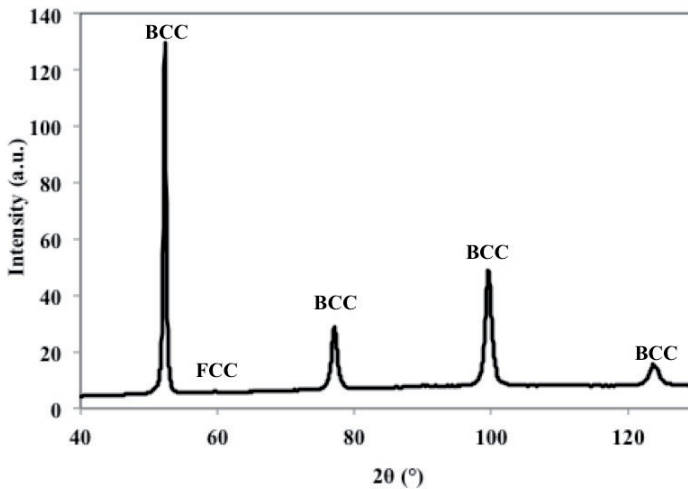
Fig. 3.8 XRD pattern of the as-received 22MnB5 steel.

3.3 Resistance spot welding

Resistance spot welding was carried out on AWL and SchlattesTM pedestal type spot welding machines at Tata Steel. The frequency of 1000 Hz MFDC was used. The AWL welding equipment is shown in Fig. 3.9.

For the welding of CR700Y980T-DH-GI steel, F1 16×5.5 (16 and 5.5 refer to the diameter of the electrode and electrode tip in mm, respectively) electrodes with an electrode force of 4 kN and welding parameters, as described in the VDEh SEP1220-2
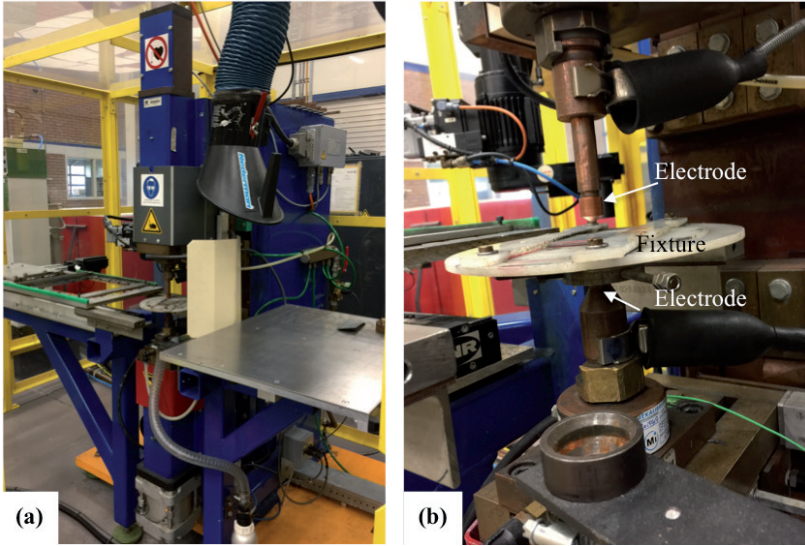
Fig. 3.9 (a) Resistance spot welding equipment at Tata Steel and (b) higher magnification of the welding machine.
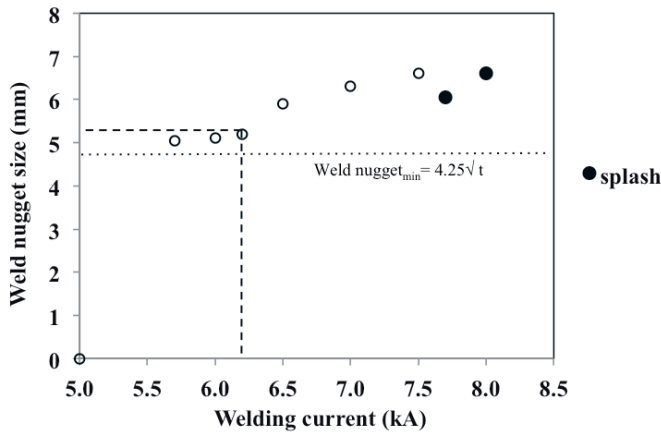
Fig. 3.10 Weld growth curve for the CR700Y980T-DH-GI steel, the solid symbols indicate splashing. The straight dotted line shows the minimum required weld nugget size of the steel studied. The welding current of 6.2 kA that was used as a first pulse current for welding sequences 1-4.

standard (VDEh: German Iron and Steel Institute) were used [8]. Welding parameters employed to construct the weld growth curve are mentioned in Table 3.4. Current was varied between I_{min}, the weld current needed to produce a $4.25\sqrt{t}$ weld nugget diameter, which is the minimum acceptable and I_{max}, the highest current amplitude before splashing occurs.

The weld growth curve for the steel is plotted in Fig. 3.10. The weld nugget sizes range from 5.0 mm to 6.6 mm. Splashing occurs at current levels above 7.5 kA.

Table 3.4 Resistance spot welding parameters for determining the weld growth curve of the 1.3 mm DH1000-GI (weld settings in SEP1220-2 are determined by the material thickness, strength (> 380 MPa) and coating).

	Minimum weld nugget size (4.25 ×√ t) (mm)	Squeeze time (ms)	Weld time (ms)	Hold time (ms)	I range (kA)	I_{min} (kA)	I_{max} (kA)
CR700Y980T-DH-GI	**4.8**	**400**	**320**	**200**	**5.0-8.0**	**5.7**	**7.5**

Table 3.5 Single and double pulse resistance spot welding parameters for CR700Y980T-DH-GI.

Sequence	No. of pulses	Squeeze time (ms)	Weld time 1 (ms)	Current 1 (kA)	Cool time (ms)	Current 2 (kA)	Weld time 2 (ms)	Hold time (ms)
1	**1**	**400**	**320**	**6.2**	**-**	**-**	**-**	**200**
2	**2**	**400**	**320**	**6.2**	**40**	**5.7**	**320**	**200**
3	**2**	**400**	**320**	**6.2**	**40**	**6.2**	**320**	**200**
4	**2**	**400**	**320**	**6.2**	**40**	**6.9**	**320**	**200**

The welding parameters used to produce welds are shown in Table 3.5. Selection of different sets of welding conditions is referred to as a sequence. Sequence 1 is a single pulse resistance spot weld. Apart from the standard single pulse weld scheme, several double pulse weld schemes were applied, with a systematic variation of the second pulse current level. Sequence 2 is a double pulse resistance spot weld with the second pulse current about 8% lower than the first pulse current. In sequence 3, two equal pulse currents in double pulse resistance spot welding were used. Sequence 4 is produced using a second pulse current about 12% higher than the first one. A cooling time of 40 ms was chosen to allow the weld edge to remain austenitic between two pulses. The welding schemes are indicated schematically in Fig. 3.11.

In order to study the effect of a paint bake cycle on CR700Y980T-DH-GI welds, two weld schedules were taken into account: a standard single pulse weld schedule, as well as a double pulse weld schedule, consisting of two equal current pulses (Fig. 3.12). The welding parameters used to prepare the spot weld samples are listed in Table 3.6. A current of 6.6 kA was chosen. The post heat treatment cycles for the single pulse-heat treated (single pulse-PB) and double pulse-heat treated (double pulse-PB) welds involve a typical paint bake (PB) heat treatment of the welded samples at 453 K (180 °C) for 20 min. Thermocouples were placed in the oven to monitor the temperature. The estimated heating rate was 5 Ks^{-1} and after the simulated paint bake thermal cycle, the sample was air-cooled.

The 22MnB5 steel was also welded using F1 16×5.5 electrodes with a holding force of 4.5 kN and welding parameters, as described in the VDEh SEP1220-2 standard [8]. Welding parameters employed to construct the weld growth curve are given in Table 3.7.
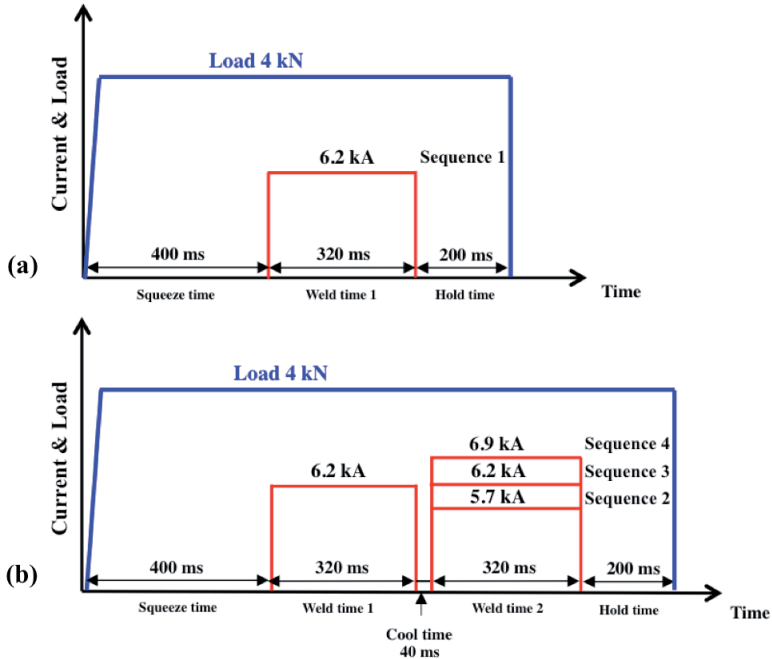
Fig. 3.11 Schematic representation of the (a) conventional and (b) double pulse RSW schemes for CR700Y980T-DH-GI steel.
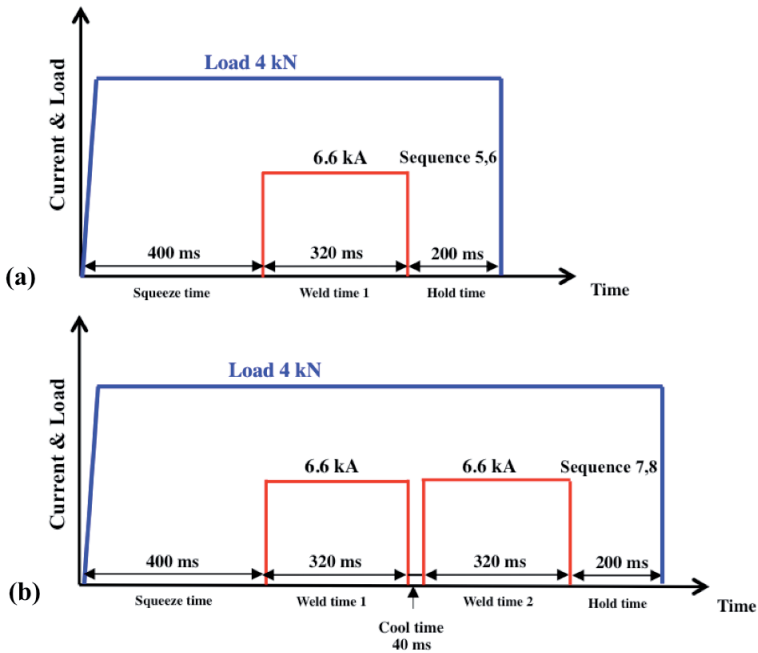
Fig. 3.12 Schematic representation of the welding schedules for single pulse and double pulse welds of CR700Y980T-DH-GI (studying the effect of baking cycle). Sequence 6 and 8 include a subsequent post welding paint bake cycle.

Table 3.6 Welding parameters to study the effect of baking cycle on CR700Y980T-DH-GI steel.

Weld	No. of pulses	Squeeze time (ms)	Current 1 (kA)	Weld time 1 (ms)	Cool time (ms)	Current 2 (kA)	Weld time 2 (ms)	Hold time (ms)	Heat treatment
Single pulse (sequence 5)	1	400	6.6	320	-	-	-	200	No
Single pulse- PB (sequence 6)	1	400	6.6	320	-	-	-	200	Yes
Double pulse (sequence 7)	2	400	6.6	320	40	6.6	320	200	No
Double pulse- PB (sequence 8)	2	400	6.6	320	40	6.6	320	200	Yes

Table 3.7 Resistance spot welding parameters for determining the weld growth curve.

	Minimum weld nugget size (4.25 ×√ t) (mm)	Squeeze time (ms)	Weld time (ms)	Hold time (ms)	I variation (kA)	I_{min} (kA)	I_{max} (kA)
22MnB5	5.2	550	340	250	4.4- 7.5	5.9	7
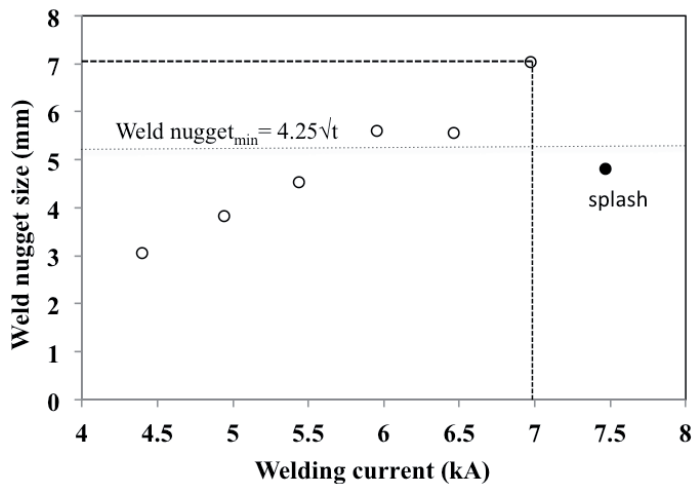
Fig. 3.13 Weld growth curve for the 22MnB5 steel, the solid symbols indicate splashing.

The weld growth curve for this steel is plotted in Fig. 3.13. The weld nugget sizes range from 3.0 mm to 7.0 mm. Splashing occurs at a current level of 7.5 kA.

The welding parameters used to produce welds are shown in Table 3.8. Sequence 9 is a single pulse resistance spot weld. Apart from the standard single pulse weld scheme, several double pulse weld schemes were applied, with a variation of the cool time between two pulses from 60 ms to 100 ms. The welding schemes are indicated schematically in Fig. 3.14.

Table 3.8 Welding parameters for 22MnB5 steel

Weld	No. of pulses	Squeeze time (ms)	Current 1 (kA)	Weld time 1 (ms)	Cool time (ms)	Current 2 (kA)	Weld time 2 (ms)	Hold time (ms)
Sequence 9	1	550	7	340	-	-	-	250
Sequence 10	2	550	7	340	60	7	340	250
Sequence 11	2	550	7	340	80	7	340	250
Sequence 12	2	550	7	340	100	7	340	250
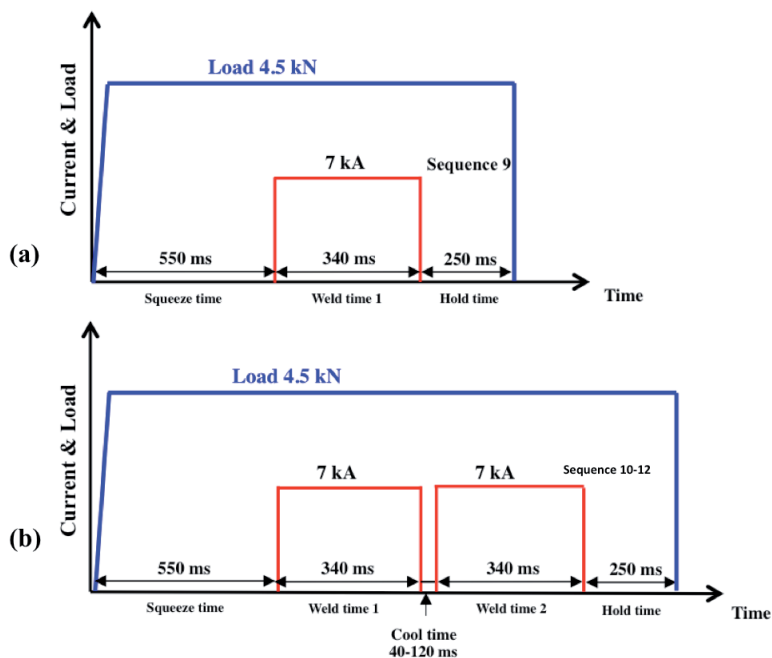
Fig. 3.14 Schematic representation of (a) single and (b) double welding schedules for 22MnB5 steel.

3.4 Experimental Procedures

3.4.1 *In-situ* phase fraction determination with synchrotron X-ray diffraction

Small block samples were prepared from the as-received CR700Y980T-DH-GI sheet, a 3rd generation 1 GPa AHSS with a sheet thickness of 1.3 mm in a cold-rolled and galvanized condition. The coating was removed by an acid etch. The blocks were homogenized at 1250 °C for 3 days in a vacuum chamber. The material was then annealed in a salt bath at (780 °C) for 30 minutes followed by water quenching to obtain a typical dual-phase ferritic martensitic microstructure (Fig. 3.15). Tensile specimens with a gauge length of
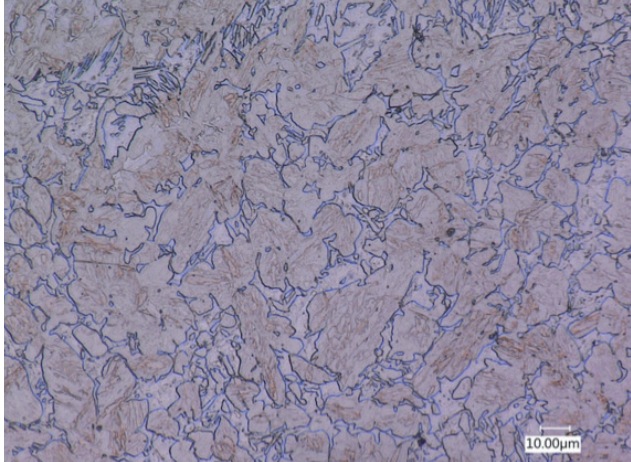
Fig. 3.15 Initial microstructure of the steel studied with in-situ synchrotron X-ray diffraction. Standard metallographic procedure with 2% Nital as an etchant was used. The brown and white colours represent martensite and ferrite, respectively.
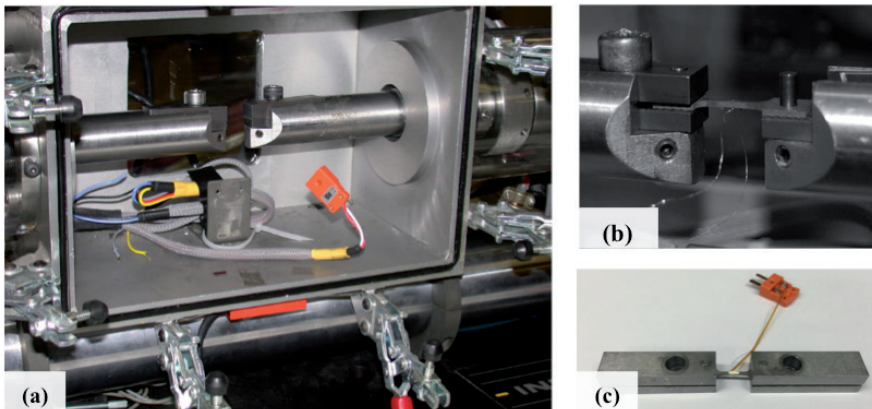
Fig. 3.16 Experimental set up at the ID11 beam line of ESRF facility in Grenoble, France, (a) ETMT chamber, (b) vertically located sample and (c) configuration of the sample with thermocouples attached and the CeO2 as a calibrant.

16 mm and a cross section of 1.5×1.0 mm^2 were electro-discharge machined from the homogenized and heat-treated samples.

Thermal cycles were generated by Ohmic heating with a direct current passing through the sample. Temperature control was established by a type-R thermocouple discharge welded to the centre of the specimen. The experimental configuration and a test specimen are shown in Fig. 3.16. To prevent decarburization during heating and cooling, the electro thermal mechanical testing (ETMT) was flushed with argon gas. The specimens were heated up to 1000 °C at a heating rate of 10 Ks^{-1}, kept for 10 seconds at that temperature to obtain a fully austenitic microstructure, and subsequently cooled at
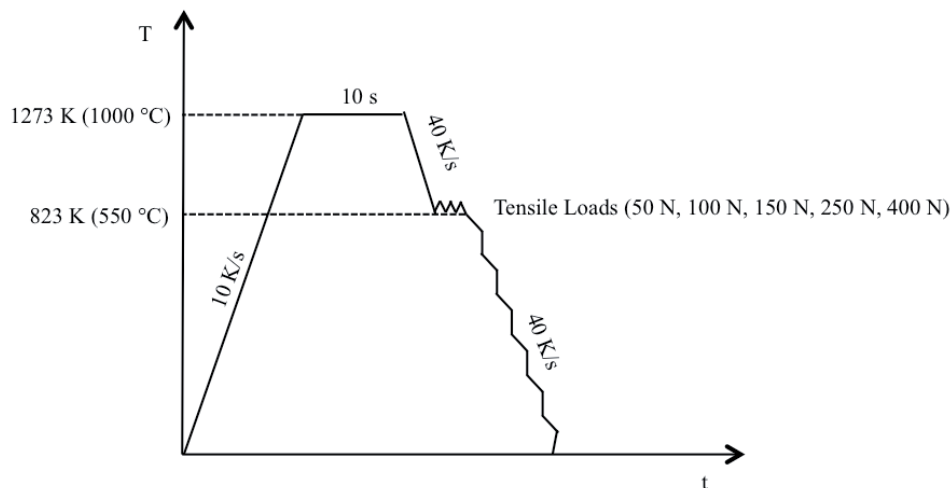
Fig. 3.17 Schematic illustration of the thermal-mechanical cycles applied.

a rate of 40 Ks^{-1} to room temperature. According to previous dilatometric experiments for the steel studied, M$_s$ in the absence of loading is 345 °C. The cooling process was interrupted for 7 seconds at 550 °C (*i.e.* above M$_s$) to apply an axial tensile force of 50, 100, 150, 250, or 400 N, which was held constant during further cooling to room temperature.

The loads of 50, 100, and 150 N for the given sample geometry are approximately equivalent to the stresses of 33, 67, and 100 MPa, which are below the yield stress of the material at 550 °C, while the 250 and 400 N loads (167 and 267 MPa) are equal to and higher than the yield stress, respectively. The loading axis was selected to be parallel to the transverse rolling direction (TD) and perpendicular to the rolling direction (RD). A schematic representation of the thermal-mechanical cycle is shown in Fig. 3.17. It should be mentioned that the martensitic transformation is known to occur very rapidly. Due to the experimental restrictions, such as detector frequency for collecting diffraction images and the high cooling rates required for martensitic transformation, diffraction patterns were recorded at 0.7 second intervals for each temperature – load treatment. The martensite start temperatures were estimated from the experimental data.

Data analysis was conducted with Fit2D image processing software developed at ESRF [10]. A typical 2D X-ray diffraction pattern is shown in Fig. 3.18. To convert the 2D data to 1D diffraction patterns, integration over the azimuthal angles at a constant scattering angle was performed. From the 1D patterns, a fit of each reflection to a pseudo-Voigt profile over the azimuthal angles was carried out. Volume fractions of the phases and austenite lattice parameters were acquired from the integrated intensities and the scattering angles of two FCC ($\gamma_{(200)}$ and $\gamma_{(220)}$) and two BCC ($\alpha_{(200)}$ and $\alpha_{(211)}$) phase rings [11]. Typical intensity – 2θ patterns of $\gamma_{(220)}$ and $\alpha_{(211)}$ at different times during cooling are shown in Fig. 3.19, and these were used for volume fraction calculations. The BCC phases include
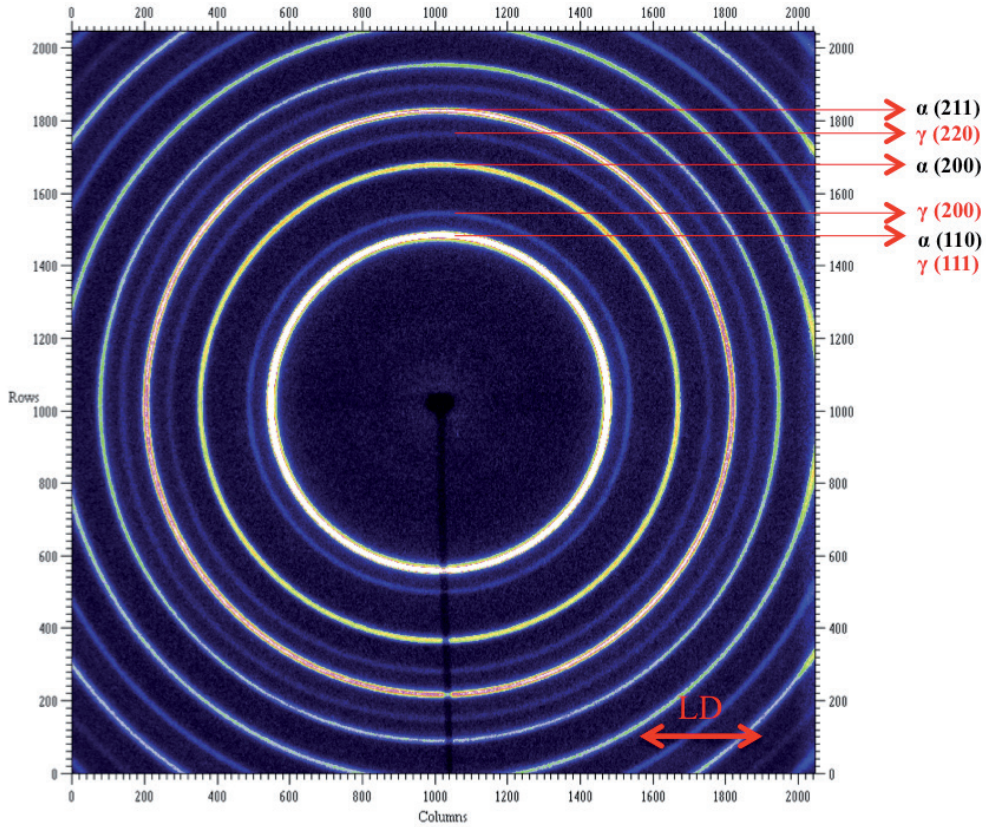
Fig. 3.18 2-D X-ray diffraction pattern. LD indicates the loading direction, which is perpendicular to the rolling direction of the steel.
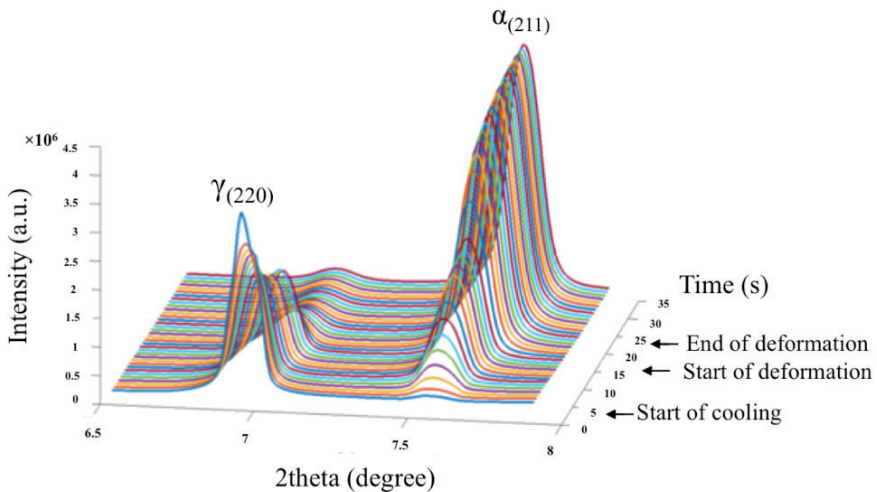
Fig. 3.19 Intensity- 2theta patterns for the sample subjected to 400 N load during cooling. The austenite peak ($\gamma_{(220)}$) intensity decreases and the BCC peak ($\alpha_{(211)}$) intensity increases during cooling. Arrows indicate the start of cooling, start and end of deformation.

several ferrite products such as grain boundary ferrite, Widmanstätten ferrite, bainitic ferrite, and also martensite. Although martensite has a BCT structure, considering the low carbon content of the steel, diffraction peaks of this phase cannot be distinguished from the BCC phase, due to the line broadening of the martensite peaks. The transformation temperatures and kinetics were derived from the volume fraction data.

3.4.2 Residual stress measurements with synchrotron X-ray diffraction

A schematic of the experimental arrangement for residual stress measurement is shown in Fig. 3.20. Strain scanning was performed in a radial direction with the step size of 900 μm at two different depth locations with a gauge length of about 600 μm, one at the weld centre depth location and the other at the depth of 0.65 mm (half of one plate thickness). The counting time per point was 10 min. The measurements were carried out on two in-plane directions at each point with a 90° rotation. The strain measurement at the centre line was stopped where the weld edge is reached. Schematics of the spot welds including the residual stress measurement locations are shown in Fig. 3.21.

In order to measure the stress free d-spacing (d_0), welds with similar welding schedules were electro-discharged machined from the weld. In addition, some vertical slits at positions of the weld centre (0 mm), 3 mm and 7 mm were made to release the stresses even further. The slit depth and width were 0.65 mm and 0.25 mm, respectively. Schematics of the reference samples and an actual reference sample are shown in Fig. 3.22.

3.4.2.1 Data pre-processing and analysis

A pseudo-Voigt profile was used to fit the measurements. Fig. 3.23 shows a typical peak fitting for the (200) BCC plane within the weld nugget, HAZ and the base material. For a fixed diffraction angle and a specific energy, the d-spacing (d_i) for a certain plane be can be obtained from Bragg's law. The strain (ε) can be derived by (Eq. 3.2):

$$\varepsilon_i = \frac{(d_i - d_0)}{d_0}. \tag{Eq. 3.2}$$

The stress can be calculated from the biaxial Hooke's law (Eq. 3.3) using the diffraction elastic constant (E) and Poisson ratio (ν) of the (200) planes, which are taken from the literature to be 169.3 GPa and 0.295, respectively [12].

$$\sigma_i = \left[\varepsilon_i + \nu \varepsilon_j \right] \left| \frac{E}{1 - \nu^2} \right|. \tag{Eq. 3.3}$$

The stress free lattice parameters of (200) BCC planes within different zones are shown in Table 3.9. The strains were calculated using the stress free lattice parameter at the same location. The instrumental error is in the order of 40 MPa.

3
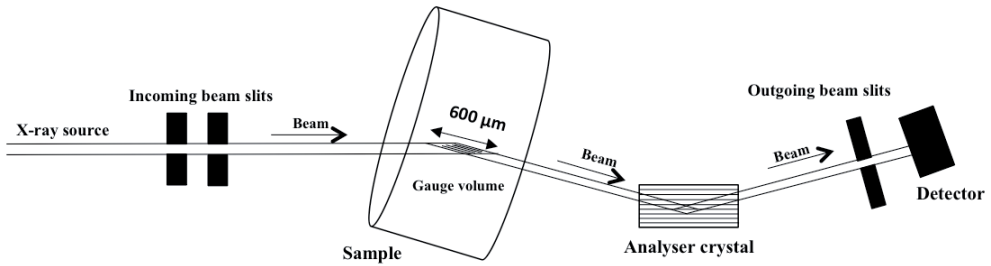
Fig. 3.20 Schematic set-up for the synchrotron X-ray diffraction measurement.
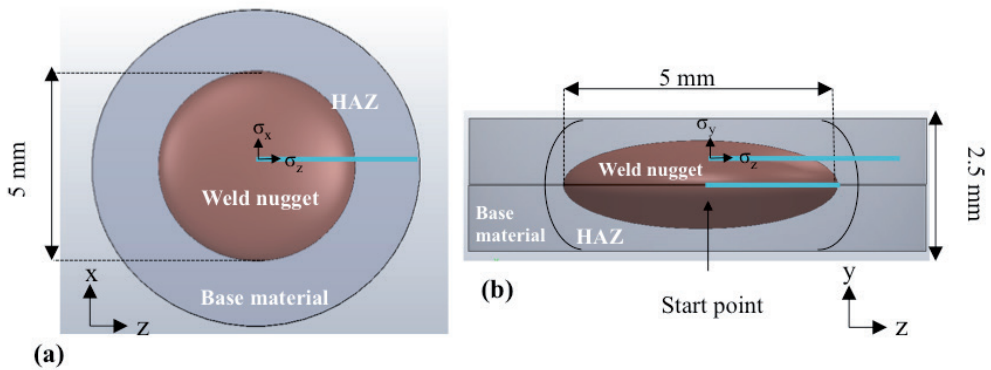
Fig. 3.21 Schematic representation of a welded sample (a) top view and (b) side view, the brownish shape represents the weld nugget. The blue lines indicate the positions at which residual stresses were measured.
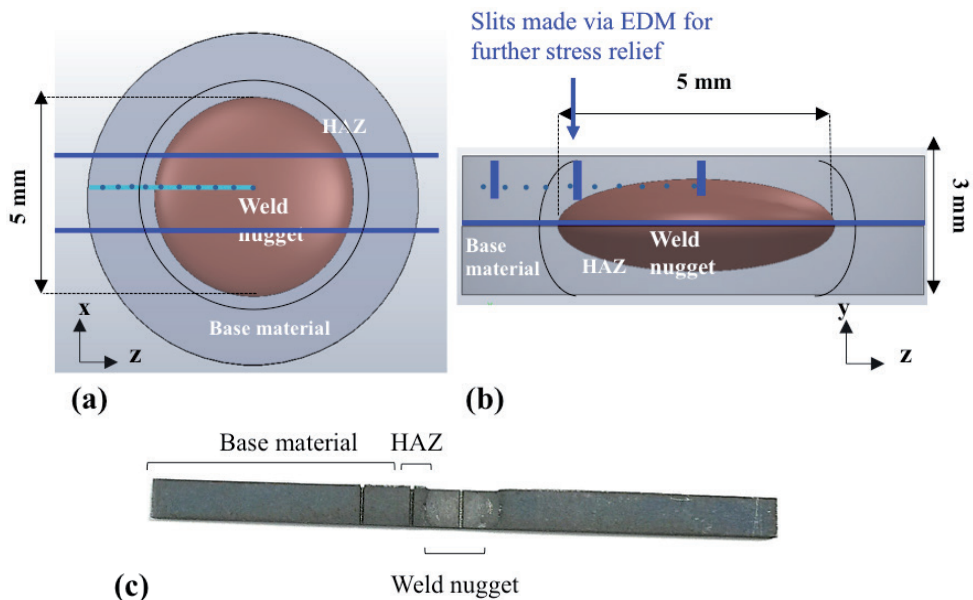
Fig. 3.22 (a) Schematic top view of a spot weld, the dark blue lines indicate the cut location for the reference sample, (b) schematic cross section view of a weld, the dark blue indicates the cut location for the reference sample preparation and the slits were made for further stress relief and (c) a top view of a reference sample.
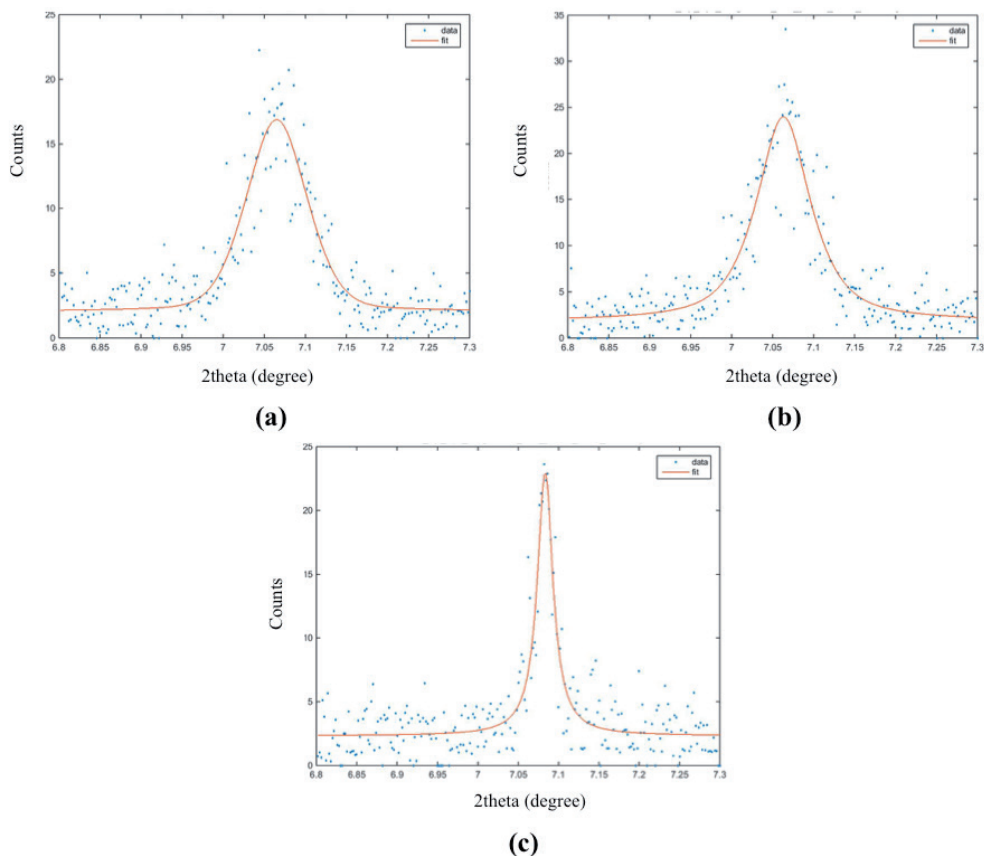
Fig. 3.23 Typical peak fitting of (200) BCC for (a) weld nugget zone, (b) HAZ and (c) base material of a resistance spot weld.

3.4.3 Micro-strain measurement using ring-core milling

In order to measure the micro-residual strains at the weld edge, a ring-core milling procedure was carried out at MPIE (Max-Planck-Institut für Eisenforschun) to assess the relaxation strain on a single pulse weld of CR700Y980T-DH-GI steel (sequence 1). Ring-core milling was carried out using an FEI Helios Nanolab 600 dualbeam FIB/SEM instrument with the help of a specifically developed automated procedure [13, 14]. The surface of the sample was *in-situ* sputtered (e-beam assisted deposition) with thin patterned dots (~50 nm) of Pt at the start of the experiment (Fig. 3.24 a), which act as high-contrast features for digital image correlation (DIC). These platinum dots enable high-resolution DIC tracking and do not interfere with the relaxation process, as they are much softer and more compliant than the steel. Milling was performed using an annular trench with an inner diameter of 5 μm, while employing a current of 0.92 nA at 30 kV. Scanning electron images are sequentially captured during the milling process (Fig. 3.24 b and Fig. 3.25). DIC image post-processing was also applied using the
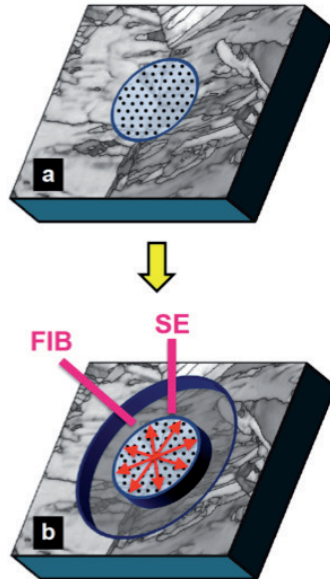
Fig. 3.24 Schematic representation of the ring-core milling technique (a) a pattern is applied to the sample surface, (b) an annular trench is milled. The remnant pillar is accordingly relaxed. Scanning electron (SE) images are sequentially captured during the milling process [13, 14].
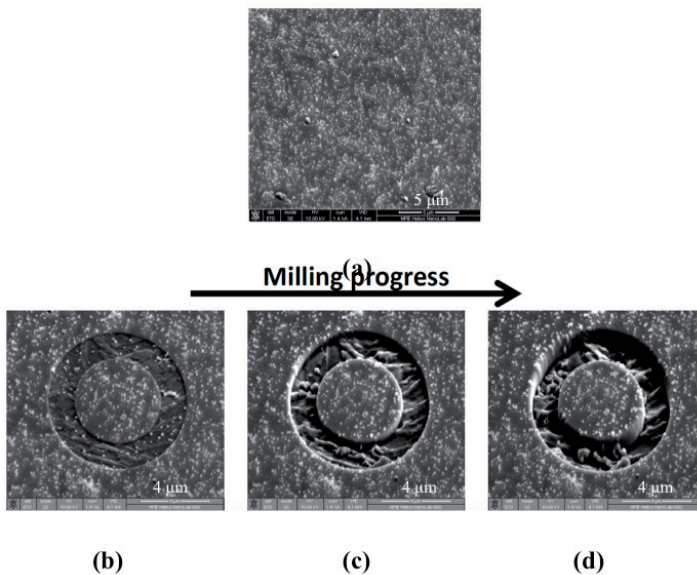
Fig. 3.25 SEM images taken from the weld edge of a single pulse welded CR700Y980T-DH-GI steel (sequence 1) (a) before milling and (b-d) during the milling process.
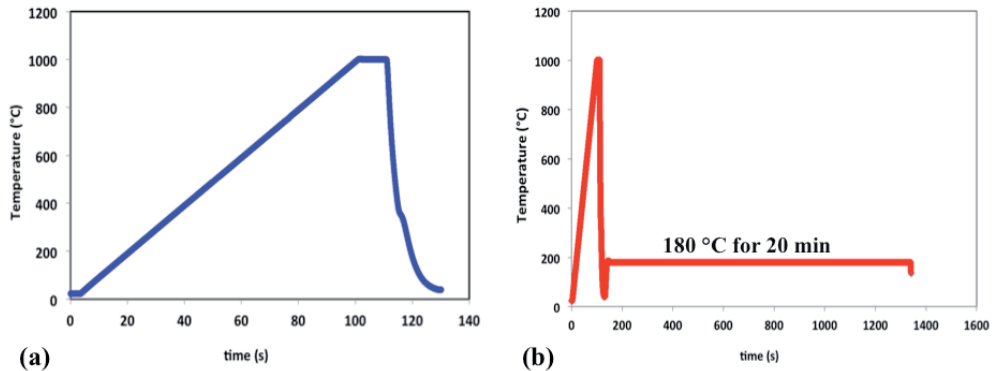
Fig. 3.26 Schematic of the thermal cycles applied via Gleeble to mimic (a) martensitic microstructure and (b) tempered martensite microstructure, representing a paint bake cycle.

ARAMIS software (V6.3.0, GOM GmbH), which also allows a 2D strain distribution analysis to be applied.

3.4.4 Fracture toughness measurements

In order to measure the effect of the baking cycle on the fracture toughness of a martensitic thin sheet of CR700Y980T-DH-GI, experiments were conducted as described below.

Rectangular sheets with dimensions of 200 mm × 45 mm were cut from the as-received advanced high strength steel, CR700Y980T-DH-GI. Thermal simulations were conducted using a Gleeble 3800 to mimic the entire thermal cycle of the heat affected zone in an as-welded sample and a heat treated (bake thermal cycle) sample. Samples were heated at the rate of 10 Ks^{-1}, maintained at a temperature of 1000 °C for 10 s, and then Helium quenched in order to obtain a fully martensitic microstructure. Half of the samples were heated to 180 °C and were kept at that temperature for 20 minutes to simulate a typical paint thermal cycle applied in the automotive industry. Temperature control was achieved by means of feedback from a R-type thermocouple discharge welded to the centre of the sample. For a certain thermal cycle, three samples were prepared. A schematic of the thermal cycles applied is shown in Fig. 3.26.

Double-edge notched test (DENT) specimens having a notch length of 9 mm and notch radius of 0.25 mm were electro-discharge machined from the heat treated sheets. The notch tips of all the samples were ground to grit 4000 perpendicular to the notch length direction to be able to track the crack visually. A schematic of a DENT specimen is shown in Fig. 3.27.

Pre-fatigue cracking was conducted by the compression-compression loading method to obtain two cracks with similar length in each sample. Pre-fatigue cracking was stopped when a crack extension of 1.3±0.02 mm was obtained at each side. The uniaxial tensile tests were performed on the DENT specimens while simultaneously the
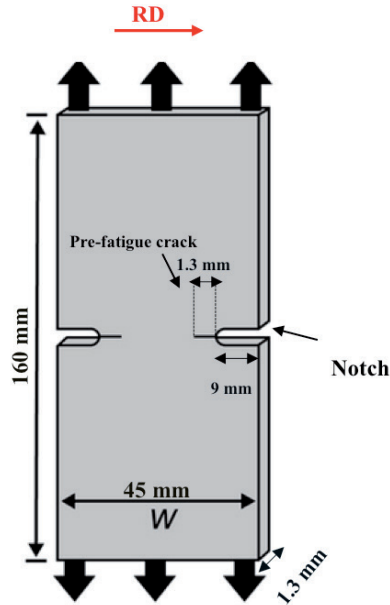
Fig. 3.27 Schematic of the Double edge notched tensile (DENT) specimen.
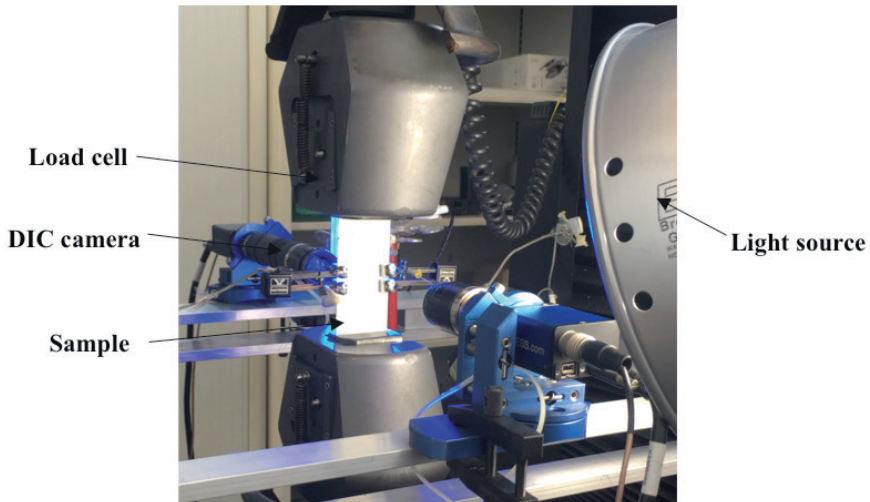
Fig. 3.28 The experimental set up for fracture toughness measurements, including camera arrangement for digital image correlation measurements.

Digital Image Correlation (DIC) technique was used to monitor the crack propagation and the deformation zone. The experimental arrangement is shown in Fig. 3.28.

A LIMESS Q-400-3D DIC system [15] along with a commercial software package Istra 4D was used to capture and analyse images at a frame rate of 8 Hz. Prior to measurement, the DIC camera was calibrated using 4 images of translated and rotated

planar dot pattern of known spacing. The accuracy of the displacement measurement was about 10^{-5} m.

Fracture toughness tests were performed on AN Instron 5500R 100 kN universal testing machine. The displacement signal was measured via two Instron extensometers. These extensometers have a standard gauge length of 12.5 mm that can be adjusted by changing the mounting position of the blades that contact the specimen. The tests were performed at a crosshead speed of 0.33 mm.s^{-1} and the tests were interrupted at certain points during loading to measure crack length and crack opening displacement (COD) by means of optical microscopy. Extensometer data for crack tip opening displacement (CTOD) approximation were compared with DIC and optical microscopy images.

3.5. Modelling of resistance spot welding

3.5.1 SORPAS modelling of single and double pulse welding

In addition to the experimental investigation, thermal cycles during resistance spot welding with single and double pulse weld schemes were determined using a commercial finite element code (SORPAS®) for CR700Y980T-DH-GI steel. The input data for the SORPAS simulations consisted of the welding parameters such as welding current, welding time and the applied force as well as the standard SORPAS database, which includes the temperature dependent properties of a conventional dual phase AHSS (DP1000 steel) (in appendix A, Fig. A.1). The grid size was 0.25×0.25 mm^2 and the time step was 1 ms. The boundary conditions in the model are defined with a function called tools. This function represents the connection to the welding machine that applies the current and the mechanical force. The mechanical module, thermal module, electrical module, contact modeling as well as the electro-thermo-mechanical couplings in this model are illustrated in [16]. In order to reduce the computation time, calculations were stopped after a holding time of 100 ms. The output data from the simulation is composed of temperature-time diagrams from which the peak temperatures, heating and cooling rates during welding can be derived. The weld nugget size and temperature distribution after weld time 1 (340 ms, explained in section 3.3) were also obtained from the simulation, as shown in Fig. 3.29. Simulations were validated by weld nugget size measurements (Fig. 3.30). In this investigation, data is extracted for a node within the fusion zone at a distance of 2.1 mm from the weld centre (Fig. 3.29). This area (weld edge) is of high importance in determining the mechanical performance of the spot welds.

3.5.2 Simufact modelling of single and double pulse welding

Due to limitations in prediction of temperatures higher than the liquidus using the SORPAS® platform, in later stages of the research another simulation platform, Simufact, was used to also predict the residual stresses of the spot welds.
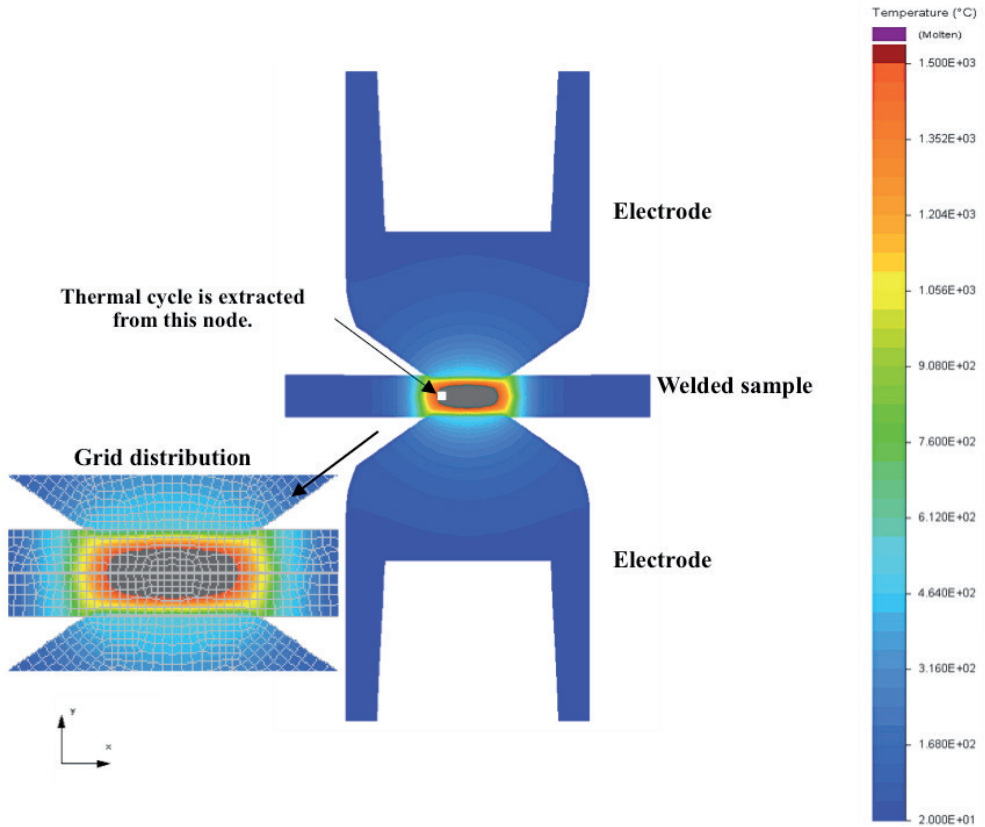
Fig. 3.29 Calculated temperature distribution after weld time 1, indicating the weld nugget for sequence 1. The thermal cycles are extracted from the node indicated by the white square. Grid distribution is also shown.
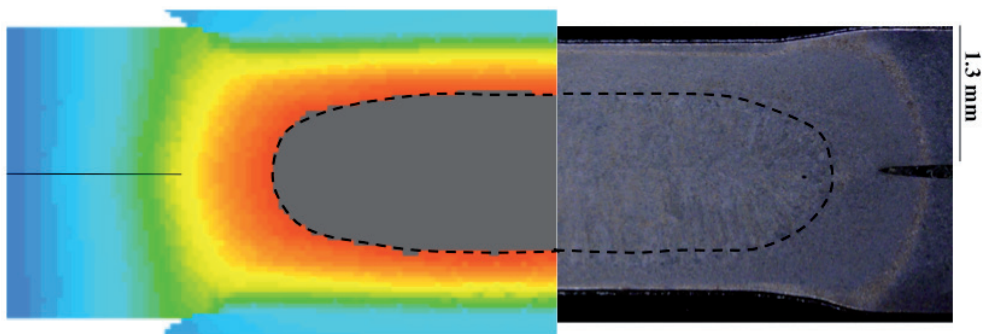
Fig. 3.30 Simulated temperature profile at peak temperature and a cross section of a single pulse resistance spot weld, the temperature contour is the same as Fig 3.29.

A 3D finite-element (FE)-based electrical-thermal-metallurgical-mechanical model was developed to compare with the experimental results of residual stresses by Dr. He Gao, Tata Steel Europe. After validation, the FE-model can be utilised for various spot welding conditions applied to the CR700Y980T-DH-GI steel. A sheet coupon with a dimension of $45 \times 45 \times 1.3$ mm^3 was created, meshed and assembled. The original mesh grid was $2 \times 2 \times 0.75$ mm^3. During simulation, a dynamic mesh refinement with a radius of 5 mm is applied to the sheet near the electrodes, where each cubic element was split into 8. The configurations of the simulation with grid distribution at room temperature and the peak temperature during welding are shown in Fig. 3.31. The time step is 0.02 s. The model is checked for time step independency. There are three constraint nodes at the corners of the bottom sheets to prevent sheet movement and the sheets are free to expand. A schematic representation of RSW and trends of electrical resistance and temperature in various components during welding are shown in Fig. 2.2. Considering both the bulk resistivity and the contact resistance between each two adjacent components, it can be seen that copper electrodes have the lowest value of electrical resistance, while the highest value is reached at the contact surface between the two metal sheets.

Material properties were calculated based on chemical composition in JMatPro and imported into the model. The temperature dependent material properties, such as thermal conductivity, specific heat capacity, Young's modulus, density, thermal expansion coefficient, electrical resistivity, flow stress and phase diagram are shown in appendix A, Fig. A.2 (a-h) [17]. A comparison of the temperature dependent material properties extracted from JMatPro and SORPAS is shown in Fig. A.1. The initial room temperature, heat conductivity and convection coefficients were defined to be 293 K, 30 W/K m^2 and 10 W/K m^2, respectively. A reference point was set on the centre-bottom of the lower sheet in order to align the lower electrode. An external force of 4 kN was applied on the upper electrode perpendicular to the sheet surface. The current and times for squeeze, weld and hold are defined in accordance with SEP 1220-2 [8] as shown in Fig. 3.11. This model includes the physics of Joule heating, heat transfer, phase transformation and solid mechanics, from which evolution of temperature, phases and stresses during resistant spot welding can be obtained. For modeling, constraints at three corners of the lower sheet are applied to prevent the moving of the sheets. The sheets are free to expand.

Fig. 3.32 shows the comparison of the simulated weld nugget and the cross section of a single pulse resistance weld. Good agreement was found between the simulated and experimental weld nugget size (difference < 4%) and shape.
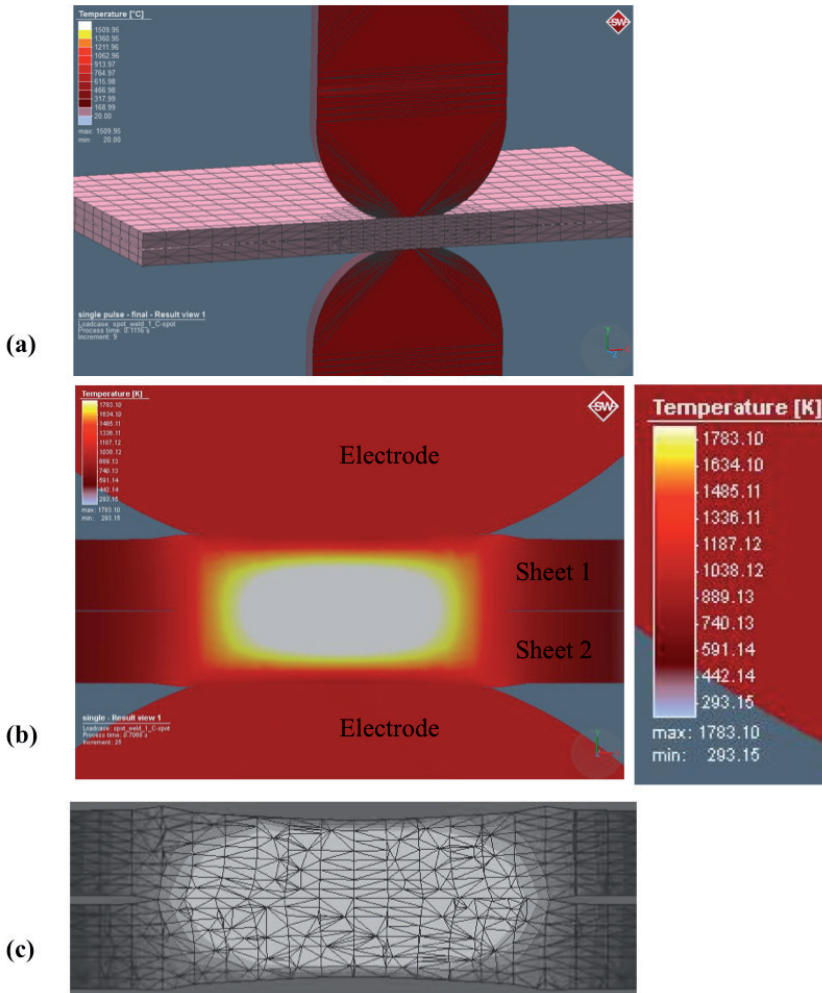
Fig. 3.31 (a) Grid distribution at the beginning of welding, (b) simulated temperature profile at the peak temperature when the weld pool is the largest and (c) grid distribution at the peak temperature for a single pulse resistance spot weld (welding sequence 1).
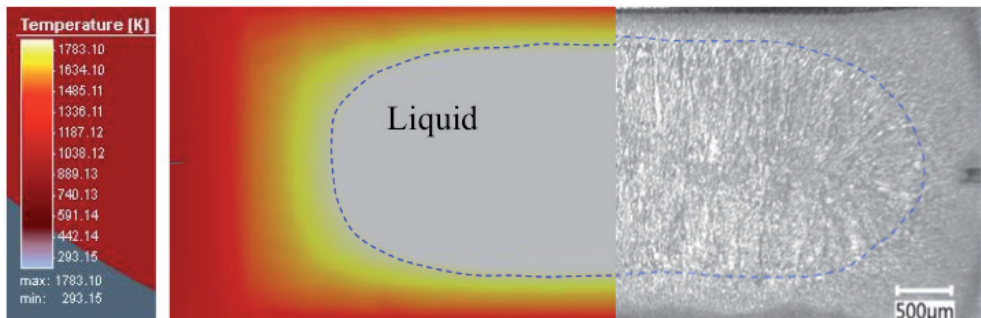
Fig. 3.32 Simulated temperature profile at the peak temperature and a cross section of a single pulse resistance spot weld.

Concluding remarks

In this chapter details are provided on the experimental methods and procedure and modelling aspects. The base materials were characterised and the RSW details were provided. The microstructural characterization techniques and mechanical testing of the welds have also been discussed. Details of the thermo-mechanical analysis of the steel studied using synchrotron X-ray diffraction (ETMT) and fracture toughness measurements are presented. The experimental procedures for residual stress measurements of the welds using *ex-situ* synchrotron X-ray diffraction and ring-core FIB milling are discussed. Two modelling platforms to predict the temperature profiles and residual stresses of the welds were considered and discussed. The procedures described in this chapter will be referred in the subsequent chapters, where results on the various aspects of resistance spot welding of AHSS are presented and discussed.

References

[1]   C. Cayron, *ARPGE: a computer program to automatically reconstruct the parent grains from electron backscatter diffraction data*. J Appl Crystallogr. 40 (2007) 1183-1188.

[2]   CrysTbox diffract GUI2.19 by Miloslav Klinger.

[3]   J.C. Labiche, O. Mathon, S. Pascarelli, M.A. Newton, G.G. Ferre, C. Curfs, G. Vaughan, A. Homs, D.F. Carreiras, *The fast readout low noise camera as a versatile x-ray detector for time resolved dispersive extended x-ray absorption fine structure and diffraction studies of dynamic problems in materials science, chemistry, and catalysis*, Rev. Sci. Instrum. 78(9) (2007) 091301-11.

[4]   A.P. Hammersley, S.O. Svensson, M. Hanfland, A.N. Fitch, D. Husermann, *Two-dimensional detector software: From real detector to idealised image or two-theta scan*, High Press. Res. 14(4–6) (1996) 235–248.

[5]   G.S. Jung, K.Y. Lee, J.B. Lee, H.K.D.H. Bhadeshia, D-W Suh, *Spot weldability of TRIP assisted steels with high carbon and aluminum contents*, Sci. Tech. Weld. Join. 17(2) (2012) 92–98.

[6]   E.M. van der Aa, M. amirthalingam, J. winter, D.N. Hanlon, M.J.M. Hermans, M. Rijnders, I.M. Richardson, *Improved resistance spot weldability of 3rd generation AHSS for automotive applications*, 11th International Seminar on Numerical Analysis of Weldability, Graz, Austria, Sep. 2015.

[7]   VDA 239-100 Material specification: *Sheet Steel for Cold Forming* (2016).

[8]   SEP 1220-2: *'Testing and documentation guideline for the joinability of thin sheet of steel-part 2: resistance spot welding'*, Technical report 08, VDEh standard (2007).

[9]   K.W. Andrews, *Empirical formulas for the calculation of some transformation temperatures*, Journal of the Iron and Steel Institute 203 (1965) 721-727.

[10]   A.P. Hammersley: *ESRF Internal Report*, ESRF98HA01T, FIT2D V9.129 Reference Manual V3.1, 1998.

[11]   N.H. van Dijk, A.M. Butt, L. Zhao, J. Sietsma, S.E. Offerman, J.P. Wright, S. van der Zwaag, *Thermal stability of retained austenite in TRIP steels studied by synchrotron X-ray diffraction during cooling*, Acta Mater. 53(20) (2005) 5439–5447.

[12]   R.K. Dutta, R.M. Huizenga, M. Amirthalingam, A. King, H. Gao, M.J.M. Hermans, I.M. Richardson, *In situ synchrotron diffraction studies on the temperature-dependent plane-specific elastic constants in a high-strength quenched and tempered structural steel*, Scr. Mater. (2013) 187-190.

[13]   M. Sebastiani, C. Eberl, E. Bemporad, G. Pharr, *Depth-resolved residual stress analysis of thin coatings by a new FIB-DIC method*, Mater. Sci. Eng. A 528 (27) (2011) 7901-7908.

[14]   F. Archie, M. Zeeshan Mughal, M. Sebastiani, E. Bemporad, S. Zaefferer, *Anisotropic distribution of the micro-residual stresses in lath martensite revealed by FIB ring core milling technique*, Acta Materialia 150 (2018) 327-338.

[15]   LIMESS webpage, 2017, Available from: http://www.limess.com/en/products/ digital-image-correlation.

[16]   D. Loveborn, *3D FE simulations of resistance spot welding, thesis*, KTH Royal Institute of Technology, Report KIMAB-2016-108 (2016).

[17]   Sente Software Ltd. (2005) '*A collection of free downloadable papers on the development and application of JmatPro*', http://www.sentesoftware.co.uk/biblio. html.

3

CHAPTER 4

Single and double pulse resistance spot welding

4.1 Single and double pulse welding of CR700Y980T-DH-GI steel[1]

The effects of single and double pulse resistance spot welding on the microstructural evolution of advanced high strength automotive CR700Y980T-DH-GI steel are presented in this chapter.

As discussed in chapter 2, in the newest generation AHSSs, even the largest weld nugget sizes have the tendency to show failure modes other than the desirable full plug failure when subjected to cross-tension strength (CTS) testing. During CTS testing, the crack initiates at the weld edge; the local microstructure of this zone therefore plays an important role in the mechanical performance of the welds.

The combined effect of high amounts of alloying elements in AHSSs and the high cooling rates in RSW (2000–4000 Ks^{-1}), result in the formation of a lath martensitic microstructure in the weld nugget zone. The lath martensite has a subgrain structure including packets, blocks, sub-blocks and laths [1, 2]. Different crystallographic lath variants can exist within a single prior austenite grain. Parallel laths with a pair of different variants form blocks, and parallel blocks with a common habit plane form packets. It has been reported that the prior austenite grain size (PAGS) and the variant selection have important influences on the mechanical performance of lath martensite structures [3–8]. A decrease in PAGS reduces the packet and block size of lath martensite and increases the strength of the steel [7]. In summary, the performance of the welds is affected by both the segregation of the alloying elements and the formation of the lath martensite substructure [9].

As mentioned in chapter 2, post pulsing is one of the most efficient means of modifying the microstructure and thus the mechanical properties of resistance spot welds. In this chapter, an analysis of elemental distribution and microstructural changes on the mechanical properties of the welds due to variation in second current pulse amplitude is reported. The results contribute to a better understanding of the metallurgical phenomena in resistance spot welding of advanced high strength steels.

4.1.1 Results
In this study, welds were prepared according to the welding sequences 1 to 4 as described in section 3.3. A primary welding current of 6.2 kA was selected. This current leads to

---

1 This chapter is based on the published scientific papers:
P. Eftekharimilani, E.M. van der Aa, M.J.M. Hermans, I.M. Richardson, Microstructural characterisation of double pulse resistance spot welded Advanced High Strength Steel, Sci. Technol. Weld. Join. 22(7) (2017) 545–554.
P. Eftekharimilani, E.M. van der Aa, M.J.M. Hermans, I.M. Richardson, The microstructural evolution and elemental distribution of a 3rd generation 1 GPa advanced high strength steel during double pulse resistance spot welding, Weld. World. 61(4) (2017) 691-701.
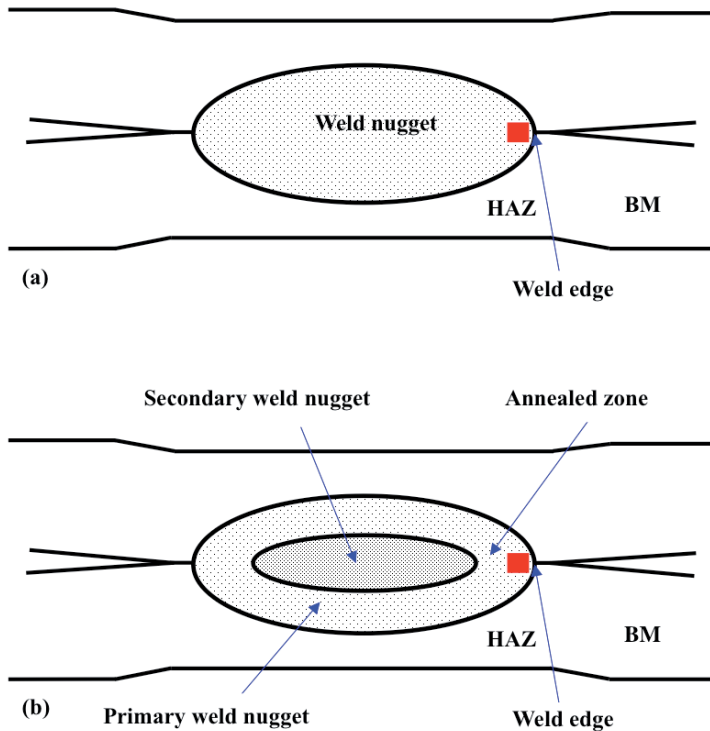
Fig. 4.1 Schematic representation of the cross-section of (a) a single pulse weld and (b) a double pulse weld, indicating the primary and secondary weld nugget in the welds. The dotted area is the (primary) weld nugget. The colored square at the primary weld nugget edge (notch) indicates the area of primary interest, where EBSD and EPMA scans were made.

a weld nugget diameter of 5.2 mm. The second current pulse for sequences 2, 3 and 4 are 5.7, 6.2 and 6.9 kA, respectively. The results of the investigation of these welds are presented in the following sections.

4.1.1.1 Microstructural characterisation

Schematic representations of a cross-section of a single pulse and double pulse welds are shown in Fig. 4.1a and b, respectively. During the first pulse, the primary weld nugget is produced. The second pulse results in a subdivision of the primary weld nugget into two zones. The outer zone is referred as annealed zone, which is solidified after the application of the first pulse and annealed during the second pulse. The inner zone is solidified after the application of the second pulse and referred as the secondary weld nugget.

Cross-section macrographs of the single and double pulse welds are shown in Fig. 4.2. In all the samples, the fusion zone and heat affected zone can be distinguished. As can be seen, the weld nugget of the single pulse weld (sequence 1) contains a typical

75
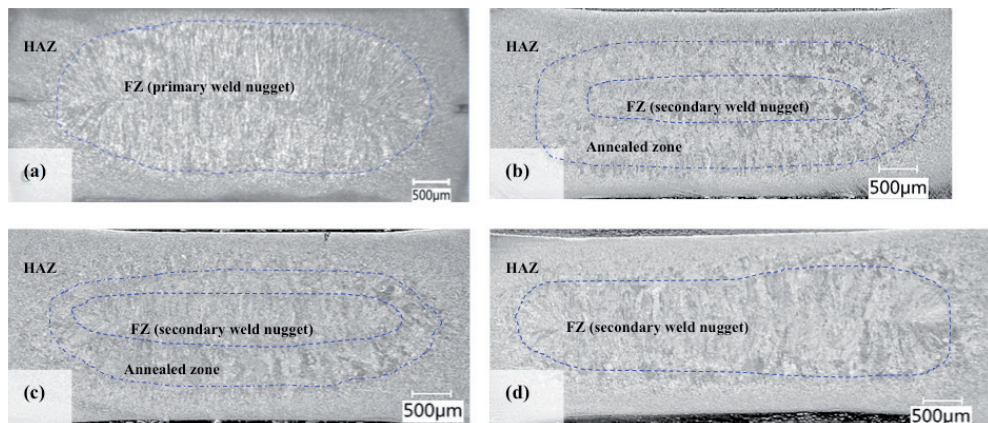
Fig. 4.2 Macrographs of the cross sections of the resistance spot welds (a) sequence 1, (b) sequence 2, (c) sequence 3 and (d) sequence 4.

Table 4.1 Weld nugget diameters for different sequences obtained from metallographic investigations.

Sequence	1	2	3	4
Primary weld nugget diameter (mm)	5.1	5.2	5.2	-
Secondary weld nugget diameter (mm)	-	3.7	4.3	5.7

columnar solidification structure (Fig. 4.2 a). The secondary weld nugget diameter increases with an increase in the second current pulse (Fig. 4.2 b and c). The zone between the primary and secondary weld nuggets is annealed and differs in size and microstructure for different welding sequences according to the second current pulse amplitude. The measured primary nugget diameters for sequences 1, 2 and 3 are similar; 5.1 mm, 5.2 mm and 5.2 mm, respectively. The secondary nugget diameter is 3.7 mm for sequence 2 (second pulse current amplitude of 5.7 kA). The size increases with increasing welding current. For sequence 3 (second pulse current amplitude of 6.2 kA), the secondary nugget diameter is about 4.3 mm. If the second pulse current amplitude is further increased to 6.7 kA (sequence 4), the diameter of secondary nugget exceeds that of the primary nugget (Fig. 4.2 d).

The microstructures of the single and double pulse welds are fully martensitic. The weld nugget in the single pulse weld and the secondary weld nugget show a martensitic solidification structure (Fig. 4.3 a). The annealed zones in sequences 2 and 3 also have a martensite microstructure. However, the martensitic structure in this area has become equi-axed (Fig. 4.3 b). Detailed images of the dendrites and equi-axed grains are shown in Fig. 4.4. Dendrites with a typical solidification grain orientation along the maximum temperature gradient at the weld nugget of a resistance spot weld are shown in Fig. 4.4 a and are depicted with higher magnification in Fig. 4.4 b. The annealed zone of a double
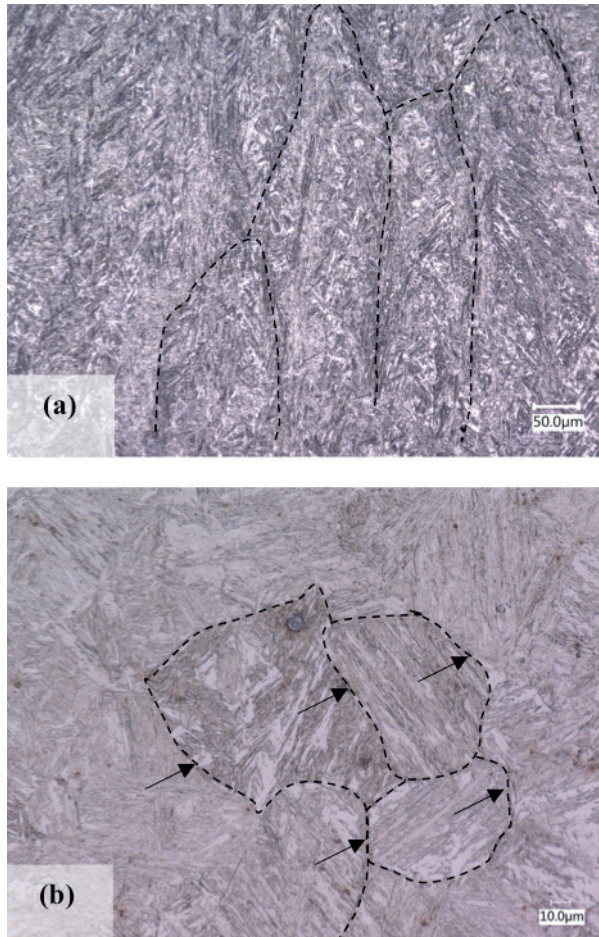
Fig. 4.3 Micrographs of a cross-section of the sequence 2 (double pulse weld), (a) secondary weld nugget showing a solidification dendritic structure and (b) annealed zone showing equi-axed grains (Dotted lines indicated by the arrows show the grain boundaries).

pulse weld reveals prior austenite grains with an equi-axed grain structure (Fig. 4.4 c and d). The existence of dendrites in some equi-axed grains at the interface of the secondary weld nugget and the annealed zone indicates partial melting of grains at the fusion line during the second current pulse (Fig. 4.4 d).

4.1.1.2 Elemental distribution

The measured elemental distribution for phosphorous, manganese and silicon at the weld edges of the primary weld nugget for the four welding sequences (indicated by the red square area in Fig. 4.1) is shown in Fig. 4.5, Fig. 4.6 and Fig. 4.7, respectively. The solidification structure is obvious for sequence 1 and 4 and the strong segregation of
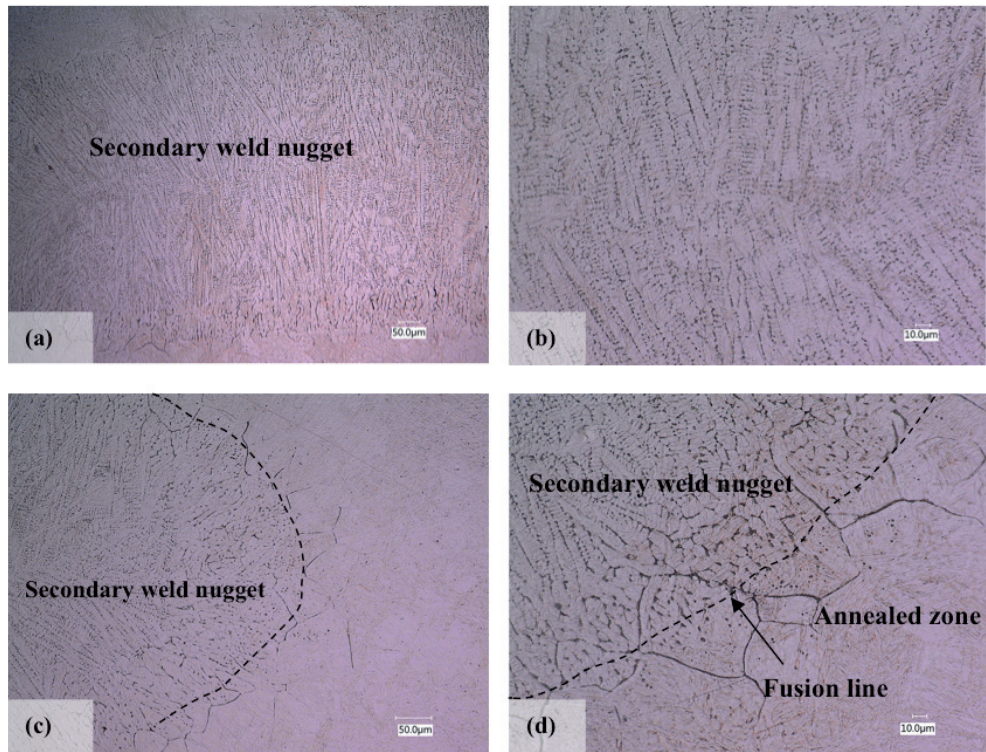
Fig. 4.4 Micrographs of the cross-sections of a double pulse welds (sequence 3) using improved etchant (Béchet-Beaujard reagent), (a) secondary weld nugget, (b) higher magnification of secondary weld nugget, showing dendritic structure (c) annealed zone and (d) higher magnification of the annealed zone showing equi-axed grains.

manganese, phosphorus and silicon is clearly visible (Fig. 4.5-4.7 a and 4.5-4.7 d). In sequence 2, the elemental segregations have been reduced in comparison with sequence 1 and 4. The distribution of manganese, silicon and phosphorus for this weld shows the presence of the elements at prior austenite grain boundaries as well as within the dendrite structure in some areas. Homogenising of the alloying elements during the second current pulse has occurred. The EPMA plots for sequence 3 show the lowest segregation of elements (Fig. 4.5-4.7 c). In this weld, like sequence 2, homogenisation of alloying elements has taken place and in just a few zones in the EPMA plots, the prior austenite grain boundaries can be seen; *i.e.* the areas with higher concentrations of manganese, silicon and phosphorous. Further quantitative study of the elemental segregation for different welds was preformed with line scans taken vertically at approximately 25 µm from the right hand side of the elemental plots. The line scans and the average and standard deviation of the results are presented in Fig. 4.8 and Table 4.2, respectively. The quantitative results of the line scans (table 5) show that the lowest standard deviation,
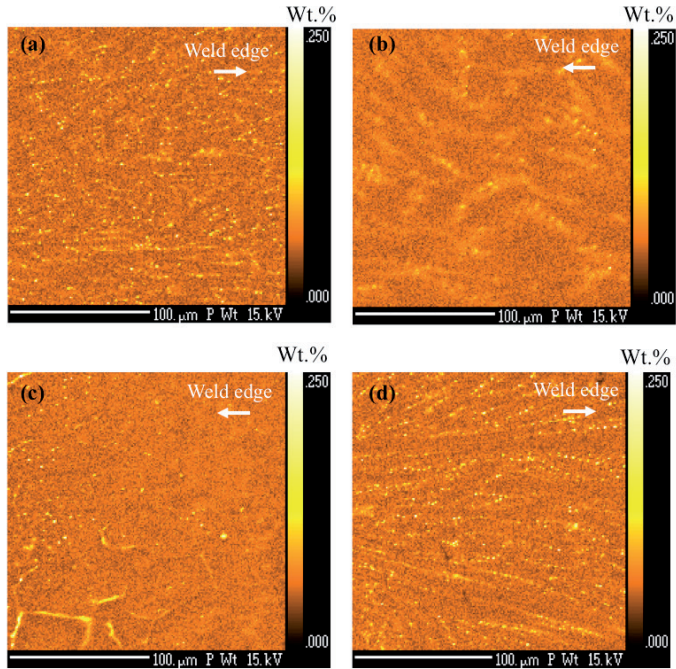
Fig. 4.5 Elemental maps of phosphorous taken at the primary weld nugget edge of (a) sequence 1, (b) sequence 2, (c) sequence 3 and (d) sequence 4.
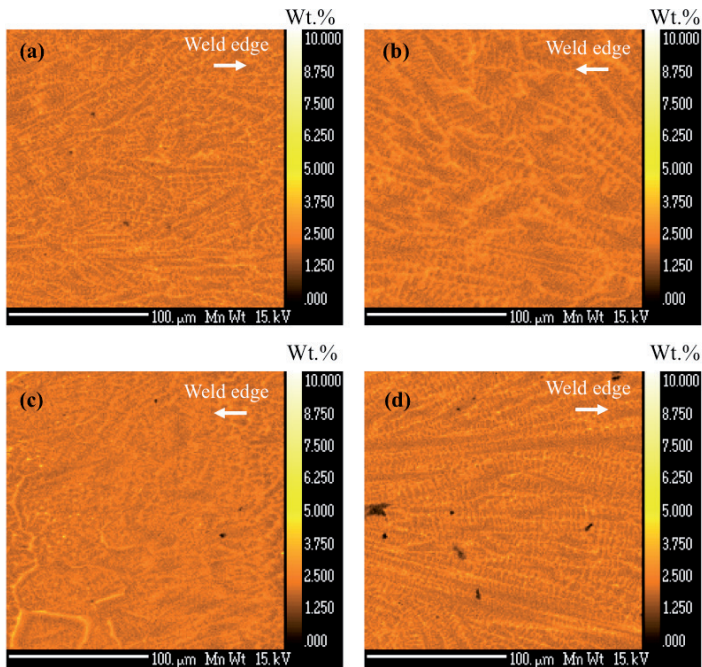
Fig. 4.6 Elemental maps of manganese taken at the primary weld nugget edge of (a) sequence 1, (b) sequence 2, (c) sequence 3 and (d) sequence 4.
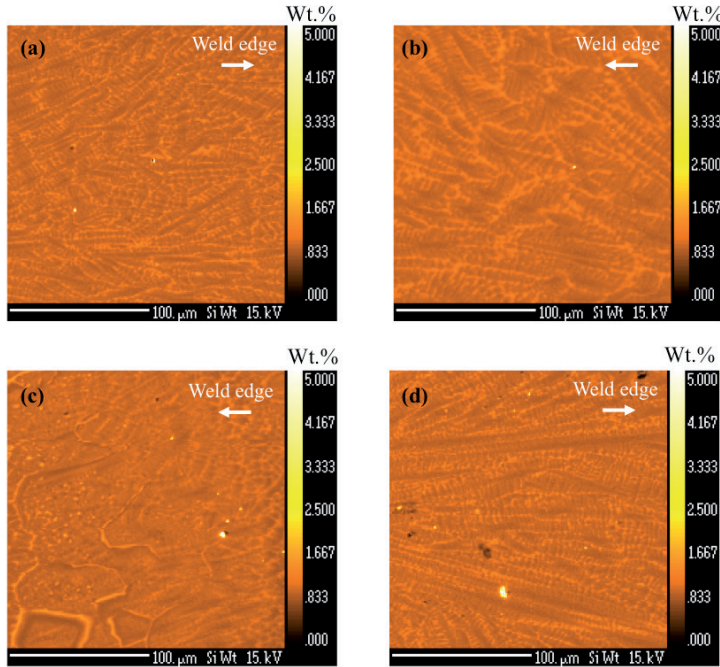
Fig. 4.7 Elemental maps maps of silicon taken at the primary weld nugget edge of (a) sequence 1, (b) sequence 2, (c) sequence 3 and (d) sequence 4.
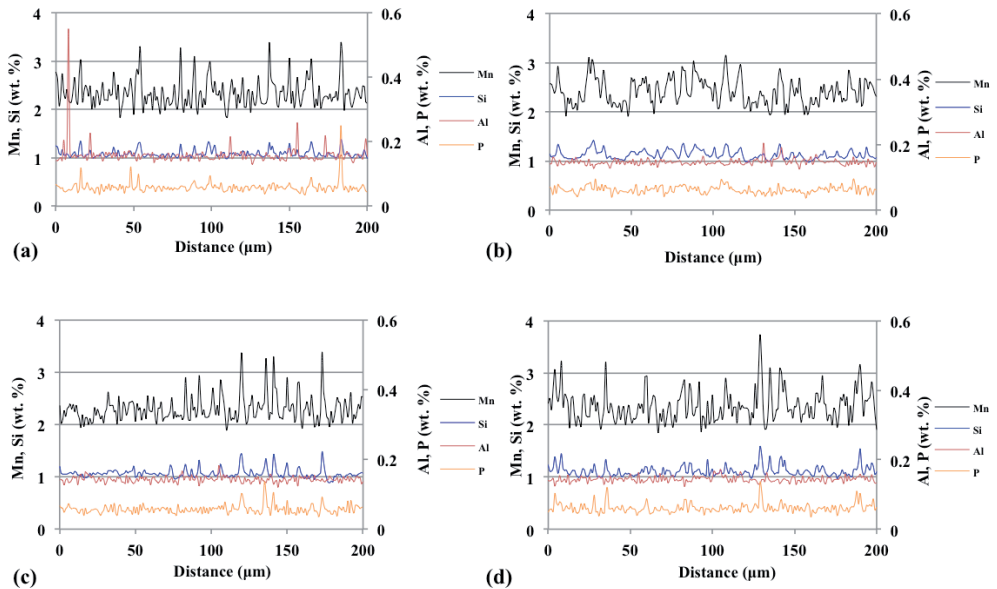
Fig. 4.8 Line scans taken vertically at approximately 25 μm from the right hand side of the elemental plots of (a) sequence 1, (b) sequence 2, (c) sequence 3 and (d) sequence 4.

Table 4.2 Average compositions and standard deviations obtained from EPMA line scans.

	Mn (wt.%) Average	Mn (wt.%) Stdev	Si (wt.%) Average	Si (wt.%) Stdev	P (wt.%) Average	P (wt.%) Stdev
Sequence 1	2.340	0.271	1.089	0.085	0.060	0.018
Sequence 2	2.369	0.265	1.116	0.088	0.062	0.011
Sequence 3	2.315	0.214	1.084	0.010	0.059	0.009
Sequence 4	2.309	0.337	1.084	0.098	0.062	0.025
Base material	2.255	0.262	1.015	0.074	0.055	0.008

meaning lowest segregation of the elements, is related to sequence 3, which was welded with two equal pulse currents.

The absolute average phosphorous level in the measured results is 0.060 wt.%, while the parent material analysis indicates 0.012 wt.%. The error is related to lack of EPMA calibration, but should not influence the trends observed with respect to the phosphorous level.

4.1.1.3 Martensite substructure and dislocation density

To obtain more detailed information concerning the morphology and crystallographic features of the lath martensite, inverse pole figure colour maps taken from the edge of the primary weld nugget of the welds (indicated by the coloured square in Fig. 4.1) were acquired by EBSD and are shown in Fig. 4.9. The prior austenite grains were reconstructed from the lath martensite structure, using the Kurdjumov–Sachs (K–S) orientation relationship, using ARPGE software [10].

The mean prior austenite grain sizes for sequence 1, 2 and 3 are 58 µm, 42 µm and 50 µm, respectively (Table 4.3). In further analysis, sequence 4 is not considered, as it will not deviate from sequence 1. In addition, also the ellipticity ((a-b)/a, where a and b are the major and minor ellipse radii, respectively) of the prior austenite grains was calculated. The mean ellipticity for the sequences is shown in Table 4.3. Sequence 1 shows the lowest circularity of the parent austenite grains and the inverse pole figure map confirms the typical solidification orientation of the grains at the weld edge. The ellipticity of prior austenite grains decreases for the double pulse spot welds and the grains within the annealed zone of the primary weld nugget typically changes to a more equi-axed structure.

Another feature to characterise the microstructure obtained is the block width (the block width measurement approach is presented at section 3.1.3). The block width, determined assuming the K-S orientation relationship between prior austenite grain and martensite and considering a misorientation of around 50° to 60°, is presented in Table 4.3. The highest block width is related to sequence 1. In double pulse welds, the block width is reduced.
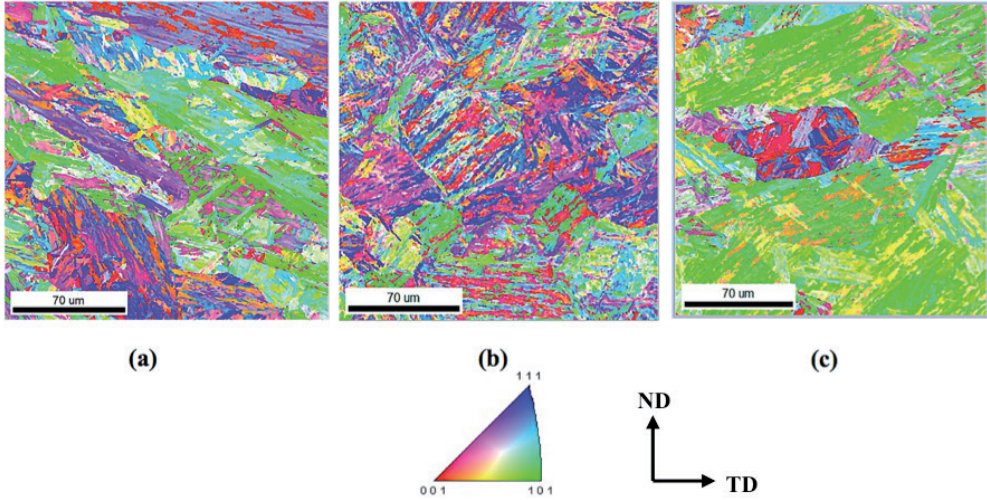
Fig. 4.9 Colour-coded inverse pole figure (IPF) maps with indexation at the primary weld nugget edge of (a) sequence 1, (b) sequence 2 and (c) sequence 3. ND and TD represent the normal direction and transverse direction to the rolling direction of the steel, respectively.

Table 4.3 Calculated values from EBSD maps for different welds.

	Sequence 1	Sequence 2	Sequence 3
PAGS (μm)	58 ± 4	42 ± 3	50 ± 6
Ellipticity	4.12	3.14	3.10
Average block width (μm)	1.76	1.3	1.6
Stdev block width (μm)	0.3	0.34	0.4
KAM	0.68	1.26	0.92
ρ_{GND} **(m^{-2})**	1.4×10^{14}	2.77×10^{14}	1.8×10^{14}

The change in block orientation is evident when double pulsing is applied. In the single pulse weld, the blocks are elongated (Fig. 4.10 a-b). In double pulse welds, the ellipticity of the prior austenite grains has reduced and the blocks are less elongated (Fig. 4.10 c-d).

The substructure of lath martensite subjected to high cooling rates, contains high densities of dislocation tangles. Kernel average misorientation (KAM) maps and distribution graphs of the KAM for the three weld sequences are presented in Fig. 4.11. The average KAM for these sequences is shown in Table 4.3. The geometrically necessary dislocation density (ρ_{GND}) is related to KAM by (Eq. 4.1) [11, 12]:

$$\rho_{GND} = \frac{\theta_{KAM}}{|\vec{b}| \cdot u \cdot n} \tag{Eq. 4.1}$$

where θ_{KAM} is the kernel average misorientation angle, $|\vec{b}|$ (Burgers vector) is 0.286 nm for the α Fe phase, u is the step size of the measurement and n is the number of nearest
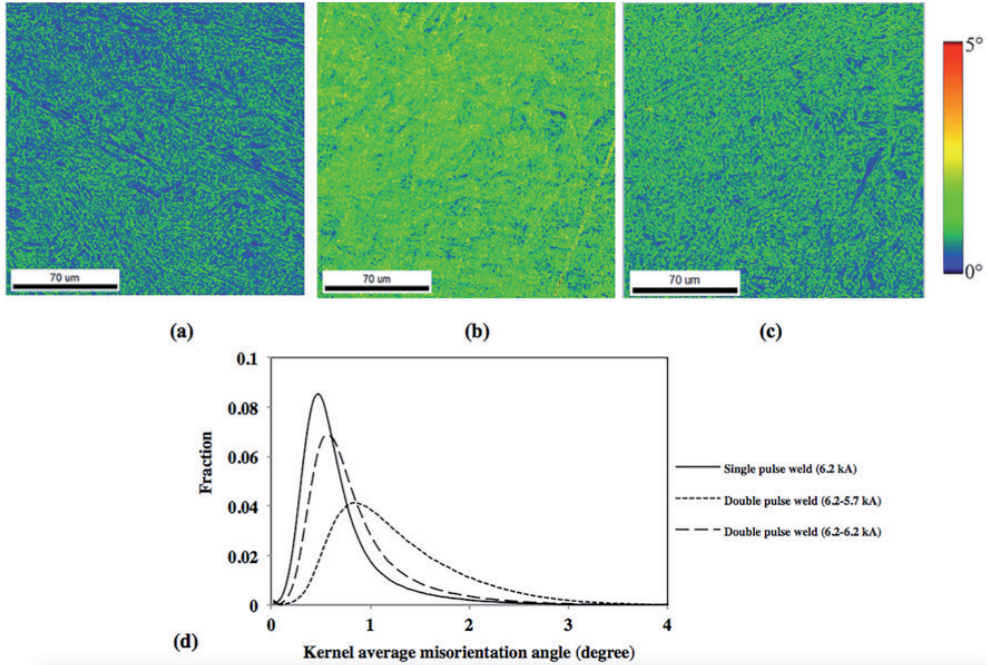
Fig. 4.11 Kernel average misorientation (KAM) maps (calculated with conditions of 5° and 2nd neighbour) at the primary weld nugget edge of the (a) sequence 1, (b) sequence 2, (c) sequence 3 and (d) distribution of KAM of different welds.

neighbours (considered 2 in this study). The calculated ρ_{GND} for the welds are shown in Table 4.3. Sequence 1 shows the lowest KAM and subsequently the lowest ρ_{GND}, whereas sequence 2 shows the highest KAM and ρ_{GND}. The distribution of KAM (Fig. 4.11 d) shows that when the average KAM increases, the distribution widens.

The overall EBSD results reveal that sequence 2 shows the smallest average prior austenite grains and block widths as well as the highest average KAM and ρ_{GND} and the ellipticity of the double pulse welds has decreased (Table 4.3) at the primary weld nugget edges. The most important change of microstructural features by double pulsing is the more equi-axed prior austenite grains at the weld edge of sequence 2 and 3.

4.1.1.4 Mechanical properties

The microhardness profiles of the CR700Y980T-DH-GI welds are shown in Fig. 4.12. The average weld nugget microhardness of sequence 1 is about 500 HV_{200g}. In the HAZ, the hardness drops steeply towards the hardness of the base material. It is shown that the HAZ of the sequence 2 and 3 are wider than sequence 1, due to the increased heat input. No significant microhardness changes are observed between different sequences, although double pulse welds show a slightly higher hardness in the weld nugget. The microhardness of the annealed zone of the welds is highlighted in Fig. 4.12. Sequence 1,
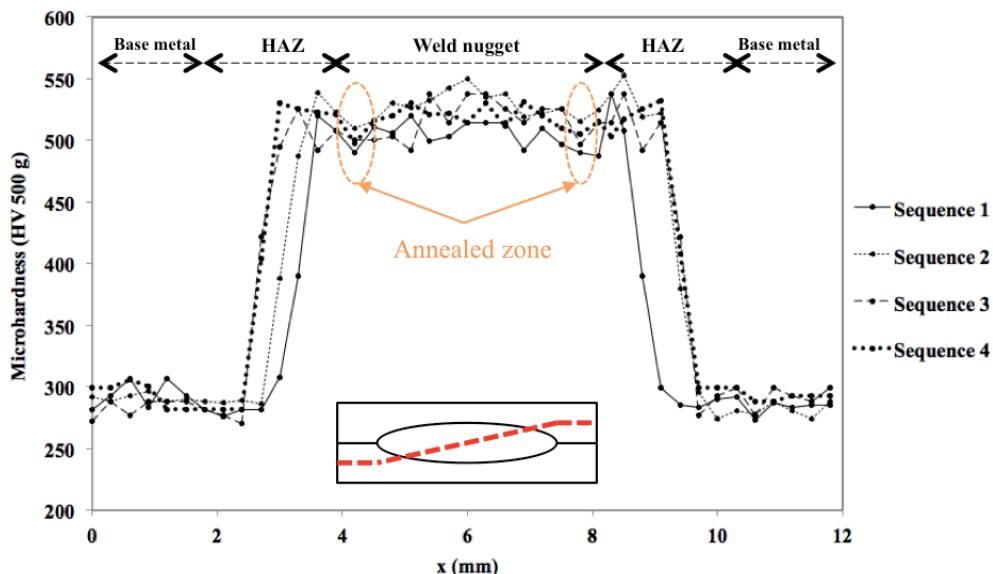
Fig. 4.12 Microhardness profiles of single and double pulse welds (Location of the hardness profile is indicated in the inset image.

2 and 3 welds have similar primary weld nugget sizes of about 5.1 mm. Sequence 4 has a lager weld nugget size of 5.7 mm.

The cross-tension strengths (as described in section 3.1.8) for the single and double pulse welds are shown in Fig. 4.13 and the measured properties are provided in Table 4.4. The CTS test results reveal that the double pulse welds show higher CT strength than the single pulse weld. The highest CT strength is related to sequence 3. The measured weld nugget sizes show that the sequences 1 to 3 have similar weld nugget diameters. However, sequence 4 has a larger weld nugget size due the high current in the second weld pulse (Table 4.4). Even with the wider weld nugget and HAZ widths after sequence 4, the CTS strength of the welds made with sequence 4 are clearly lower than for sequence 3 (Fig. 4.13). The addition of the second current pulse leads to an increase in the bearing force and displacement of the welds. The failure modes of the sequence 1, 2, 3 and 4 subjected to CTS testing are interfacial (average plug ratio of 0%), partial plug (average plug ratio of 35%), full plug (average plug ratio of 100 %) and partial plug (average plug ratio of 21%) failure, respectively (number of samples in each case was 3).

The tensile shear strength (TSS) test results for the welds are shown in Table 4.5. The results show that the double pulse welds also have a higher TSS. However, there is no significant difference between the TSS of sequence 2 and 3. Sequence 1 shows a partial plug failure during TSS testing, whereas in sequence 2, 3 and 4, full plug failure was obtained for TSS tests.
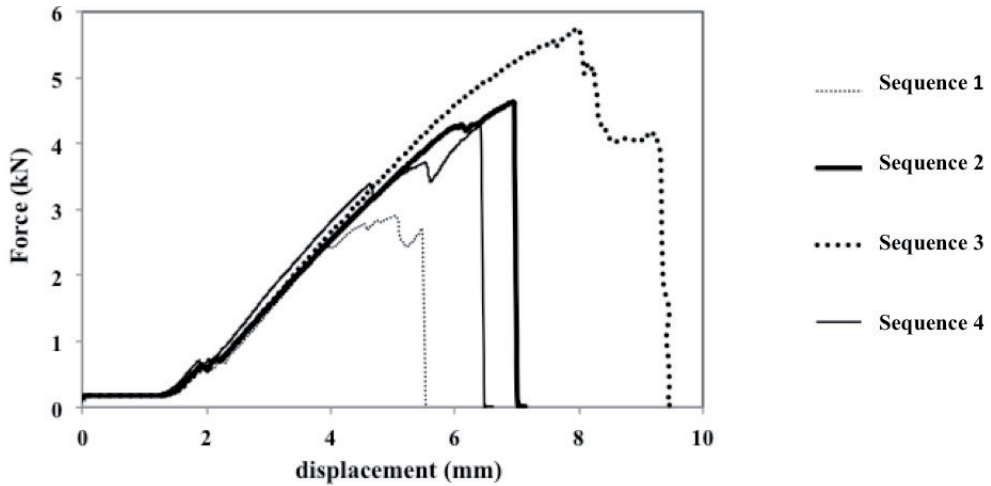
Fig. 4.13 Typical force versus displacement diagrams obtained from CTS tests of single and double pulse welds.

Table 4.4 Cross-tension Strength (CTS) results of the CR700Y980T-DH-GI welds.

Sequence	First current (kA)	Second current (kA)	Failure mode	Average weld nugget size (n=3) (mm)	Average CTS Strength, F_{CTS} (n=3) (kN)	Average plug ratio (n=3)	Average displacement at max. force (n=3) (mm)
1	6.2	-	Interfacial Failure	5.1±0.1	2.88±0.08	0%	4.9±0.4
2	6.2	5.7	Partial Interfacial Failure	5.1±0.1	5.12±0.4	35%±4%	7.7±0.8
3	6.2	6.2	Full Plug failure	5.2±0.1	5.63±0.2	100%	8.0±0.2
4	6.2	6.9	Partial Interfacial Failure	5.7±0.2	3.81±0.3	49%±2%	6.3±0.5

Table 4.5 Tensile Shear Strength (TSS) results of the CR700Y980T-DH-GI welds.

Sequence	First current (kA)	Second current (kA)	Failure mode	Average weld nugget size (n=2) (mm)	Average TSS Strength, F_{TSS} (n=2) (kN)	Average plug ratio (n=2)	Average displacement at max. force (n=2) (mm)
1	6.2	-	Partial Plug failure	5.1±0.1	19.8±0.4	83%	1.03±0.1
2	6.2	5.7	Full Plug failure	5.1±0.1	21.1±0.3	100%	1.10±0.2
3	6.2	6.2	Full Plug failure	5.2±0.1	21.2±0.3	100%	1.29±0.1
4	6.2	6.9	Full Plug failure	5.7±0.2	18.2±0.4	100%	1.04±0.3
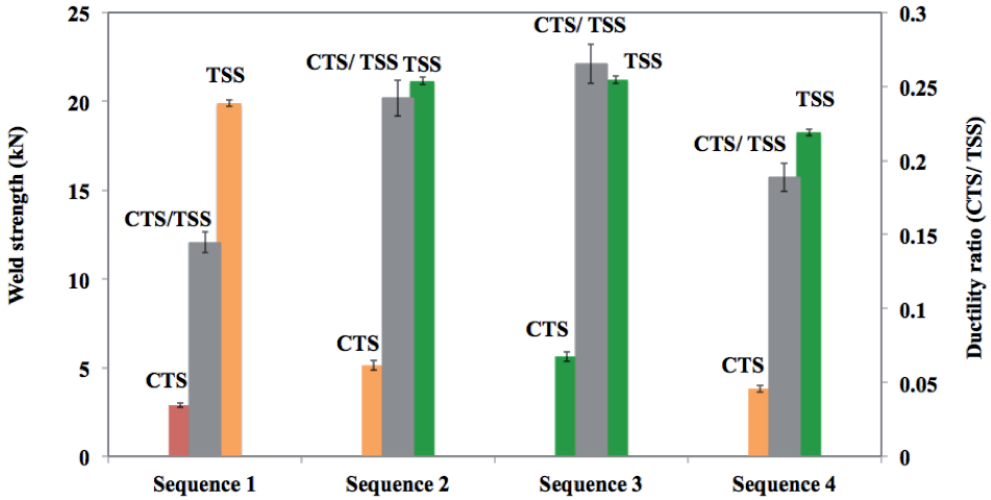
Fig. 4.14 Mechanical response of single and double pulse welds. Red indicates interfacial failure, orange partial plug failure and green full plug failure.
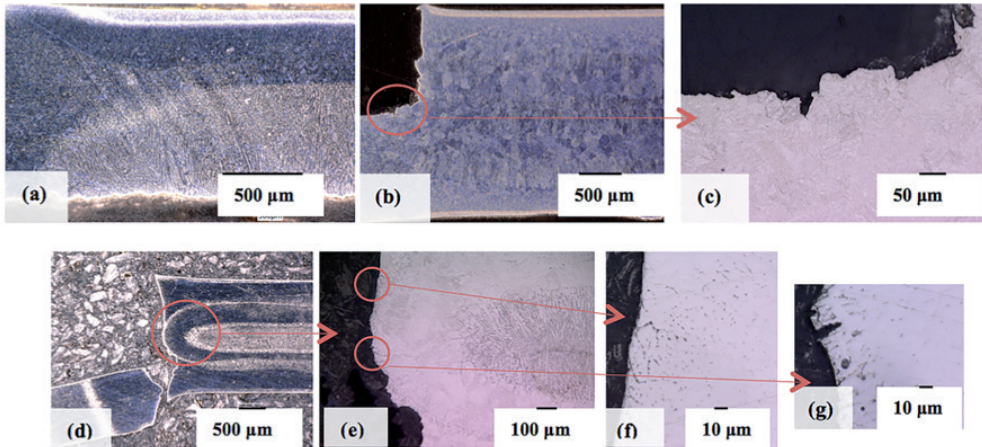
Fig. 4.15 Cross-sections of the fractured samples subjected to CTS testing, (a) sequence 1, (b) sequence 2, (c) higher magnification of b, (d) sequence 3, (e) higher magnification of d and (f-g) higher magnification of e.

From the combined CTS and TSS results, the ductility ratio (CTS/TSS) as an indication of the weld ductility is calculated. Sequence 3 has the highest ductility ratio (Fig. 4.14). The cross-sections of the fractured samples subjected to CTS testing are shown in Fig. 4.15, indicating that in sequence 1, weld metal failure occurred. In sequence 2, failure occurred in the annealed zone. The higher magnification image (Fig. 4.15 c) shows that the crack has propagated particularly along the prior austenite grain boundaries. A cross-section of sequence 3 weld shows that the failure has taken

place outside the primary weld nugget (Fig. 4.15 d-e) and the crack path initially followed the prior austenite grain boundaries and then continued as a ductile shear fracture in the HAZ material, which can be seen in Fig. 4.15 f-g.

4.1.2 Discussion

The single pulse welds show weld metal failure during CTS testing and the microstructure at the weld edge is dendritic and has a preferred orientation along the maximum thermal gradient. Microstructural changes in welds produced by double pulsing lead to improved mechanical response and failure modes. Simulated welding thermal histories at the primary weld edge of different sequences are shown in Fig. 4.16. At this location, the calculated peak temperature during the second pulse is about 1670 K for sequence 2 and around 1760 K for sequence 3. During the second pulse, the microstructure remains austenitic and recrystallisation (nucleation and grain growth) in the austenite phase occurs at the primary weld edge. Due to the higher second current pulse (heat input) of sequence 3 in comparison with sequence 2, the material in sequence 3 experiences higher temperatures at the primary weld edge (within the annealed zone) (Fig. 4.16). During the second pulse in sequence 2, the material at the weld edge remains austenitic. As the peak temperature is relatively low, grain growth of the austenite is limited (average prior austenite grain size of 42 μm). In sequence 3, due to the higher peak temperature, larger grains (average prior austenite grain size of 50 μm) are observed. The optical microscopy and EBSD results also confirm that the grain growth occurred during the second pulse in sequences 2 and 3. This changes the elongated grains to a more equi-axed shape.

It has been reported that there is a direct relationship between the prior austenite grain size and the block width in a lath martensite structure [6]. The results here confirm that the weld with smallest prior austenite grains contains the smallest block width (sequence 2). In case of sequence 1 and 3, the calculated mean prior austenite grain size is almost the same and the calculated block width is also comparable. However, sequence 1 and 3 differ in ellipticity, 4.12 and 3.10, respectively.

The increase in KAM and widening of the KAM curves in double pulse welds (Fig. 4.11) reflect that the grain size decreases and the ρ_{GND} increases. It has been reported that in low carbon lath martensite, the dislocation density increases with prior austenite grain refinement [13]. This observation has been confirmed in the present study. The larger prior austenite grain size of sequence 3 in comparison with sequence 2, which is attributed to the higher second current pulse, results in the lower ρ_{GND} of lath martensite in this weld. In general, a refined microstructure (*i.e.* small prior austenite grain and block width) will result in improved mechanical properties [3- 8]. This means that the microstructure of sequence 2 should be the most favourable.

The elemental partitioning at the weld edge is also an important factor that determines the mechanical properties during cross tension strength (CTS) testing of

resistance spot welds [14]. In the double pulse welds (sequence 2 and 3), redistribution of phosphorous, manganese and silicon takes place during the second current pulse. As sequence 3 experiences the highest peak temperature during the second pulse, the redistribution of phosphorous in this weld is most pronounced, indicated by a low standard deviation.

The diffusivity for phosphorous [m²s⁻¹] in austenite is given by Eq. 4.2 [15, 16]:

$$D_P^\gamma = 0.01 \times 10^{-4} \exp\left\{-\frac{184200}{RT}\right\}, \qquad\qquad \text{(Eq. 4.2)}$$

where R is the gas constant and T is the absolute temperature.

According to the temperature profile obtained by simulation (Fig. 4.16), the temperature at the edge of the weld produced using sequence 2 during the second current pulse amplitude of 5.7 kA reaches 1670 K and remains approximately constant for 25 ms. The calculated diffusivity of phosphorous in austenite at this temperature would be 1.73×10^{-8} m²/s. In case of sequence 3, the weld edge temperature during the second current pulse is about 1760 K for 25 ms. The calculated phosphorous diffusivity is 3.41×10^{-8} m²/s.

The characteristic diffusion length (m) is given by Eq. 4.3:

$$x = \sqrt{D_P^\gamma \cdot t}, \qquad\qquad \text{(Eq. 4.3)}$$

where t is the diffusion time. The calculated characteristic diffusion length during the second pulse for sequence 2 is about 20 μm and for sequence 3 is about 30 μm. Thus, the calculations also confirm that the reduction in phosphorus segregation at the weld edge in sequence 3 is higher than sequence 2.

During CTS and TSS testing, cracking initiates from the weld edges. The crack path is dictated by the local microstructure and the elemental distribution in this area. In this work, it is shown that double pulsing during RSW affects the lath martensite microstructure and the elemental distribution at the primary weld nugget edge of the welds over the entire annealed zone. The specific temperature cycle of sequence 2 with a relative low peak temperature at the weld edge of the primary weld nugget results in the smallest prior austenite grains and block widths and the highest KAM and ρ_{GND}. However, this temperature does not result in complete redistribution of phosphorous. In sequence 3, where a higher current amplitude (*i.e.* higher temperature) is applied during second pulsing, the phosphorous distribution is improved. However, at the same time somewhat larger prior austenite grain sizes, block widths and lower KAM and ρ_{GND} were found. Grain size and phosphorous distribution are two competing mechanisms in the area of interest. The peak temperature should be limited to avoid excessive grain growth (sequence 2), whereas from the phosphorous distribution point of view, a
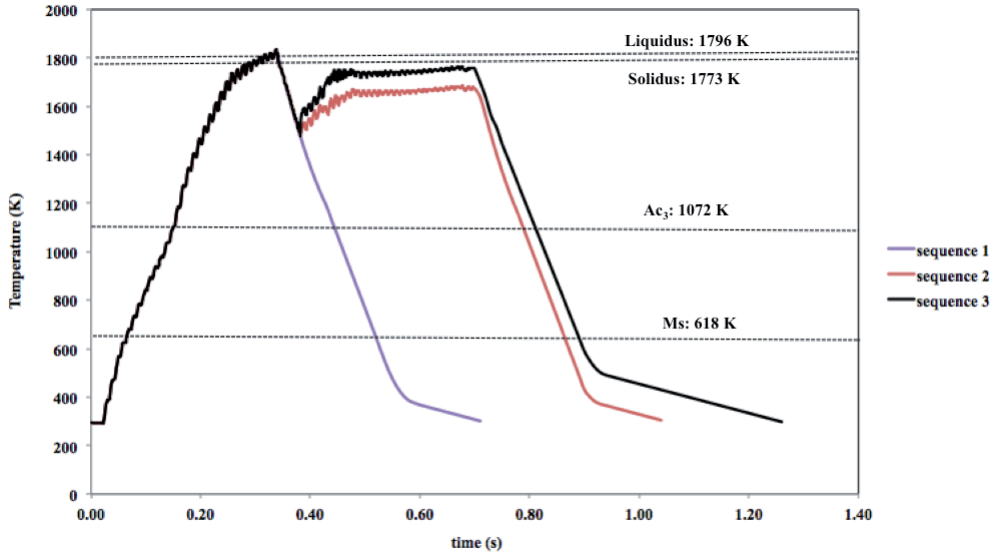
Fig. 4.16 Simulated thermal histories at the primary weld edge of different welds.

high temperature is required (sequence 3). The mechanical testing of welds shows that sequence 3 has the highest CTS and TSS. It appears that the fracture path always follows prior austenite grain boundaries, where the phosphorous is segregated. A clear example of phosphorous segregation at the prior austenite grain boundaries is shown in Fig. 4.5c. Therefore, phosphorous redistribution is highly likely to play a dominant role in determining the mechanical properties of the welds examined.

4.2 Single and double pulse resistance spot welding of 22MnB5 steel

4.2.1 Results

In order to improve the resistance spot weldability of an ultra high strength hot stamping boron steel (22MnB5 steel), double pulse welding was applied. A selected set of welding experiments on 22MnB5 hot stamping steel has been conducted to confirm the results obtained from single and double pulse welding of the CR700Y980T-DH-GI steel. In this study, the welding sequences 9 to 12 as described in section 3.3 were applied. A primary welding current of 7 kA was selected. The second current pulse amplitude was also 7 kA. The cooling time between two current pulses was varied from 60 ms to 80 ms and 100 ms. The effect of the cool time on the microstructure and mechanical performance of the welds was studied.

A typical cross-section of a double pulse resistance spot welded 22MnB5 steel is shown in Fig. 4.17. Fig. 4.17 b shows the microstructure of the secondary weld nugget
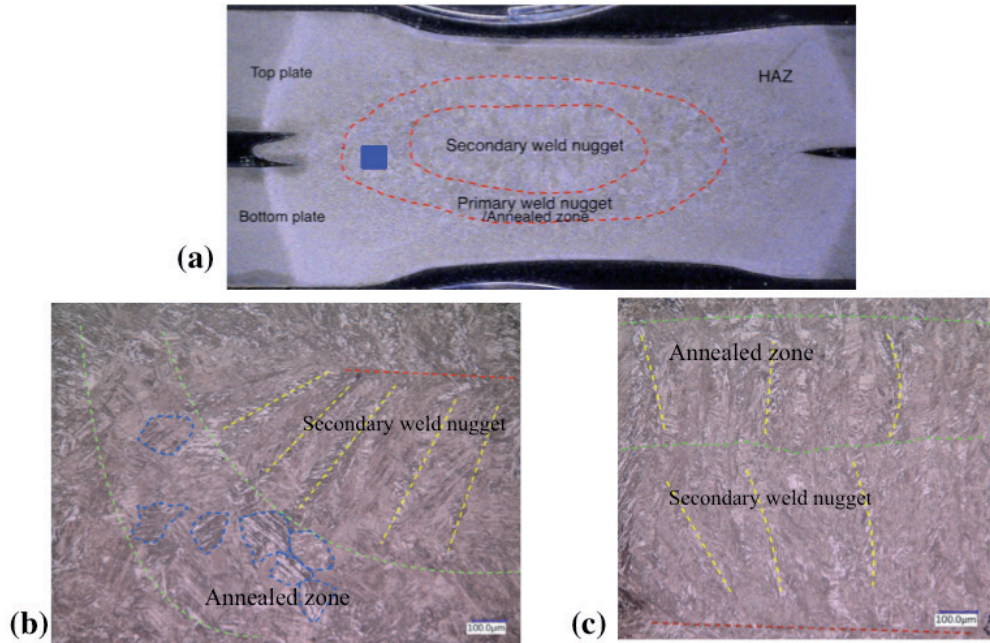
Fig. 4.17 (a) A typical cross-section of a double pulse weld of hot stamping steel and (b & c) higher magnification of the annealed zone and secondary weld nugget for welds subjected to various cooling times, (b) a double pulse weld with the cool time of 80 ms showing equi-axed structure in the annealed zone (sequence 11) and (c) a double pulse weld with the cool time of 100 ms representing a dendritic structure within the annealed zone (sequence 12).

and the annealed zone of sequence 11, a double pulse weld subjected to a cooling time of 80 ms. The microstructure of the annealed zone is martensitic and consists of equi-axed grains. In the case of sequence 12, the annealed zone has a martensitic microstructure with elongated grains (Fig. 4.17 c).

A typical microhardness profile of resistance spot-welded 22Mn5B steel is presented in Fig. 4.18. A drop in the microhardness in the sub-critical HAZ (HAZ softening) was measured. It should be mentioned that there was no considerable difference in the microhardness profiles of single pulse (sequence 9) and double pulse welded 22MnB5 steel (sequence 10-12).

The force-displacement curves obtained from CTS testing of these welds are shown in Fig. 4.19. The single pulse weld (sequence 9) shows the lowest load and displacement with a partial interfacial failure (PIF) mode. Sequences 10 and 12 also show partial interfacial failure (PIF) modes. Sequence 11 (the weld with the cooling time of 80 ms) shows the highest load and displacement with a full plug failure (PF) mode. The CTS testing performance of the weld has been improved by double pulse welding. In the case of sequence 12, a double pulse weld with a cooling time of 100 ms between the two
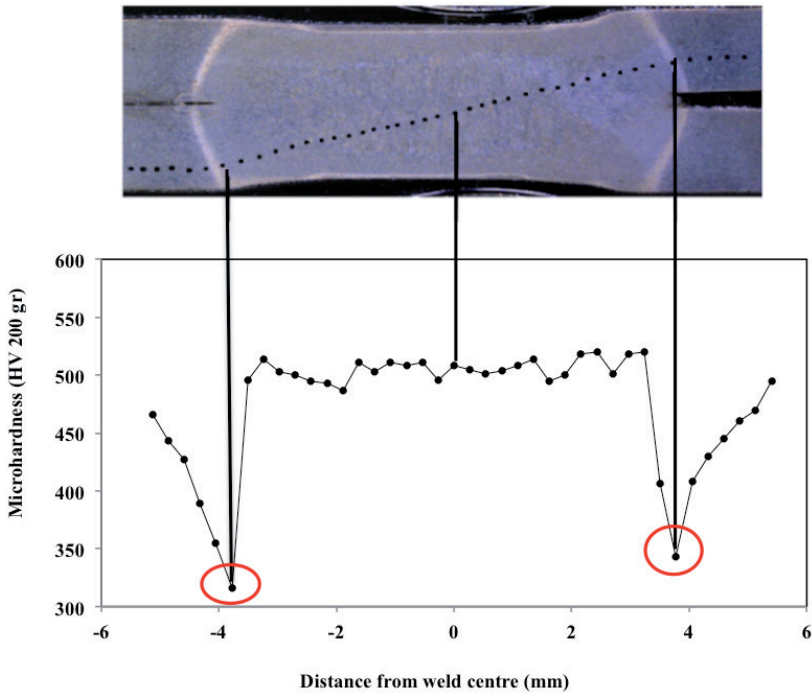
Fig. 4.18 A typical microhardness profile of a resistance spot welded 22MnB5 steel. The red shapes indicate the HAZ softening zone.
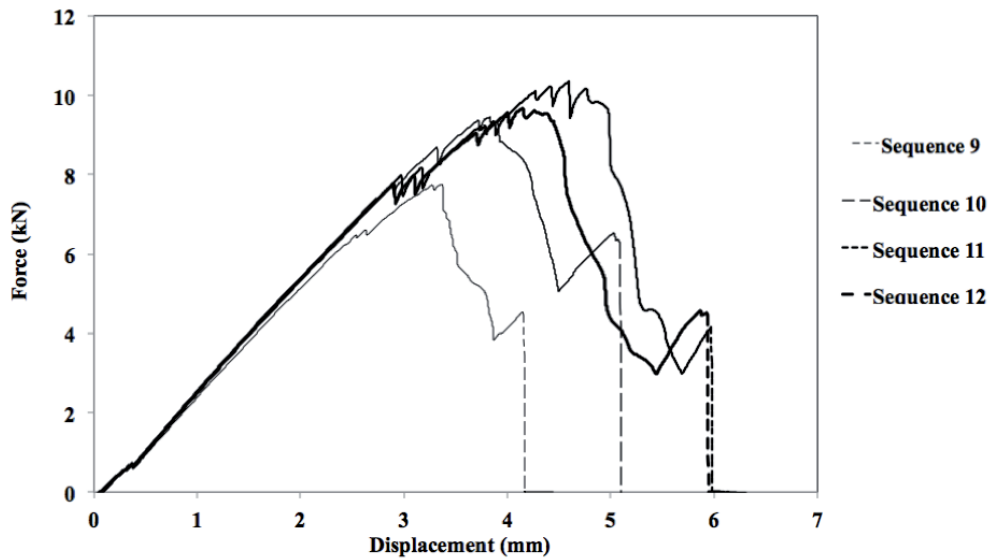
Fig. 4.19 Force-displacement curves obtained from CTS testing of different welds of 22MnB5 steel.

pulses, the mechanical performance is better than a single pulse weld. However, it is not as good as sequence 11.

4.2.2 Discussion

In this study, the welding sequences 9 to 12 as described in section 3.3 were applied. The cooling time between two current pulses was varied from 60 ms to 80 ms and 100 ms. The effect of the cool time on the microstructure and mechanical performance of the welds was studied.

The single pulse weld (sequence 9) shows partial interfacial failure (PIF) during CTS testing and the microstructure at the weld edge is dendritic. Microstructural changes in welds produced by double pulsing (sequence 10 and 11) lead to improved mechanical response and failure modes. In the case of double pulse welds subjected to a cooling time of 60 ms and 80 ms, the microstructure of the annealed zone is martensitic and consists of equi-axed grains. This is in agreement with the microstructures of the double pulse welded CR700Y980T-DH-GI steel discussed in section 4.1. In sequence 12, due to the longer cooling time (100 ms), during the second current pulse the microstructure remains dendritic and recrystallisation (nucleation and growth) of austenite does not occur and therefore, the mechanical performance is not as good as sequence 11.

As the microstructures of the primary and secondary weld nugget are martensitic, no considerable difference in the microhardness profiles of single pulse (sequence 9) and double pulse welded 22MnB5 steel (sequence 10-12) were found. A drop in the microhardness in the sub-critical HAZ (HAZ softening) is attributed to tempering of the martensite [17-19]. The microstructure of the base material is martensitic and during welding within the sub-critical HAZ, the martensite tempers and the microhardness drops.

The crack path during CTS testing of the welds in the presence of the equi-axed microstructure at the weld edge follows the grain boundaries and the failure mode is full plug failure. Conversely, the welds with the dendritic microstructure at the weld edge show partial plug failure.

4.3 Conclusions

The effects of a second current pulse during RSW on the microstructure and mechanical properties of two 3rd generation 1 GPa AHSS have been investigated. Based on the results obtained in this chapter, the following conclusions can be drawn:

1. The redistribution of the phosphorous as a detrimental alloying element and the improvement of the substructure (*i.e.* decreasing the block sizes) of the lath

martensite at the weld edge of a resistance spot weld with a double pulse welding scheme are the determining factors in the mechanical response of the AHSSs welds.

2. The elemental distribution of phosphorous at the primary weld nugget edge of the double pulse welds is more uniform than a single pulse weld. The distribution is improved when the area is subjected to a higher temperature, still below the melting temperature (*i.e.* a second current pulse of equal magnitude to the first).

3. The ellipticity of prior austenite grains at the primary weld nugget edge decreases during the second current pulse and the elongated grains become more equi-axed.

4. Double pulsing decreases the average prior austenite grain size and the block width and increases the geometrically necessary dislocation density of the lath martensite. The smallest mean prior austenite grain size and calculated block width and the highest geometrically necessary dislocation density at the edge of the primary weld nugget is obtained for double pulse welds subjected to a second current pulse lower than the first. In this case, the peak temperature at the primary weld nugget edge only allows limited austenite grain growth.

5. The mechanical properties of the welds have improved due to double pulsing and welds subjected to two equal current pulses show the highest maximum CTS and TSS and a favourable plug failure.

6. For the CR700Y980T-DH-GI steel examined in this chapter, the negative influence of phosphorous segregation to the grain boundaries on the mechanical performance of the welds is more pronounced than the positive influence expected due to grain size reduction.

References

[1]   S. Morito, H.Tanaka, R. Konishi, T. Furuhara, T. Maki, *The morphology and crystallography of lath martensite in Fe-C alloys*, Acta Mater. 51(6) (2003) 1789–1799.

[2]   S. Morito, X. Huang, T. Furuhara, T. Maki, N. Hansen, *The morphology and crystallography of lath martensite in alloy steels*, Acta Mater. 54(19) (2006) 5323–5331.

[3]   R.K. Ray, J.J. Jonas, *Transformation textures in steels*, Int. Mater. Rev. 35(1) (1990) 1-36.

[4]   J. Hidalgo, M.J. Santofimia, *Effect of prior austenite grain size refinement by thermal cycling on the microstructural features of as-quenched lath martensite*, Metall. Trans. A 47A (2016) 5288-5301.

[5]   G. Krauss, Steels: *Heat Treatment and Processing Principles*, Materials Park, Ohio, ASM International (1990).

[6]   T. Furuhara, K. Kikumoto, H. Saito, T. Sekine, T. Ogawa, S. Morito, T. Maki, *Phase transformation from fine-grained austenite*, ISIJ Int. 48(8) (2008) 1038-45.

[7]   T. Hanamura, S. Torizuka, S. Tamura, S. Enokida, H. Takechi, *Effect of austenite grain size on transformation behaviour, microstructure and mechanical properties of 0.1C–5Mn martensitic steel*, ISIJ Int. 53 (2013) 2218–25.

[8]   W. Hui, *Microstructure Refining and Strengthening of Martensitic Steel, incl. in Ultra-Fine Grained Steels*, Springer Berlin Heidel- berg (2009) 300-349.

[9]   A. Chabok, *Resistance spot welding of advanced high strength steels: Mechanical properties and failure mechanisms*, thesis, University of Groningen (2019).

[10]   C. Cayron, ARPGE, *A computer program to automatically reconstruct the parent grains from electron backscatter diffraction data*, J. Appl. Crystallogr. 40 (2007) 1183–1188.

[11]   M. Calcagnotto, D. Ponge, E. Demir, D. Raabe, *Orientation gradients and geometrically necessary dislocations in ultrafine grained dual-phase steels studied by 2D and 3D EBSD*, Mater. Sci. Eng. A. 527 (2010) 2738-46.

[12] L.P. Kubin, A. Mortensen, *Geometrically necessary dislocations and strain-gradient plasticity: a few critical issues*, Scripta Mater. 2003, vol. 48, pp. 119–25.

[13] S.C Kennett, G. Krauss, K.O. Findley, *Prior austenite grain size and tempering effects on the dislocation density of low-C Nb–Ti microalloyed lath martensite*, Scr. Mater. 107 (2015) 123- 126.

[14] S. Furusako, G. Murayama, H. Oikawa, T. Nose, F. Watanabe, H. Hamatani, Y. Takahashi, *Current Problems and the Answer Techniques in Welding Technique of Auto Bodies- First Part,* Nippon Steel technical report No. 103, Tokyo, Japan (2013) 69-75.

[15] B.C.D. Cooman, J.G. Speer, I. Yu Pyshminstev, N. Yoshinaga, *Materials design: the key to modern steel products: GRIPS media*, Harzburg, Germany (2007).

[16] J.I. Kim, J.H. Pak, K.S. Park, J.H. Jang, D.W Suh, H.K.D.H. Bhadeshia, *Segregation of phosphorus to ferrite grain boundaries during transformation in Fe–P alloy*, Int. J. Mater. Res. 105 (2014) 1166-1172.

[17] V.H. Baltazar-Hernandez, *A Study on Heat Affected Zone Softening in Resistance Spot Welded Dual Phase Steel by Nanoindentation*, J. Mater. Sci. 45 (2010) 1638– 1647.

[18] G. Krauss, *'Steels, heat treatment and processing principles'*, ASM International, Materials Park, OH (1990).

[19] R.A. Grange, C.R. Hribal, L.F. Porter, *Hardness of tempered martensite in carbon and low alloy steels*, Metall Mater Trans A. 8 (11) (1977) 1775-1785.

4

CHAPTER 5

Effect of a paint bake cycle on the microstructure-mechanical properties relationship of a resistance spot welded CR700Y980T-DH-GI steel[1]

The automotive paint bake (PB) thermal cycle is discussed in chapter 2 (section 2.6). It typically subjects the painted material to a temperature of about 180 °C for 20 min. The effects of the paint bake thermal cycle on the microstructural evolution and the mechanical properties of CR700Y980T-DH-GI resistance spot welds with single pulse and double pulse conditions are presented in this chapter. In order to also study the effect of the paint bake cycle on the fracture toughness behaviour, samples were prepared via Gleeble physical simulations to represent the coarse-grained HAZ microstructure of the welds, which were then subjected to the paint bake cycle.

5.1 Results

5.1.1 Microstructural analysis
Microstructural analysis was conducted on single pulse (sequence 5), single pulse-PB (paint bake cycle) (sequence 6), double pulse (sequence 7) and double pulse-PB (paint bake cycle) (sequence 8) welds, see Table 3.6. The locations of the samples taken for SEM and TEM studies within the weld nugget and the HAZ are schematically shown in Fig. 5.1. The SEM micrographs from zone 1 are shown in Fig. 5.2. The weld nugget microstructures of the single pulse and double pulse welds both show a martensitic microstructure (Fig. 5.2 a and b). Carbides were found in the weld microstructures of the low-temperature post-weld heat-treated samples (single pulse-PB and double pulse-PB) (Fig. 5.2 c-f); however, the SEM spatial resolution is not sufficient to confirm the type of carbides.

The SEM images of the as-welded samples (Fig. 5.2a and b) show martensitic microstructures with similar features for single and double pulse welding conditions. Further X-ray diffraction analysis was undertaken to better understand the microstructure of the double pulse welds. The X-ray diffractograms of the double pulse
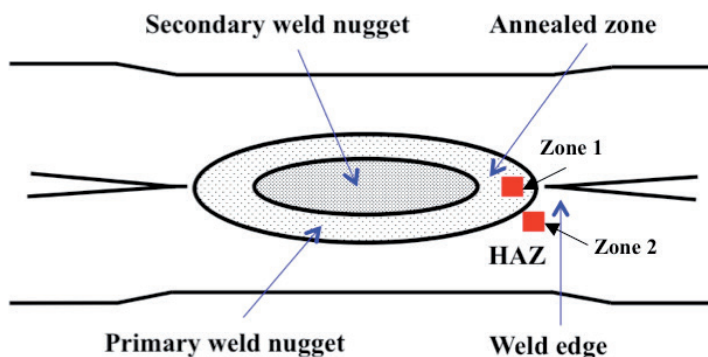
Fig. 5.1 Schematic representation of the locations where SEM and TEM samples were taken (colored squares). The dotted area is the primary weld nugget.
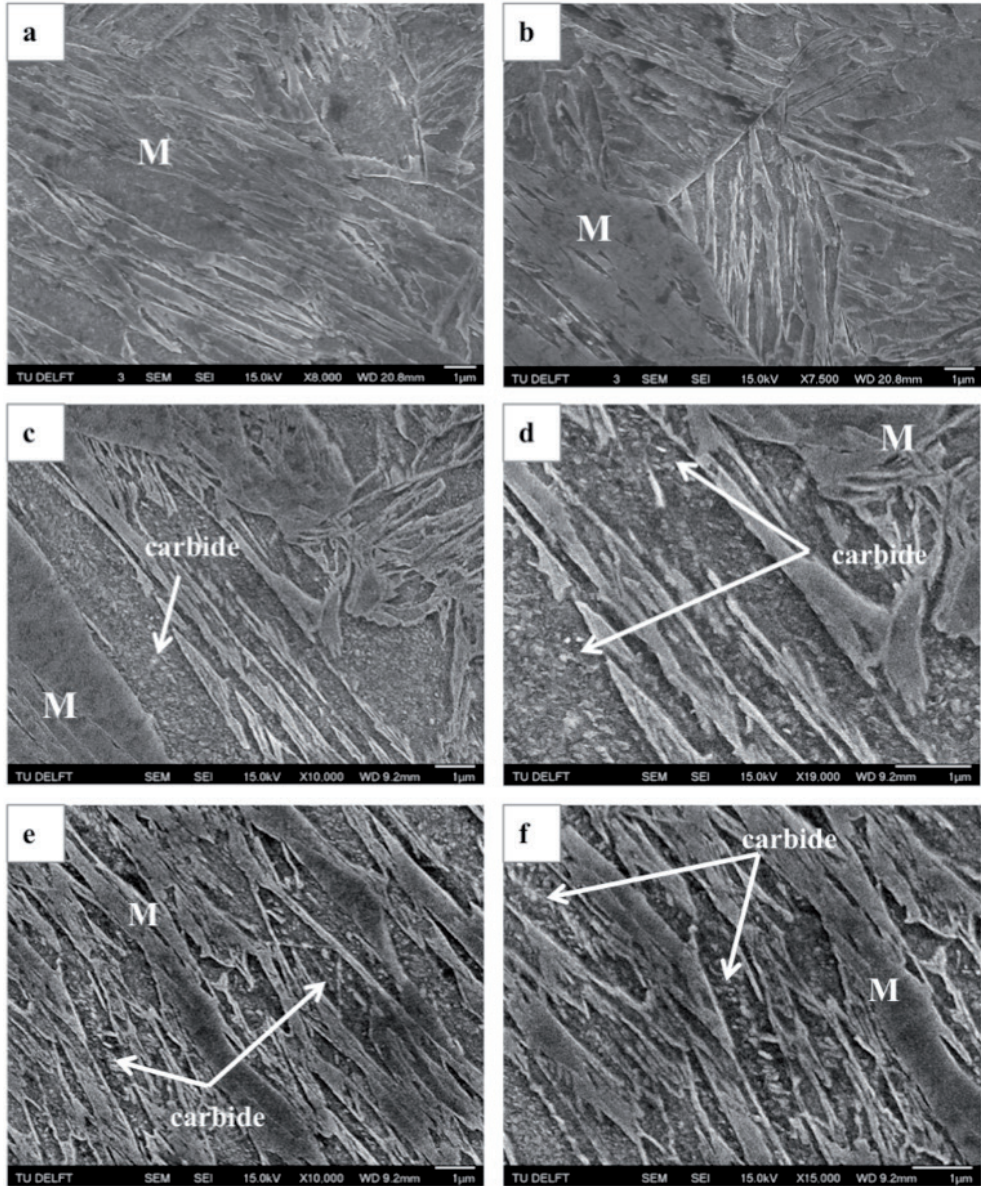
Fig. 5.2 SEM micrograph of the weld nugget (zone 1) of (a) single pulse, (b) double pulse, (c) single pulse-PB, (d) higher magnification of single pulse-PB, (e) double pulse-PB and (f) higher magnification of double pulse-PB.

and double pulse-PB weld taken from the weld nugget zone are shown in Fig. 5.3 a and b. These diffraction profiles show clear evidence of BCC martensite reflections for both samples. However, some traces of diffracting austenite planes (FCC) are detected in the diffraction pattern of the as-welded and heat-treated samples. The volume fraction
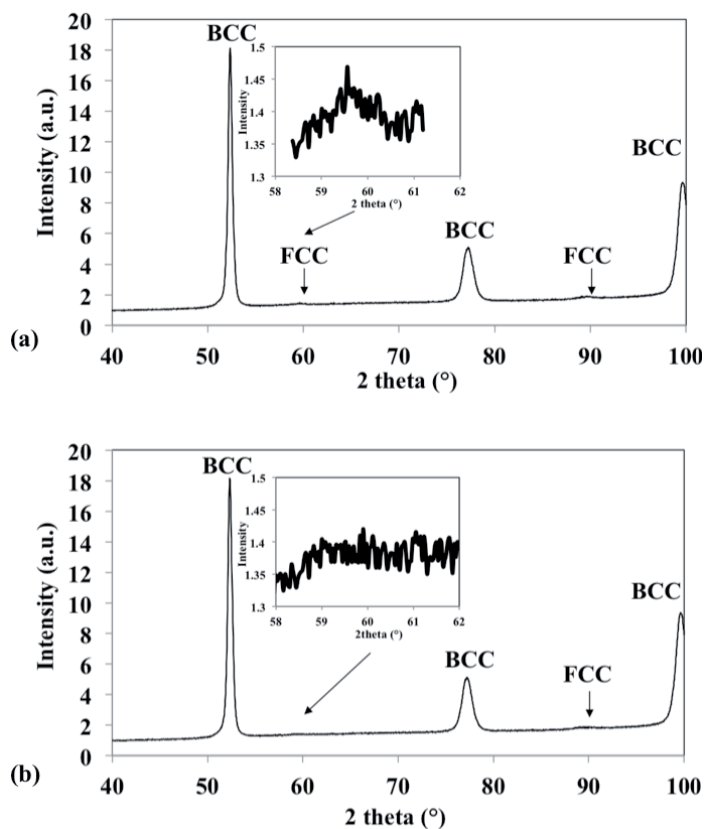
Fig. 5.3 X-ray diffraction profile of the (a) as-welded (double pulse weld) and (b) heat-treated (double pulse-PB) sample taken from the weld nugget zone (zone 1 in Fig. 5.1).

of this retained austenite is about 1 vol.% and 0.5 vol.% in the double pulse and the double pulse-PB weld, respectively. Diffraction peaks of carbides are expected at 2θ of 44°, 48.5° and 50.6° for ε-carbide and at 2θ of 44°, 50.2°, 51.2°, 52.2°, 52.8°, 53.8° and 57.7° for cementite. However, carbides were not detected from the X-ray diffraction profiles. The strongest carbide peaks are hidden under the strong ferrite peaks at 52.2° and for small particles (tens of nm), the diffraction peaks become boarder and disappear in the background, which makes it difficult to detect carbides with XRD.

Fig. 5.4 shows a bright field TEM image taken from the weld nugget zone (zone 1 in Fig. 5.1) of the as-welded double pulse weld and the corresponding selected area electron diffraction (SAED) pattern. The lath martensite features are clearly visible in Fig. 5.4 a and the indexed SAED pattern (Fig. 5.4 b) shows the Fe (α) reflections with zone axis of <0 -1 0>. No carbides were detected within the as-welded sample. The bright field TEM image taken from the HAZ of the double pulse weld (zone 2 in Fig. 5.1) and the corresponding SAED pattern are shown in Fig. 5.5. The detected reflections are Fe (α)
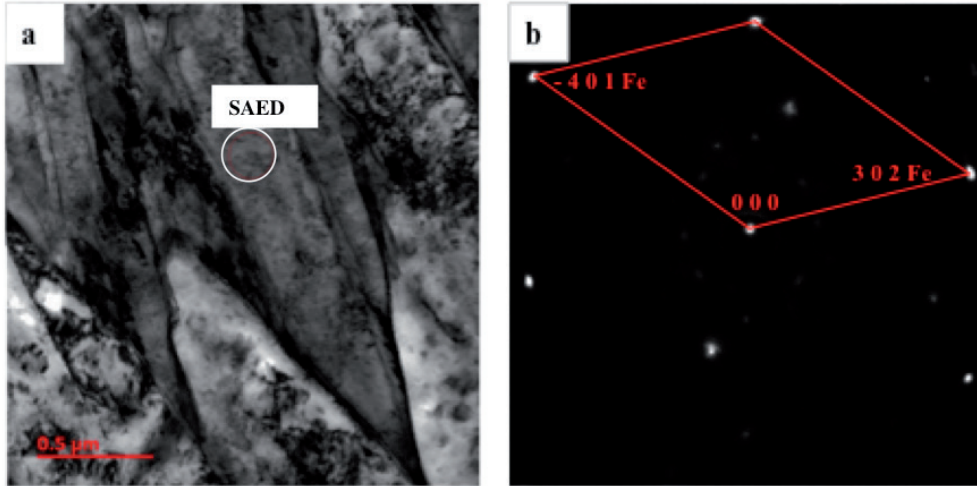
Fig. 5.4 (a) Bright field micrograph taken from the weld nugget of the double pulse weld (zone 1 in Fig. 5.1), (b) corresponding SAED pattern Fe (α) zone axis <0 -1 0>.
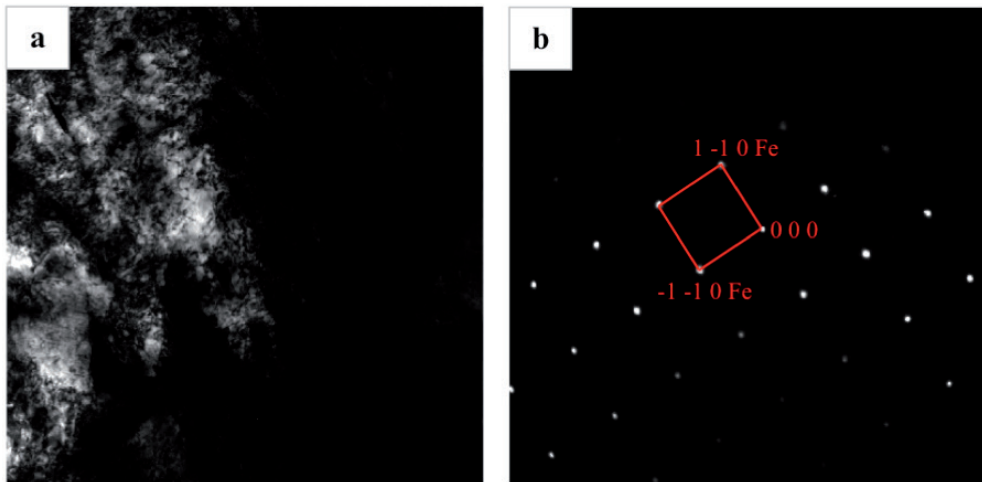
Fig. 5.5 (a) Bright field micrograph taken from the HAZ of the double pulse weld (zone 2 in Fig. 5.1), (b) corresponding SAED pattern Fe (α) zone axis <0 0 1>.

with zone axis of <0 0 1>. While again no carbide reflections were detected in the as-welded condition.

After a paint bake cycle was applied to both welding conditions, the microstructure was also investigated. Fig. 5.6 depicts the bright field image and the corresponding SAED pattern of the weld nugget of the double pulse-PB sample (zone 1 in Fig. 5.1). In this case, carbides are detected in the SAED pattern. The carbide type was determined by SAED analysis to be ε-carbide with zone axis of <0 1 1>.
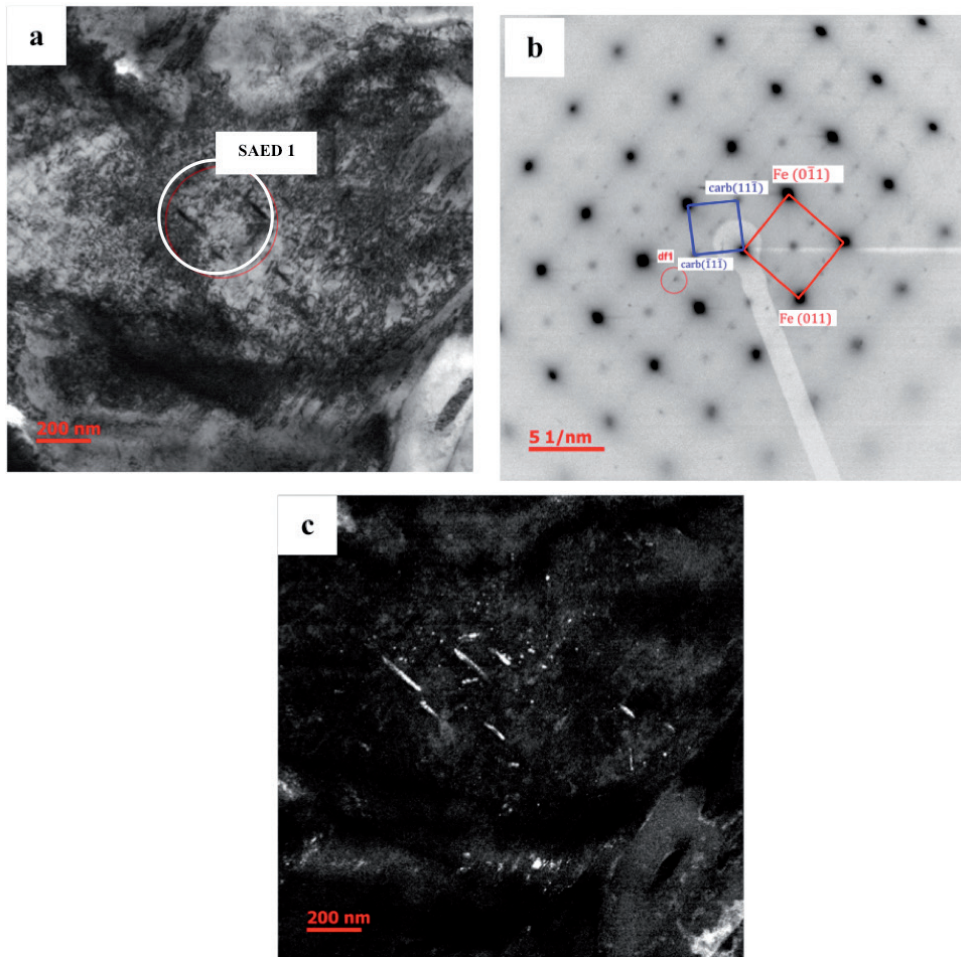
Fig. 5.6 (a) Bright field micrograph taken from the weld nugget of the double pulse-PB weld (zone 1 in Fig. 5.1), (b) corresponding indexed SAED pattern determined with CrysTbox software to be ε-carbide with zone axis <0 1 1> with excellent estimation rate and (c) dark field image of ε-carbide.

Fig. 5.7a shows a bright field TEM image taken from the HAZ of the heat-treated sample (double pulse-PB) (zone 2 in Fig. 5.1). The corresponding SAED pattern and the indexed pattern are shown in Fig. 5.7b and c, respectively. The ε-carbide with zone axis of <-1 -2 1> was detected after indexing the SAED pattern. Fig. 5.7d shows the dark field image of ε-carbide within the HAZ of the double pulse-PB sample.

5.1.2 Mechanical properties

The cross tension strength (CTS) test data for single pulse, single pulse-PB, double pulse and double pulse-PB welds is shown in Table 5.1. The representative load-displacement curves of the welds are presented in Fig. 5.8a. It should be mentioned that the weld nugget size is similar and about 6.3±0.2 mm for these welds (n=3). In chapter 4, it has
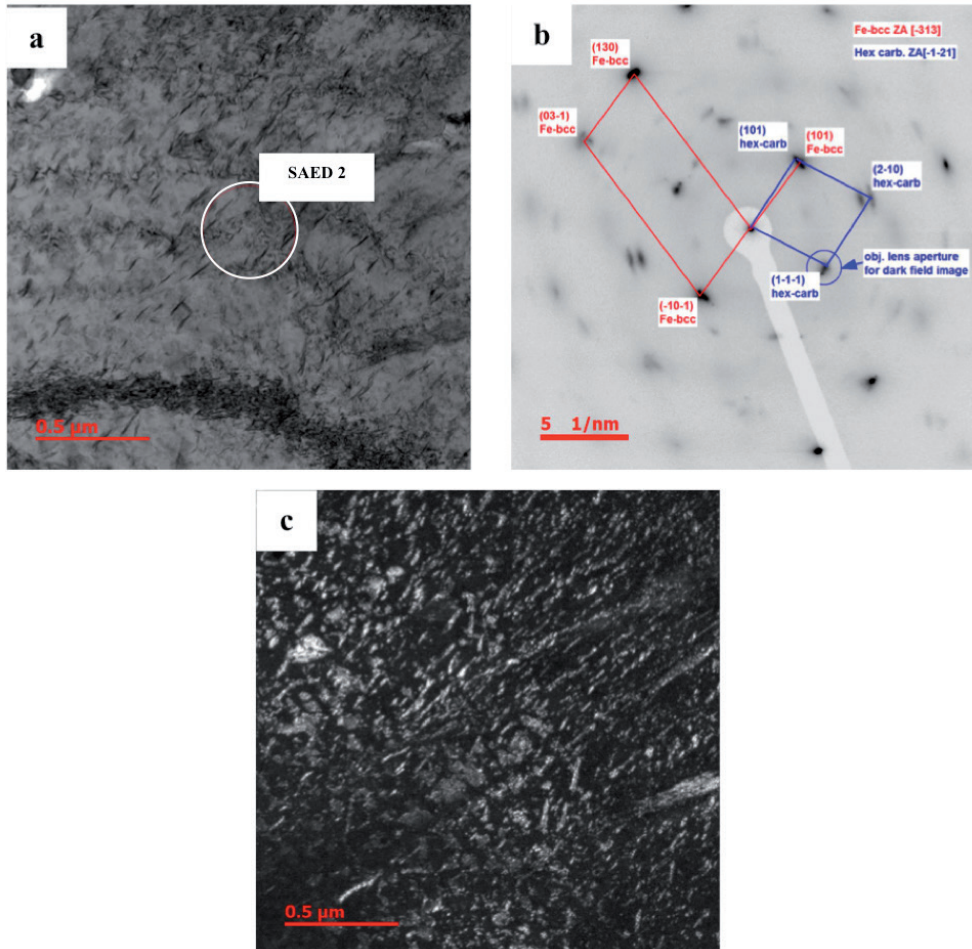
Fig. 5.7 (a) Bright field micrograph taken from the HAZ of the double pulse-PB sample (zone 2 in Fig. 5.1) (b) corresponding indexed SAED pattern determined with CrysTbox software to be ε-carbide with zone axis <-1 -2 1> with excellent estimation rate and (c) dark field image of ε-carbide.

been mentioned that the double pulse weld shows higher cross tension (CT) strength and displacement in comparison with the single pulse weld, although the weld nugget size of both welds is the same. Fig. 5.8a and Table 5.1 indicate that the paint bake heat-treated samples (single pulse-PB and double pulse-PB) show significantly higher CT strength and displacement than the as-welded samples (single pulse and double pulse weld, respectively). The highest CTS performance is achieved by the double pulse-PB sample with an average CT strength level of 8.4 ± 1.2 kN and an average displacement at maximum force of 12.1 ± 1.0 mm (number of samples per set is 3). The energy absorption capability (absorbed energy to maximum load) for the welds is depicted in Fig. 5.8b. The highest energy absorption capability is obtained for the double pulse-PB sample. Representative failure areas of different welds are given in Fig. 5.9. Single pulse and

Table 5.1 Cross tension strength (CTS) test data (I=6.6 kA, weld diameter ≈ 6.3±0.2 mm)..

Weld	Average max. force (kN) CTS strength (n= 3)	Average displacement at max. force (mm) (n= 3)	Failure mode
Single pulse	3.8 ± 0.3	6.0 ± 0.5	Partial Interfacial Failure
Single pulse-PB	5.2 ± 0.3	6.1 ± 0.5	Partial Interfacial Failure
Double pulse	5.7 ± 0.1	8.0 ± 0.2	Plug Failure
Double pulse-PB	8.4 ± 1.2	12.1 ± 1.0	Plug Failure
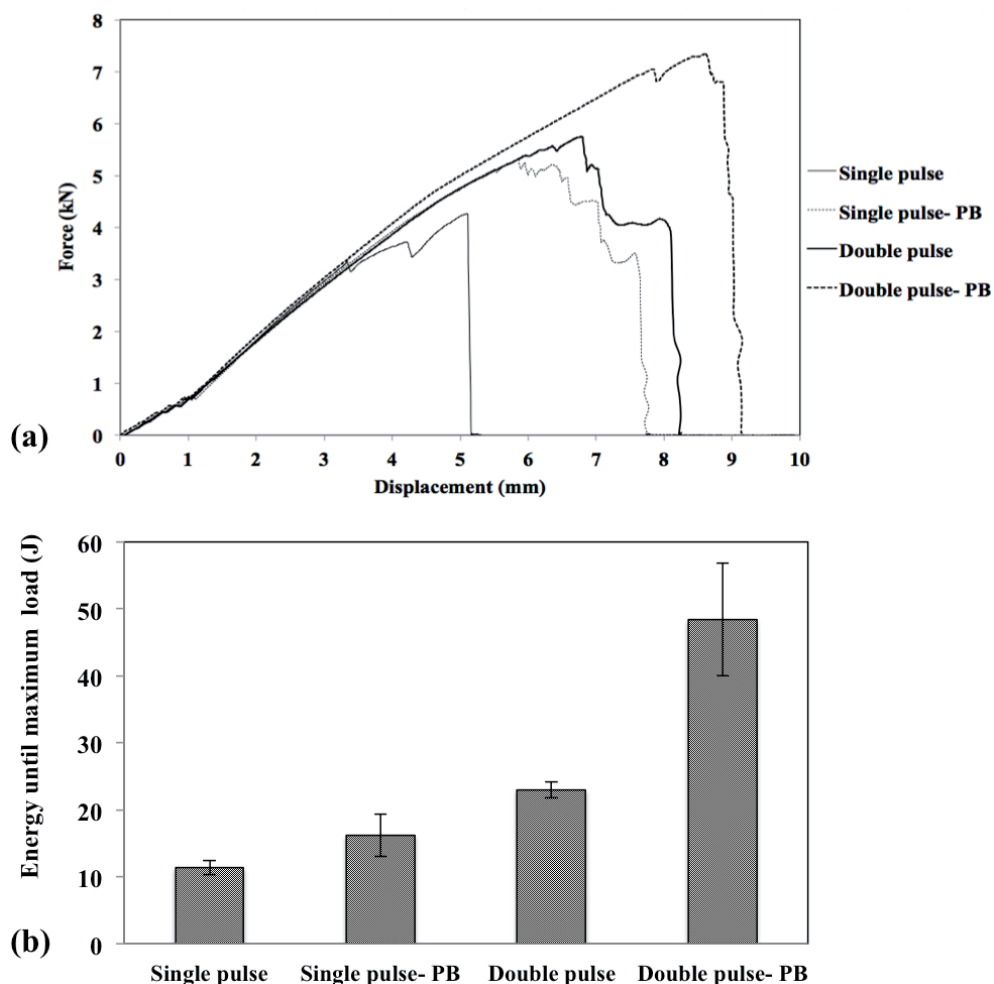
Fig. 5.8 (a) Schematic representation of force-displacement curves, (b) energy absorption to maximum load in single pulse, double pulse, single pulse-PB and double pulse-PB welds in cross tension strength tests (n= 3).
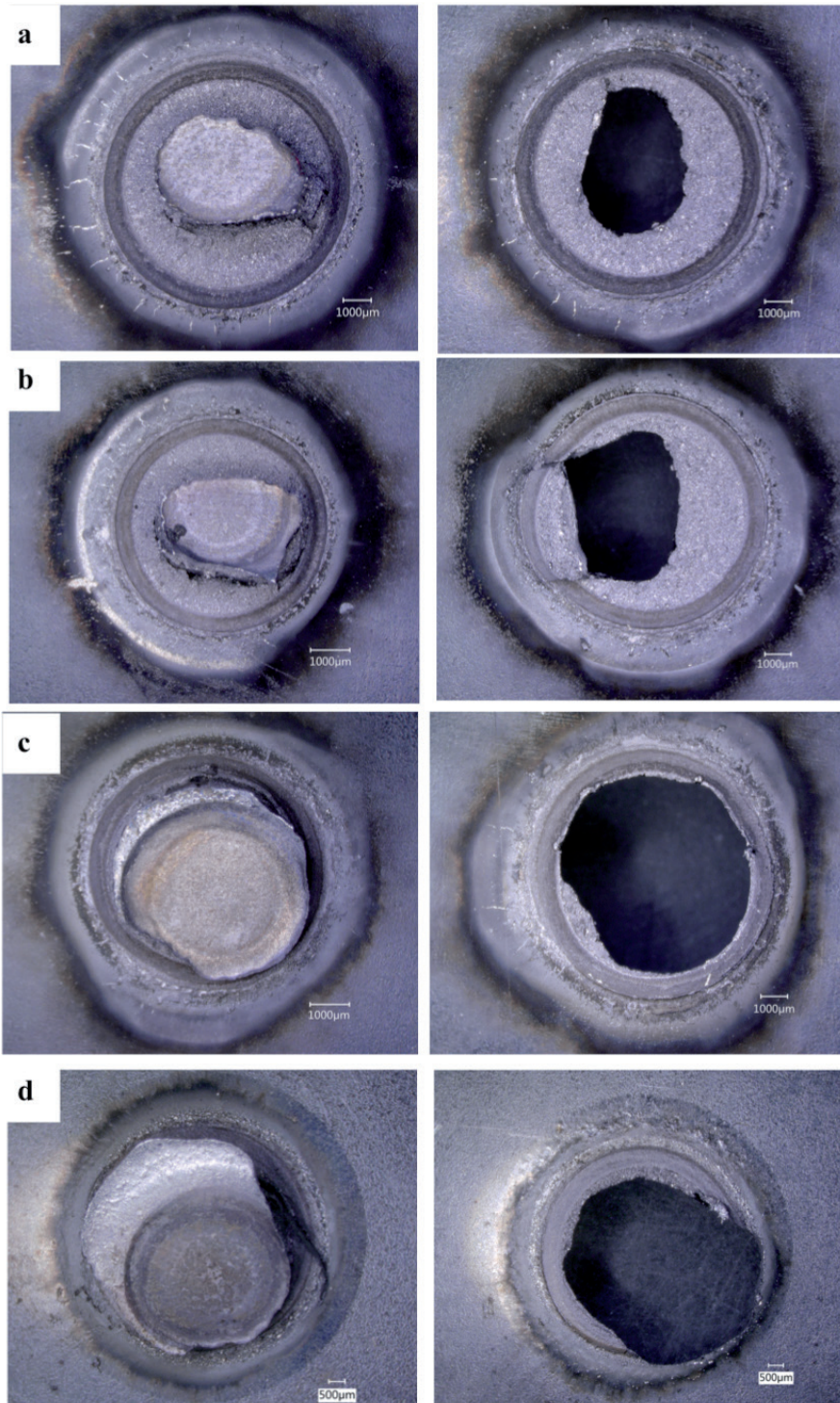
Fig. 5.9 Representative failure modes of (a) single pulse weld, (b) single pulse-PB, (c) double pulse weld and (d) double pulse-PB for cross tension strength tests.
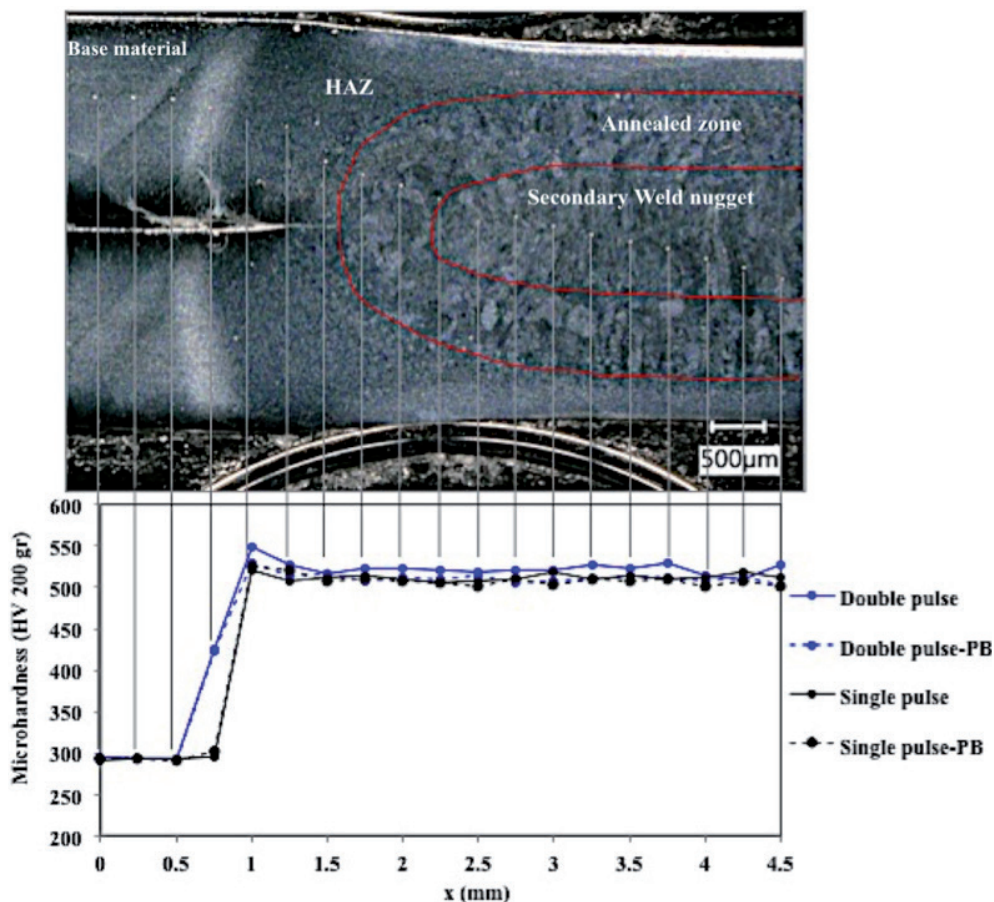
Fig. 5.10 Microhardness profile of the welds studied. The indents are shown on a cross section of a double pulse weld.

single pulse-PB welds show partial plug failure (Fig. 5.9a and b). Double pulse and double pulse-PB welds show the favorable full plug failure mode (Fig. 5.9c and d). Note that the paint bake thermal cycle after welding in the present work does not change the failure mode of the CTS samples. The microhardness profile of the welds studied is presented in Fig. 5.10. The average weld nugget microhardness of single pulse and double pulse weld is 512 HV_{200g} and 520 HV_{200g}, respectively. The weld nugget microhardness of the single pulse-PB and double pulse-PB welds is 505 HV_{200g} and 510 HV_{200g}, respectively. Although, a reduction of about 10 HV_{200g} is observed in hardness after heat treatment, this small drop by itself does not explain the large difference in CT strength behaviour.

The fractured surfaces of the welds are depicted in Fig. 5.11. The single pulse weld and single pulse-PB weld with partial plug failure mode under peel loading (CTS) show a mixed brittle and ductile fracture (Fig. 5.11a and 5.11c). However, the double pulse
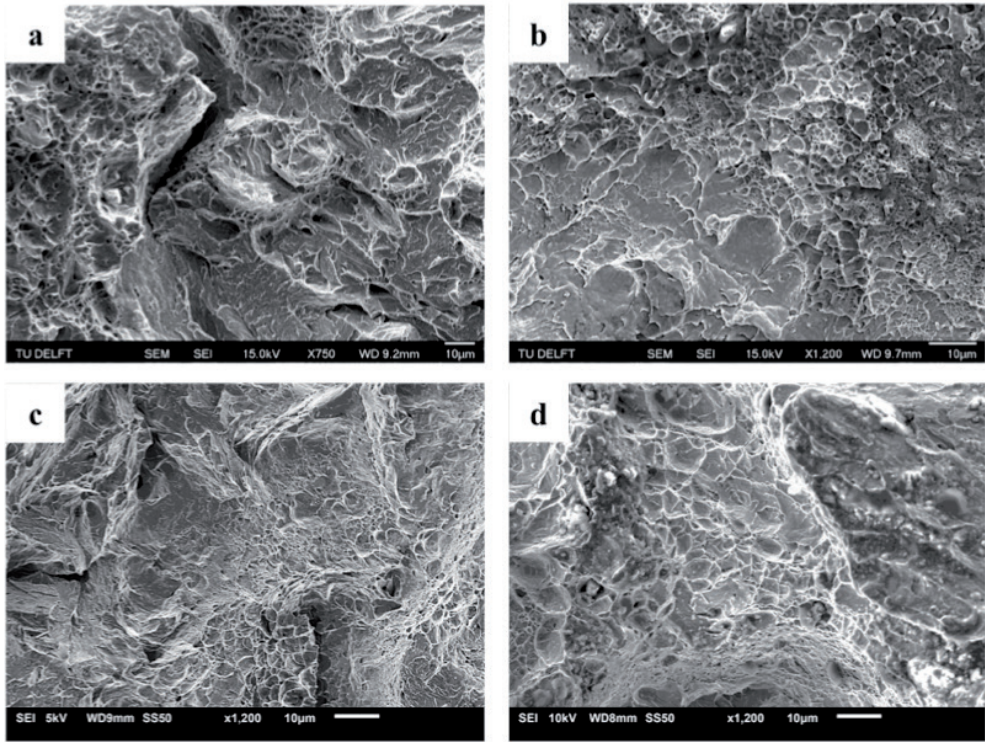
Fig. 5.11 Fractured surfaces of the CTS samples (a) single pulse weld indicating mixed brittle-ductile fracture, (b) double pulse weld indicating ductile fracture, (c) single pulse-PB indicating mixed brittle-ductile fracture and (d) double pulse-PB indicating ductile fracture.

weld and double pulse-PB weld with full plug failure in CTS test show dimples that are representative for a ductile failure (Fig. 5.11b and 5.11d). The results of mechanical tests confirm that the paint bake thermal cycle can significantly enhance the mechanical performance of the AHSS.

5.1.3 Fracture toughness measurement of a martensitic thin sheet of CR700Y980T-DH-GI with and without a baking cycle

In this section, the results of the fracture toughness measurement of a thin sheet steel are presented. As described in chapter 3, the microstructure of martensite and tempered martensite were simulated by means of a Gleeble 1700 thermo-mechanical simulator. The thermal cycle applied is presented in Fig. 3.26 section 3.4.4. The simulated martensite microstructure is representative for the course grained HAZ of the as-welded samples, whereas the simulated tempered martensite microstructure is representative for the course grained HAZ after application of the paint baking thermal cycle.

The load-displacement curve obtained from the fracture toughness test for the fully martensitic sample (pre-paint bake cycle application), *i.e.* the course grained HAZ, is
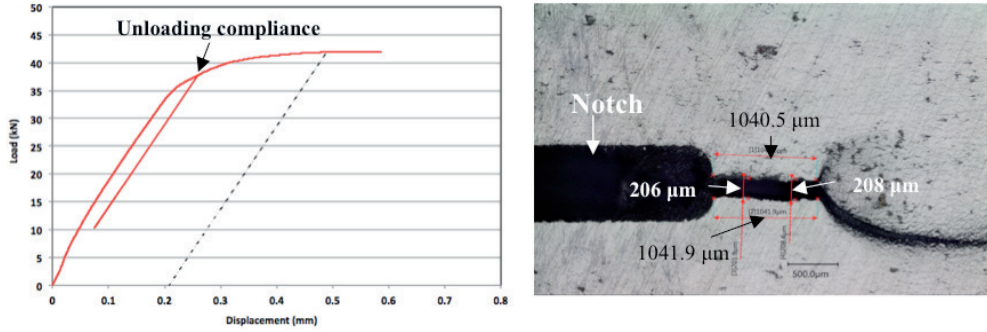
Fig. 5.12 (a) Load-displacement curve representing the crack mouth opening displacement of 211 µm and (b) optical micrograph of the crack after unloading, showing a crack opening displacement of 208 µm, in a fully martensitic sample (pre-paint bake cycle application).
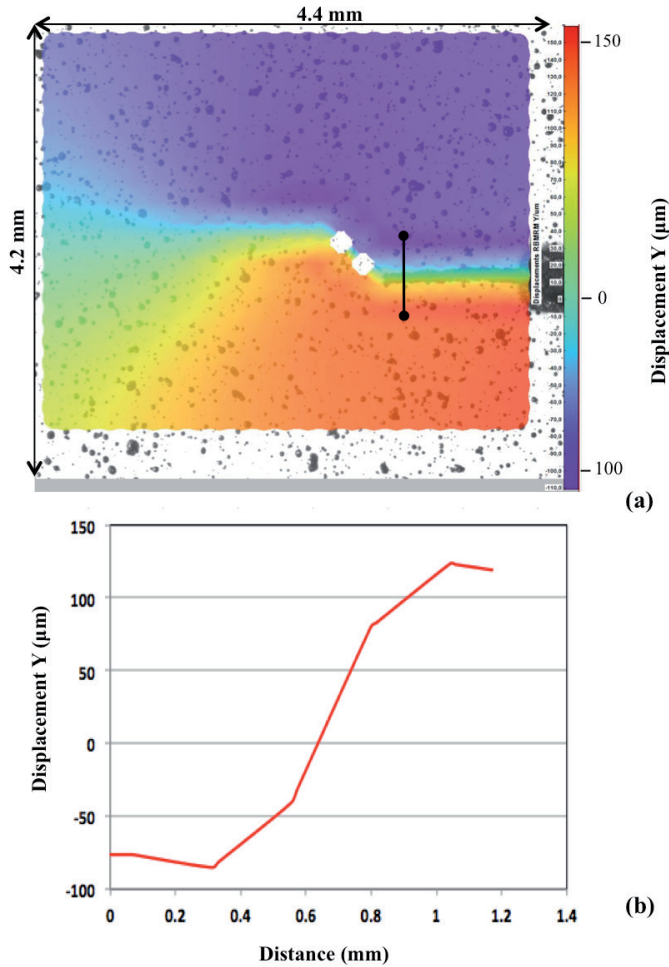
Fig. 5.13 DIC results for the fully martensitic sample (pre-paint bake cycle application) (a) the image overlaying the speckle pattern shows the displacement distribution measured, (b) displacement of the crack in the y direction through the line shown in (a).
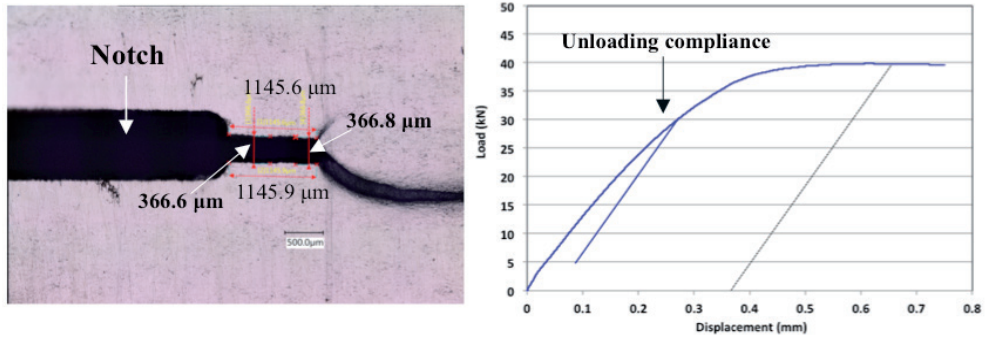
Fig. 5.14 (a) Optical micrograph of crack after unloading, showing crack opening displacement of 366 μm and (b) obtained load-displacement curve representing the crack mouth opening displacement of 371 μm in tempered martensite sample (after paint bake cycle application).
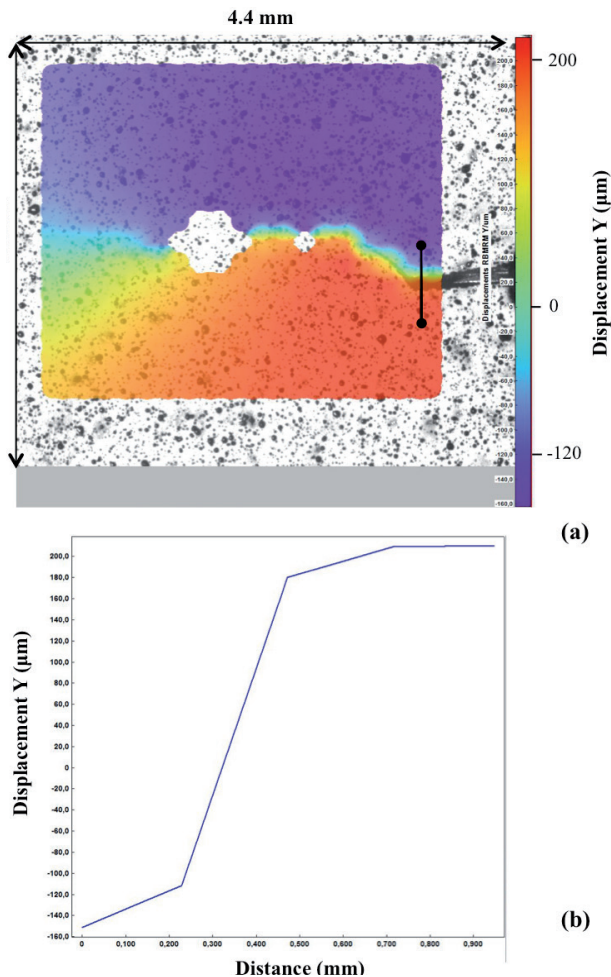
Fig. 5.15 DIC results for the tempered martensite sample (after paint bake cycle application) (a) the image overlaying the speckle pattern shows the displacement distribution measured, (b) displacement of the crack in the y direction through the line shown in (a).

Table 5.2 Comparison of fracture toughness results obtained from different methods.

Sample	Extensometer CMOD (mm)	Optical microscopy measurement crack opening displacement (mm)	DIC crack opening displacement measurement (mm)
Martensite (Pre-paint bake cycle application)	0.211	0.208	0.21
Tempered Martensite (After paint bake cycle application)	0.371	0.366	0.37

shown in Fig. 5.12 a. The measured crack mouth opening displacement is 211 μm. The optical micrograph of the crack after unloading this sample is shown in Fig. 5.12 b. As can be seen in this figure, the crack mouth and tip opening displacement are similar and the crack top and bottom surfaces have propagated parallel. Therefore, the crack mouth opening displacement can be considered as crack tip opening displacement (CTOD) [1]. The CTOD according to Fig. 5.12 b is 208 μm. During the fracture toughness tests, the digital image correlation (DIC) technique was applied to obtain displacements. The result is presented in Fig. 5.13, showing a crack opening displacement of 210 μm.

The load-displacement curve and an optical micrograph of the crack after unloading for the tempered martensite sample (after paint bake cycle application) are shown in Fig. 5.14. The displacement obtained from the DIC measurement for this sample is presented in Fig. 5.15.

An overview of the results from different CTOD determination techniques is given in Table 5.2, indicating that the CTOD has increased after applying a baking cycle. Furthermore, the techniques employed indicate a similar trend, *i.e.* paint baking increases the toughness represented by the CTOD value.

5.2 Discussion

As shown in chapter 4, the mechanical properties of resistance spot welded 3rd generation AHSSs can be significantly improved by applying a double pulse welding scheme. Improvement in mechanical performance of double pulse welds has been reported to be related to the redistribution of alloying elements such as phosphorous and the modification of the lath martensite sub-structure at the weld nugget edge during the second current pulse (chapter 4). In this chapter, the description of the microstructural evolution is extended with the effect of a second heat treatment, *i.e.* a paint bake thermal cycle. The mechanical performance of the welds has been improved even further after the application of the paint bake thermal cycle [2].

The increase in CT strength of heat-treated single pulse and double pulse welds compared to none-heat treated welds is 37% and 47%, respectively. Energy absorption, which is representative of the weld crashworthiness, has also increased after the application of the heat treatment. The double pulse-PB weld has the highest absorbed energy level to maximum load (about 48.5 J), which is in the order of a standard (1st generation) AHSS. Although a constant hardness reduction of about 7 HV_{200g} is shown in heat-treated welds, this hardness drop is believed to be too small to explain the large increase in CT strength. Smith *et al.* [3] have also reported similar effects of a paint baking cycle on the hardness levels of AHSSs welds.

The microstructural analysis of the as-welded samples either in the weld nugget or the HAZ shows a lath martensite microstructure (Fig. 5.4 and 5.5). The high cooling rates of RSW and the relatively high amount of alloying elements in AHSSs compared with conventional steels result in an almost fully martensitic weld nugget and a coarse and fine grained HAZ in these welds.

A possible factor contributing to the increased weld CT strength and higher energy absorption after a paint bake thermal cycle is tempering of martensite, *i.e.* carbide formation and thereby increasing the martensite fracture toughness.

The baking thermal cycle (at 453 K (180 ° C) for 20 min) is similar to low temperature tempering of the steels. The effects of tempering on the martensite microstructure depending on the tempering temperature have been reported. During tempering at temperatures below 373 K (100 °C), the carbon atoms segregate to the interstitial sites and dislocations and form carbon clusters [4, 5]. At temperatures between 353 K (80 °C) and 473 K (200 °C), precipitation of carbides occurs [4]. TEM analysis of the heat-treated welds at the weld nugget and the HAZ reveal the presence of carbide precipitates (Fig. 5.6, 5.7).

The chemical composition of steel together with the thermal cycle determines the microstructure and mechanical properties after tempering. Grange *et al.* [6] has reported that the hardness reduction of martensite in an iron-0.2 wt.% carbon alloy after 473 K (200 °C) tempering for 1 h is about 50 HV. However, adding 1 wt.% Si to the system could increase the hardness of the tempered martensite by about 40 HV [6, 7]. Also, Si inhibits the conversion of ε-carbide to cementite and increases the stability range of ε-carbide. Alloying elements such as Mn, P and Mo seem to have no effect on the hardness of martensite after tempering [6]. The steel considered in this study consists of relatively higher C and Si levels compared to conventional AHSS. These increased levels of C and Si are typical alloying strategies to obtain the desired strength-ductility properties. In this steel, due to its chemical composition the paint bake thermal cycle (at 453 K (180 °C) for 20 min) did not lead to severe hardness reduction (Table 3.1 chapter 3). As reported in the literature and also confirmed in this work, the hardness reduction is about 7 HV.

It is widely reported that the weld nugget and HAZ hardness reduction leads to an increase in CT strength and displacement of the spot welds [8]. Lalam [9] has reported that paint baking improves the CT strength by about 1.78 kN and reduces the CGHAZ hardness by about 60 Vickers for a weld that has been welded with a current of 9.7 kA. However, in the current results the hardness reduction is low and it is very unlikely that the small decrease in the microhardness level leads to the significant increase in CT strength. In the single pulse welds, the effect of segregation during solidification on the mechanical behaviour is most dominant. This leads to partial interfacial failure, *i.e.* failure of the weld metal. The paint bake cycle results in the formation of ε-carbides in the HAZ and weld nugget and possibly a decrease of dislocation density. This increases the strength and displacement of the weld in CTS testing, but does not change the mode of failure. If a double pulse welding sequence is applied, the segregation is decreased, grain morphology and martensite substructure are modified and a favorable failure mode results with the joint failing in the HAZ. Again the paint bake cycle, promotes precipitation taking place in the weld nugget and HAZ microstructure. This results in a general improvement of mechanical properties. The main factor, which decides whether a favorable fracture mode is obtained is thus related to elemental segregation. The paint bake cycle has a general strengthening effect. It has also been reported that the presence of about 1 vol.% ε-carbide has a contribution of about 130 MPa for the yield strength of a quenching and partitioning steel [10].

Other possible factors contributing to the increased weld CT strength and higher energy absorption after a paint bake thermal cycle are changes in retained austenite (RA), hydrogen content of the weld and a change in residual stresses within the weld nugget and the HAZ.

The transformation of retained austenite to bainite can occur during the heat treatment [4]. As shown in Fig. 5.3, the retained austenite is calculated to be about 1 vol.% in the as-welded sample and about 0.5 vol.% in the heat-treated sample. However, the decomposition of retained austenite is reported only for heat treatments at temperatures higher than 473 K (200 °C) [4]. The small change from 1% to 0.5% in RA volume percent can be neglected as a contributing factor in the present work as the 0.5% change in RA volume percent lies within the range of the experimental error for RA measurement with XRD.

The hydrogen content of the welds was measured, however due to the difficulties in interpreting the results regarding the effect of possible contaminations *i.e.* oil on the surface of the sheet materials prior to welding, no concrete conclusions can be drawn. Therefore, the effect of changes in hydrogen content of the weld is not considered further.

Crack initiation during loading is indicated by the pop-ins in the load-displacement curves of the CTS test (Fig. 5.8a). The crack initiation is delayed in heat-treated samples. Delayed crack initiation in heat-treated welds is due to an increase in fracture toughness

of the martensite. This is partly supported by the fact that the failure modes of the welds do not change, while the CT strength increases.

In summary, a typical paint bake cycle increases the CT strength and energy absorption capability of both single and double pulse resistance spot welded samples as a result of the precipitation of ε-carbides within the weld nugget and the HAZ.

5.3 Conclusions

Based on the microstructural and mechanical characterisation of the as-welded samples and those subjected to a paint bake cycle after welding, the following conclusion can be drawn:

1. Precipitation of ε-carbides and increase in fracture toughness of the martensite after the paint baking cycle contribute to the improved CTS properties of the welds.
2. Double pulse welding, followed by a paint baking cycle provides AHSS resistance spot welds with good mechanical performance.
3. The crack tip opening displacement (CTOD) of martensite has increased after a baking cycle and the results obtained from different methods are consistent and comparable.

References

[1] Th. Opraus, *Determining the suitability and application of CNT test specimens for failure assessment of welded high strength steels*, Master thesis, Delft University of Technology (2017).

[2] E.M. Van der Aa, D.N. Hanlon, T. van der Veldt, *Resistance spot weldability of 3rd generation advanced high strength steels for automotive applications*, Steels in Cars and Trucks, Noordwijkerhout, The Netherlands, 19-21 June 2017.

[3] S. Smith, T. Okada, N.J. den Uijl, T. van der Veldt, M. Uchihara, K. Fukui, *Influence of the Paint Baking Cycle on the Mechanical Properties of AHSS Welded Structures in Automotive Assemblies*, International Automotive Body Congress (IABC), At Vaals, The Netherlands, June 2009.

[4] G.R. Speich, W.C. Leslie, *Temepring of steels*, Met. Trans. A. 3(5) (1972) 1043-1054.

[5] G. Kraus, *Tempering and structural change in ferrous martensitic structures*, Phase Transformations in Ferrous Alloys Proceedings, Philadelphia, Pa, The Metallurgical Soc. of AIME, Ferrous Metallurgy Committee, (1983) 101–123.

[6] R.A. Grange, C.R. Hribal, L.F. Porter, *Hardness of tempered martensite in carbon and low alloy steels*, Metall. Trans. A. 8A (1977) 1775-1785.

[7] G. Krauss, *Deformation and fracture in martensitic carbon steels tempered at low temperatures*, Metall. Mater. Trans. A. 32A (2001) 861-877.

[8] M. Pouranvari, S.P.H. Marashi, *Critical review of automotive steels spot welding*: *process, structure and properties*, Sci. Technol. Weld. Join. 18(5) (2013) 361–403.

[9] S.H. Lalam: *Weldability of AHSS*. Proc. Great Designs in Steels Seminar, Livonia, MI, USA, March 2005, AISI, http://www.autosteel.org/Great%20 Designs%20in%20Steel.aspx.

[10] F. HajyAkbary, J. Sietsma, G. Miyamoto, N. Kamikawa, R.H. Petrov, T. Furuhara, M.J. Santofimia, *Analysis of the mechanical behavior of a 0.3C-1.6Si-3.5Mn (wt%) quenching and partitioning steel*, Mater. Sci. Eng. A 677 (2016) 505-514.

CHAPTER 6

Investigation of residual stress distribution in a resistance spot welded advanced high strength steel[1]

In a typical resistance spot welding thermal cycle, the mechanical and thermal constraints due to the electrode force in combination with a high local heating and cooling rate introduce residual stresses within the weld, which influence the mechanical performance. Various studies have been carried out to simulate the state of residual stress in spot-welded joints [1-7]. Khanna *et al.* [1] presented a review of the numerical models used to predict the spatial and temporal distribution of residual stresses in spot welded steel sheets and the effect of residual stress on the fatigue strength of a spot weld. It has been reported that the radial residual stress is tensile in nature in the weld nugget. A high fatigue load results in significant residual stress redistribution during cycling and the tensile residual stress at the weld centre is reduced [1]. There is limited literature on residual stress measurements of resistance spot welds. Florea *et al.* [7] reported results on residual stresses, obtained by neutron diffraction in spot welded aluminum alloys. Khanna *et al.* [8] have determined the residual stress in mild steel spot welds using the Moiré interferometric method with hole drilling. The yield strength of the mild steel (base material) is about 300 MPa. The in-plane residual stress in the weld centre was found to be in the range of 250-300 MPa. Low cycle fatigue loading of the spot weld caused the residual stress to drop in the weld centre by about 30% Chabok [9] reported the residual stress measurements in front of the pre-crack for single and double pulse welds of DP1000 steel. Residual stress measurement showed that the compressive residual stress perpendicular to the plane of the pre-crack decreases significantly for the double pulse welded sample [9].

Exact stress levels and distributions in the spot welded area for the AHSSs are not available, nor is the effectiveness of multiple thermal cycling, by double pulsed welding schemes, on stress redistribution or stress mitigation. High-energy synchrotron X-ray diffraction allows this data to be obtained [10, 11], which is required to come to a better understanding of the mechanical performance and failure mechanisms of resistance spot welds. High-energy synchrotron X-ray diffraction is a non-destructive technique to measure the residual strain. The high energy X-ray penetrates deeper in the material compared to laboratory XRD and allows depths resolved strain measurements within the materials. The strain measurements were carried out on the high-resolution powder diffraction beamline ID22 at the European Synchrotron Research Facility (ESRF) in Grenoble, France (see section 3.4.2). A monochromatic 70 keV X-ray beam, providing a wavelength of 0.17709589 Å with a focal spot size of 150×50 μm^2 at the sample position, was used to record the diffraction patterns of ferrite (200) planes in transmission mode. Strain scanning with a gauge length of about 600 μm was performed in a radial direction with the step size of 300 μm at two different depth locations, one at the weld centre depth location and the other at a depth of 0.65 mm from the plate surface (half of one plate thickness). The measurements were carried out in two in-plane directions at each point

with a 90° rotation (two in-plane stress components). The strain measurement at the centre line was stopped where the weld edge was reached. Furthermore, the novel FIB ring-core milling technique was used to measure the micro-residual strain at the weld edge of a resistance spot weld (see section 3.4.3). This technique and the high-energy synchrotron X-ray diffraction technique allow a comparison to be made of the residual strains of a resistance spot weld at micro-scale, in the order of 5 μm, and at macro scale, with a gauge volume of about 650 μm.

A 3D finite-element based electrical-thermal-metallurgical-mechanical model was developed in the Simufact platform to compare with the residual stresses obtained from experimental synchrotron X-ray diffraction measurements (see section 3.5.2). In this chapter, measured residual stresses as well as the constructed finite element model are presented and discussed.

6.1 Results

6.1.1 Residual stress measurement of single and double pulse welds

A schematic representation of a top view and a cross section of a single pulse spot weld (welding sequence 1, as described in section 3.3) are shown in Fig. 6.1 a and b, respectively. The measured z-component (parallel to the sheet surfaces) of residual stress (σ_z) as a function of the distance from the weld centre to the base material along the defined line (blue line in Fig. 6.1 a and b) is presented in Fig. 6.1 c. The results show that the residual stress within the weld nugget and HAZ is tensile. There is a decrease in residual stress level from the HAZ towards the base material. The base material shows compressive residual stresses near the weld. The z-component residual stress as a function of the distance from the weld centre to the weld edge along the weld centre line (red line in Fig. 6.2 a) is presented in Fig. 6.2 b. The residual stress within the weld nugget is also tensile. The stress levels are comparable with the stresses measured along the blue line.

In order to understand the effect of the welding current amplitude on the residual stress of the single pulse resistance spot welds, residual stress measurements were performed on the single pulse spot welds created with the minimum current (I_{min}), a medium current ($I_{6.2\,kA}$) and the maximum current (I_{max}). The average residual stress obtained from the (200) planes at the weld edge for different welds are shown in Fig. 6.3. A slight increase is observed in residual stress values for welds produced with higher welding currents.

The residual stress distribution of a double pulse weld (welding sequence 3 ($I_1=I_2=6.2$ kA, as described in section 3.3) from weld centre to base material along the line defined at Fig. 6.1 a and b is shown in Fig. 6.4. These results also show that the residual stress within the weld nugget and HAZ in a double pulse weld is tensile, while
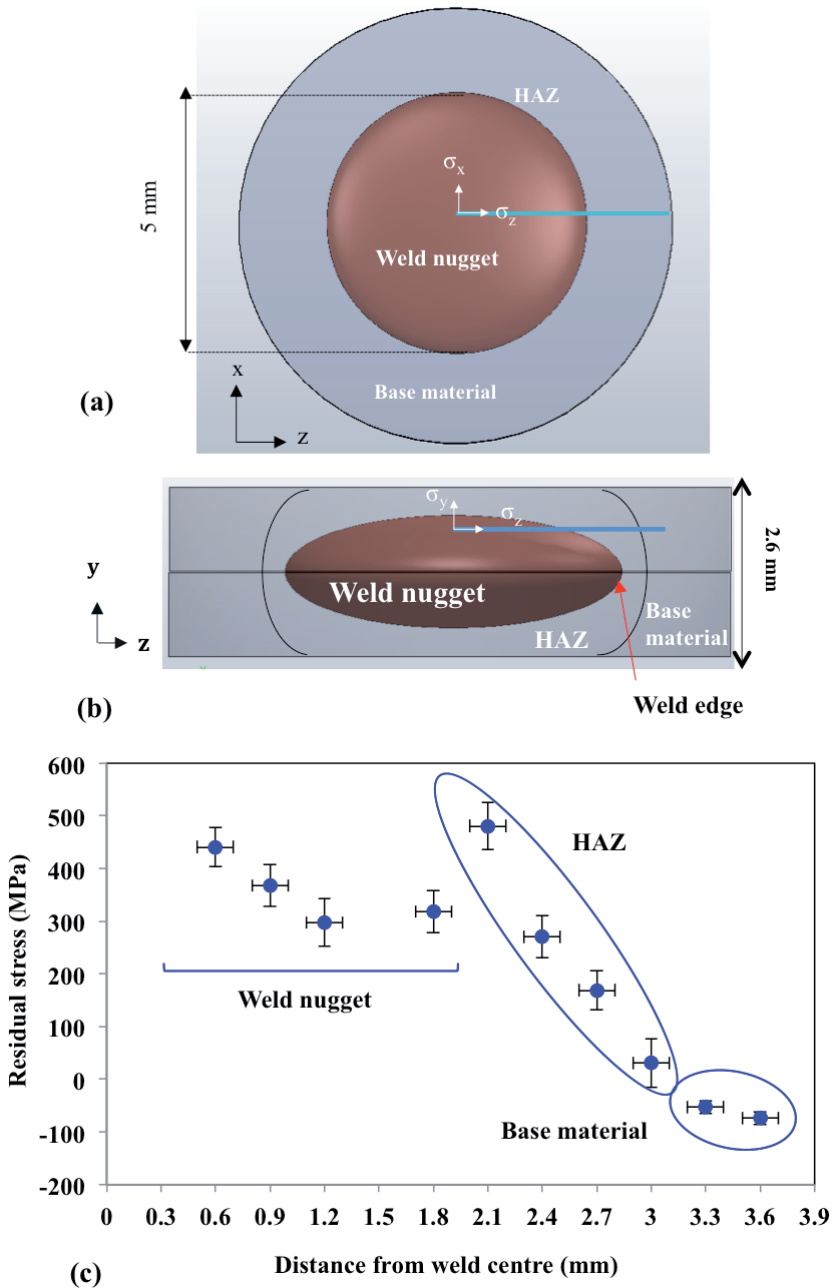
Fig. 6.1 (a and b) Schematic representations of a single pulse weld (sequence 1, I=6.2 kA) from top view and side view, respectively. The blue line indicates the location of the residual stress measurements. The x- and z-components of residual stress were measured and (c) measured z-component of residual stress (σz) along the blue line in (b).

(a)

(b)
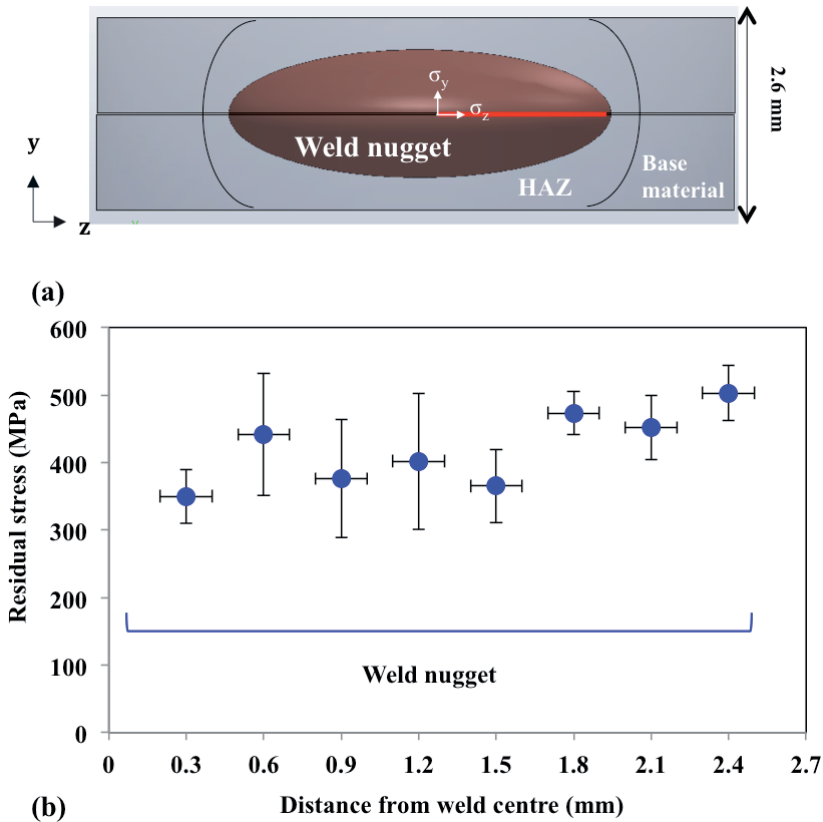
Fig. 6.2 (a) Schematic representation of a single pulse spot weld (sequence 1, I=6.2 kA). The red line indicates the location of the residual stress measurements and (b) measured z-component of residual stress (σz) along the red line in (a).

the base material shows compressive residual stresses near the weld. In general, the residual stress level within the weld nugget of a double pulse weld has reduced compared to the single pulse weld. In Fig. 6.5, the z-component of residual stress (σ_z) as a function of the distance from the weld centre to the weld edge along the weld centre line (red line in Fig. 6.2 a) for a double pulse weld is presented. The residual stress within the weld nugget is again tensile. The data point at 1.2 mm is omitted due to the low peak quality obtained at this location in the experiments.

6.1.2 Residual stress simulation of single and double pulse welds
Fig. 6.6 shows a comparison of the simulated temperature distribution and the weld nugget size of the welding sequence 1 and the cross section of a single pulse resistance weld. Good agreement is found between the simulated and experimental weld nugget size and shape.
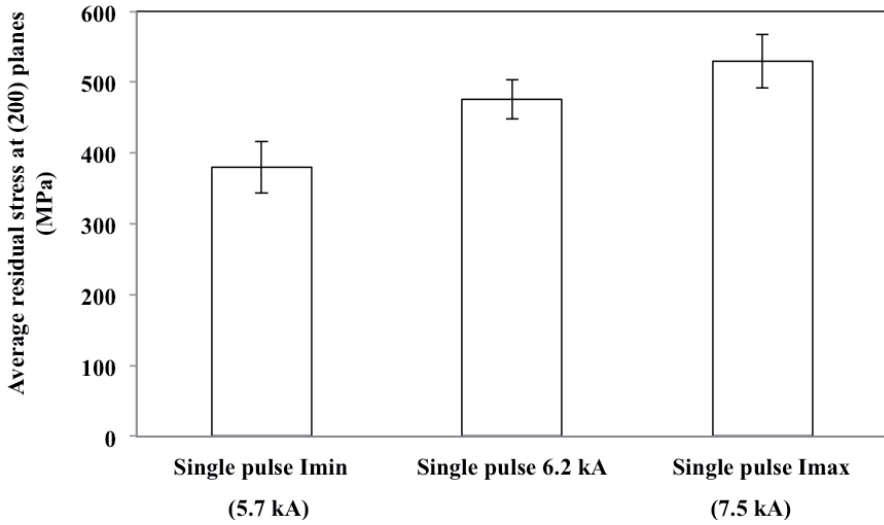
Fig. 6.3 Average residual stress in the (200) planes at the weld edge (red square in Fig. 6.1.a) obtained from 3 measurements for single pulse welds, welded with different welding currents.
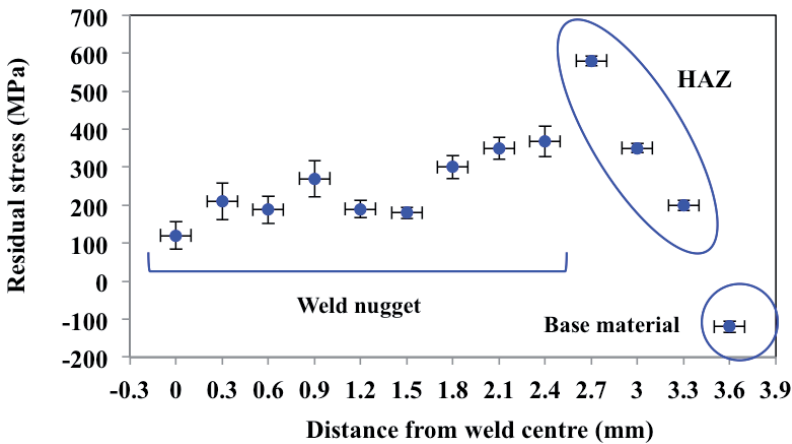
Fig. 6.4. The distribution of the z-component of residual stress (σz) in a double pulse weld along the blue line shown in Fig. 6.1b.

The simulated temperature profiles for the weld centre (indicated by the blue circle in Fig. 6.6) and the HAZ (indicated by the black circle Fig. 6.6) during welding are presented in Fig. 6.7. The heating rate at the weld centre is about 9600 Ks^{-1} and the peak temperature is calculated to be 3374 K. The heating rate in the HAZ is about 3700 Ks^{-1} and reaches a peak temperature of 1496 K. The cooling rate for the weld centre, calculated from the peak temperature until the end of electrode hold time (0.92 s), is about 4650 Ks^{-1}. For the HAZ, this is approximately 2800 Ks^{-1}. After release of the electrodes, the cooling rate
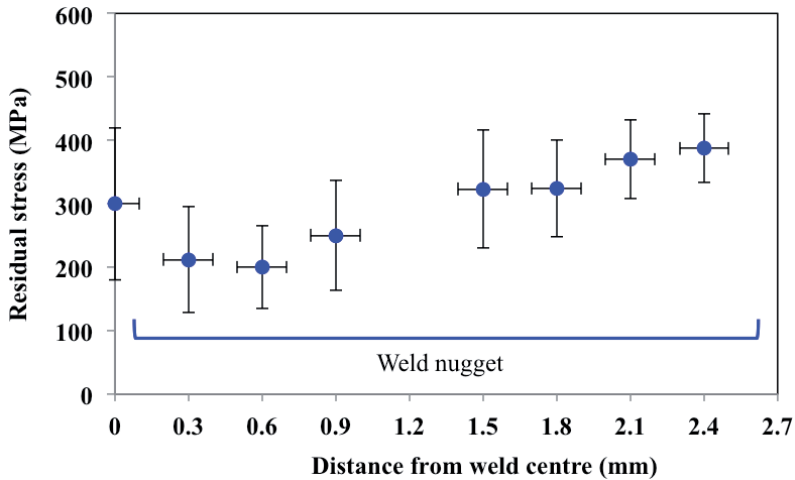
Fig. 6.5 The distribution of the z-component of residual stress (σz) in a double pulse weld along the weld centre line (red line in Fig.6.2 a).
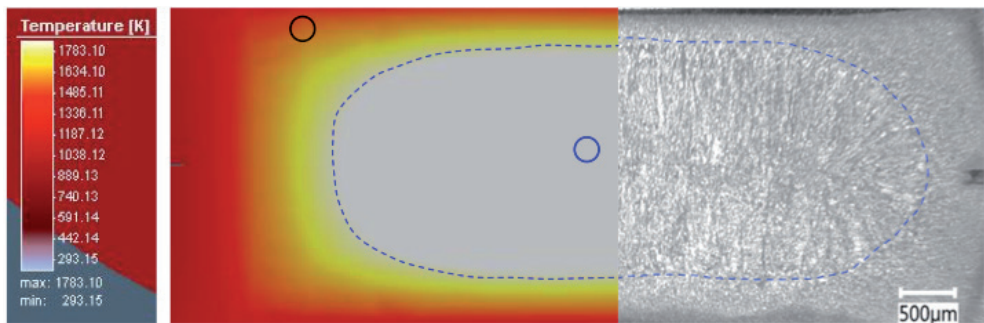
Fig. 6.6 Comparison of simulated temperature profile at peak temperature and a cross section of a single pulse resistance spot weld. The blue circle indicates the area in the weld centre. The black circle indicates the area within the HAZ, where the phase fractions of different phases during welding were extracted.

decreases. It should be mentioned that Simufact predicts a highly super heated liquid weld metal. This can however not be validated experimentally.

Based on the temperature profile in the HAZ (Fig. 6.7), the simulated phase fractions during welding and subsequent cooling in the HAZ (area shown in Fig. 6.6 with the black circle) are obtained and shown in Fig. 6.8. The base material microstructure consists of 80 vol.% bainite, 13 vol.% martensite and 7 vol.% ferrite. During welding, the microstructure becomes austenitic in the heating stage and during cooling the martensitic transformation occurs resulting in a final microstructure consisting of 98 vol.% martensite. The amount of retained austenite is approximately 2 vol.% at this location.
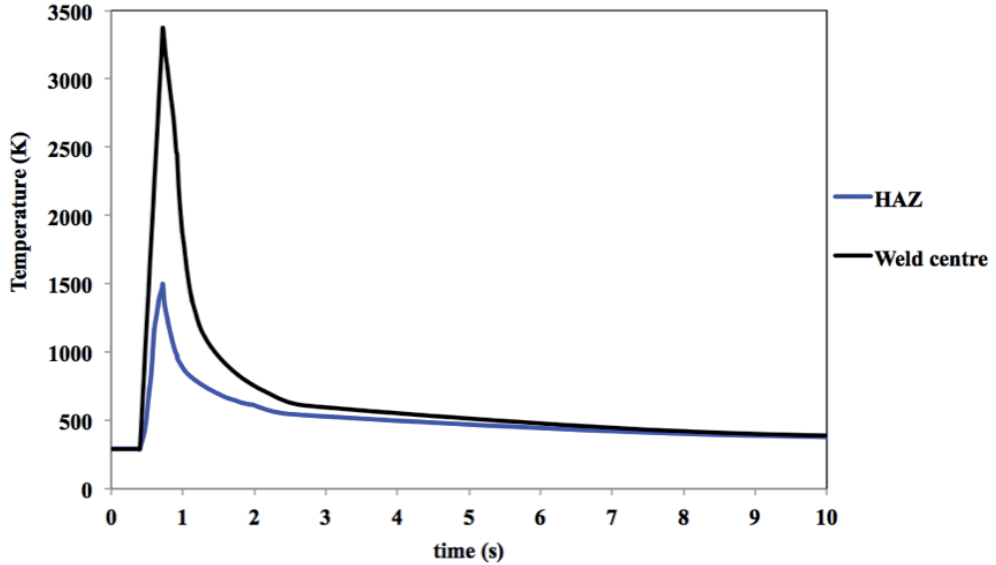
Fig. 6.7 Simulated temperature profile at weld centre, indicated with the blue circle in Fig. 6.6 and HAZ, indicated with the black circle in Fig. 6.7 in a single pulse weld. The squeezing time is 0.4 s, the welding time is 0.32 s and the holding time is 0.2 s.
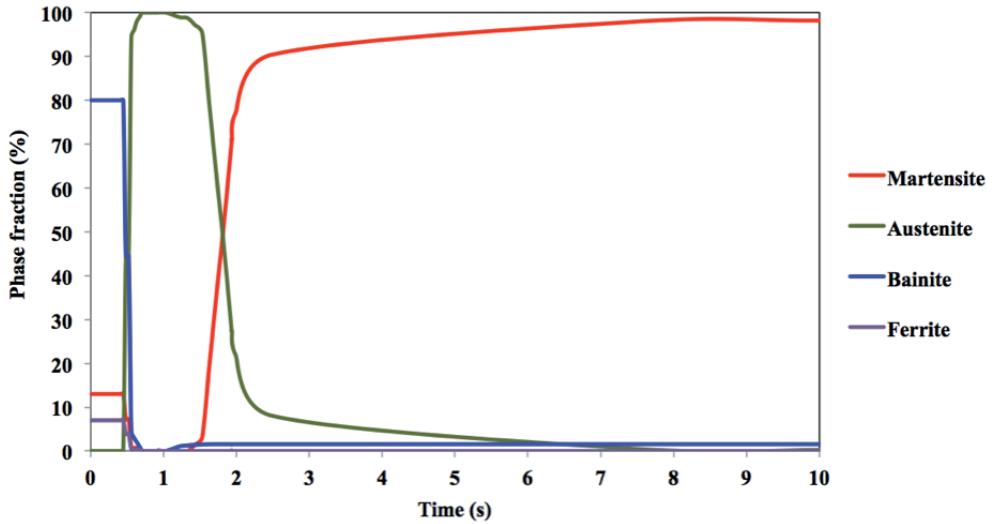
Fig. 6.8 Simulated volumetric phase fraction variation versus time during the RSW processin the HAZ.

The constructed stress model (section 3.5.2) uses the calculated temperature and phase evolution and the temperature dependent material/mechanical properties as input data for the mechanical model.

The simulated z component of residual stress fields for the top surface and the cross section view of a single pulse weld (sequence 1) are shown in Fig. 6.9 a and b, respectively.
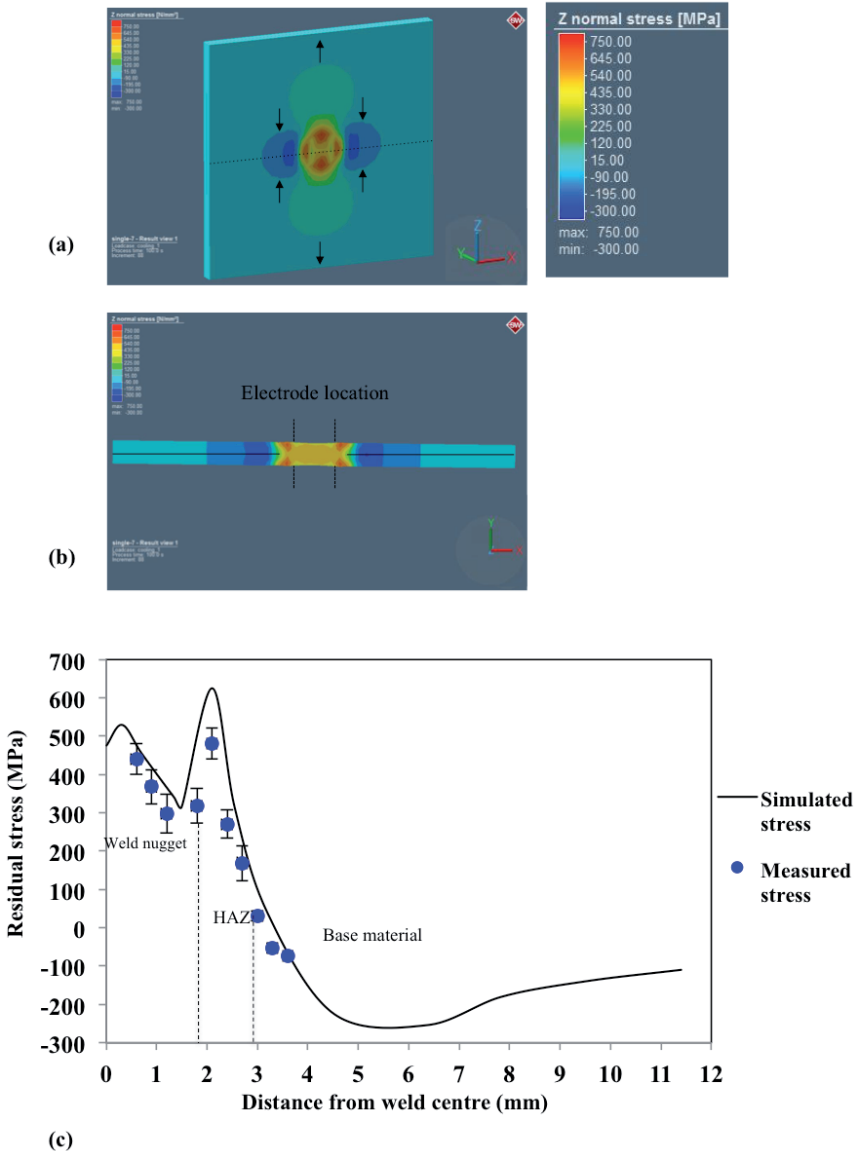
Fig. 6.9 Simulated z-component of residual stress in a single pulse weld, (a) top surface, (b) cross section view and (c) comparison of simulated and measured residual stress.

The stresses are tensile within the weld and the HAZ. The stress value at the weld centre is about 490 MPa. It can be seen that there are relatively high tensile residual stresses at the electrode and sheet interface in the HAZ. The residual stresses in these areas can be in the order of 650 MPa. The residual stress profile of the single pulse weld (along the blue line in Fig. 6.1 a and b) obtained numerically and from experimental synchrotron
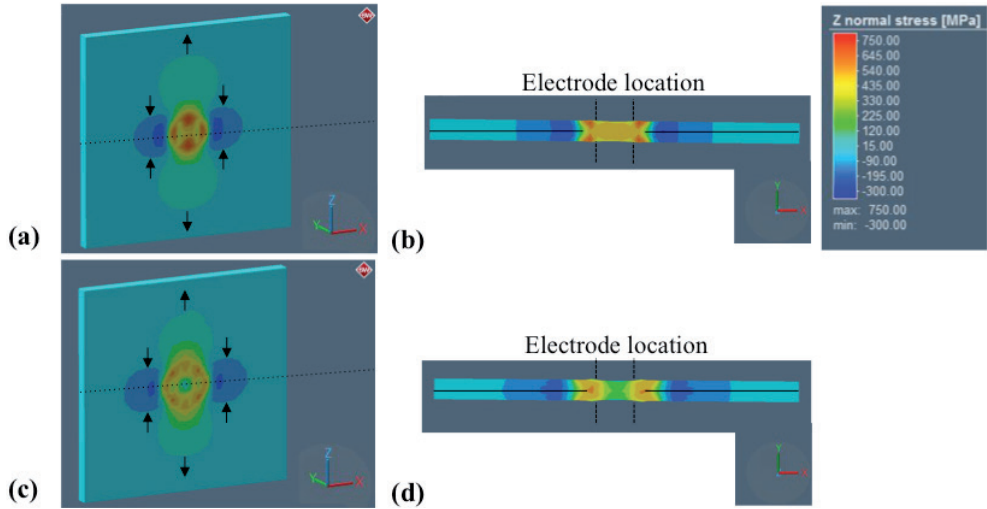
Fig. 6.10 Simulated z-component of residual stress profiles of (a and b) the single pulse weld from top surface and cross section view, respectively and (c and d) the double pulse weld from top surface and cross section view, respectively.
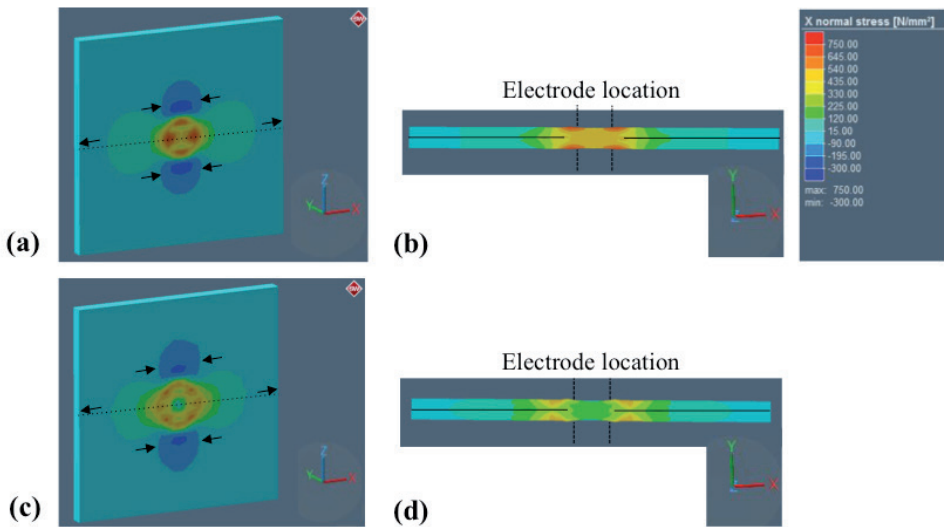
Fig. 6.11 Simulated x-component of residual stress profiles in (a and b) the single pulse weld from top surface and cross section view, respectively and (c and d) the double pulse weld from top surface and cross section view, respectively.

data is shown in Fig. 6.9 c. There is a reasonable agreement between the experimental and numerical results. The numerically calculated residual stress shows a value of about 490 MPa in tensile mode at the weld centre and towards the HAZ, the residual stress initially decreases but shows a maximum at the weld pool edge, after which the residual stress decreases in the HAZ and with increasing distance from the fusion line towards

the base material the stress becomes compressive. The calculated residual stresses tend to zero toward the edge of the plate.

The small deviation between measured and computed residual stress profiles as shown in Fig. 6.9 c, can be explained from two perspectives. The first source of error comes from the input of temperature dependent material properties and the assumptions on the node constraints applied in the model (See section 3.5.2). The deviation may also a result of errors in the experimental measurements in particular originating from the accuracy of the exact location of the weld centre and the fitting of the XRD peaks.

Top surface and the cross section views of the simulated z-component of residual stress distributions in single and double pulse welds are shown in Fig. 6.10 a-d. The simulated residual stresses are tensile in nature within the weld nugget and the HAZ for both the single and double pulse welds. In the base material (near the weld) the residual stresses are compressive in both welds (Fig. 6.10 b and d). The residual stresses are redistributed by double pulsing. The double pulse weld shows an approximate 290 MPa lower tensile residual stresses at the weld nugget in comparison with the single pulse weld. The high residual stress of about 560 MPa in the HAZ at the interface of the electrode and sheet in the single pulse weld has decreased about 360 MPa in the double pulse weld (Fig. 6.10 b and d). The compressive stresses at the base material (near the weld) of a single pulse weld are also about 100 MPa lower in a double pulse weld as a consequence of the self-equilibrium stress principle.

Top surface and the cross section views of the simulated x-component of residual stress distributions in single and double pulse welds are shown in Fig. 6.11 a-d. The double pulse weld shows about 350 MPa lower tensile residual stresses at the weld nugget in comparison with the single pulse weld. As shown in Fig. 6.11 b and d, the high residual stress of about 600 MPa in the HAZ at the interface of the electrode and sheet in the single pulse weld has decreased to an approximately 500 MPa in the double pulse weld.

The von Mises stress profiles for single and double pulse welds are shown in Fig. 6.12. The von Mises stress is calculated from the von Mises yield criterion, indicated in Eq. (6.1). The von Mises stress within the weld centre of the double pulse weld is about 400 MPa lower than in the single pulse weld. Moreover, the von Mises stress distribution is more uniform in the double pulse than the single pulse weld. The source of asymmetry in stress profiles shown in Fig. 6.12 is related to the assumptions on the node constraints applied in the model.

$$\sigma_{von\,Mises} = \sqrt{\frac{(\sigma_z - \sigma_x)^2 + (\sigma_x - \sigma_y)^2 + (\sigma_y - \sigma_z)^2}{2}}. \qquad \text{(Eq. 6.1)}$$

To better understand the stress evolution during resistance spot welding, the simulated von Mises stress during welding of a single pulse weld is provided in Fig. 6.13. During welding, when the current is applied and the melt pool is formed,

(a)   **(b)**
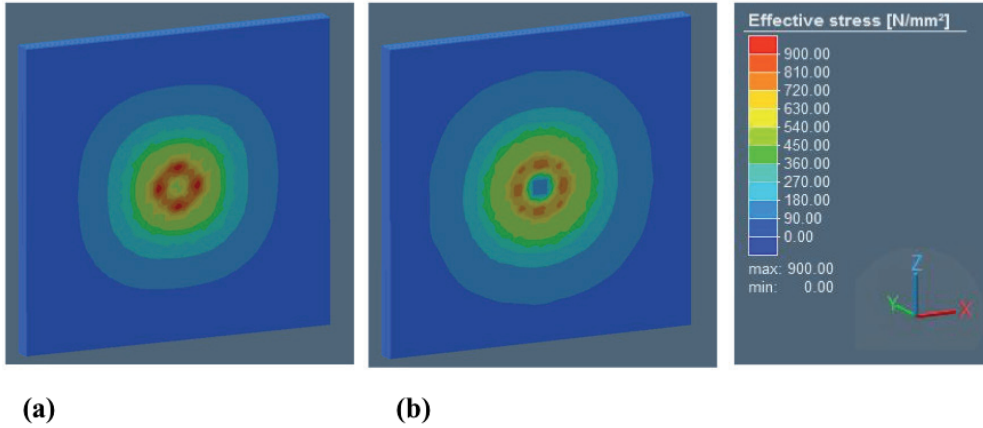
Fig. 6.12 The von Mises stress (effective stress) profiles for (a) single pulse and (b) double pulse welds.

t= 720 ms
Peak temperature
(a)

t= 760 ms
During holding time
(b)

t= 910 ms
During holding time
(c)

t=1300 ms
After electrode release
Peak Temperature: 1100 K
(d)

t= 100000 ms
Room temperature
(e)
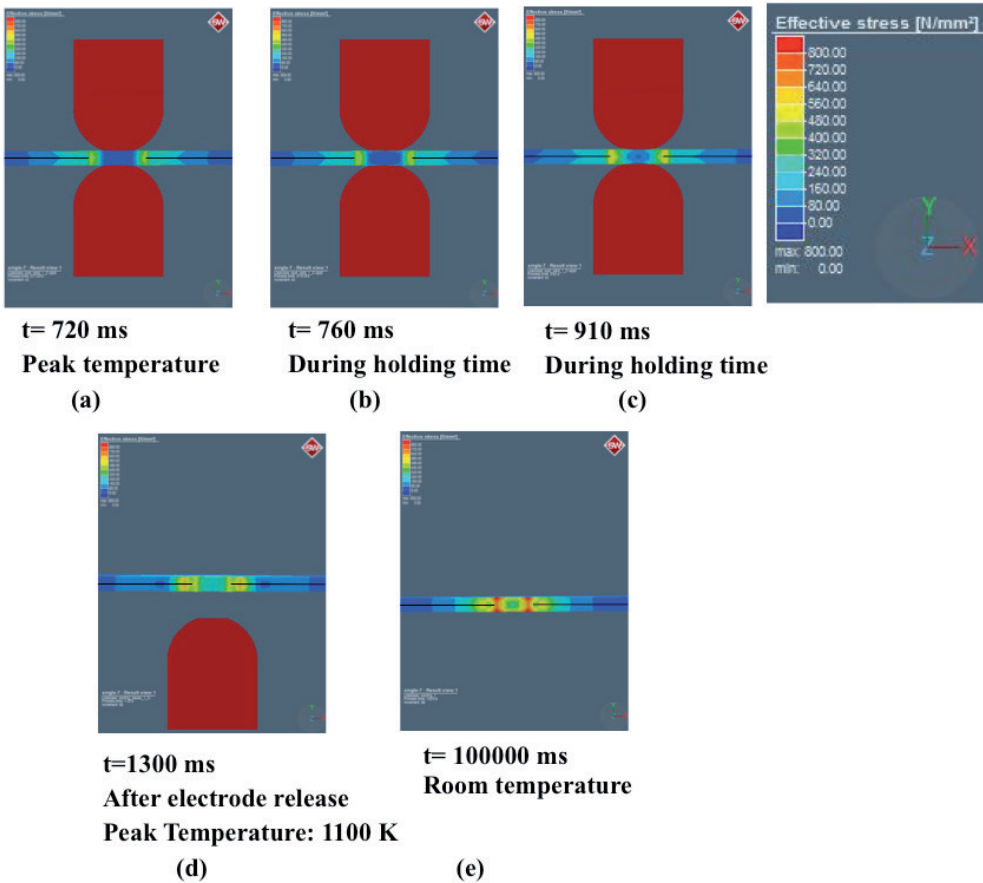
Fig. 6.13 Simulated von Mises stress evolution during RSW of a single pulse weld (i.e. sequence 1), (a) at peak temperature, (b) during holding time, (c) at end of holding time, (d) after electrode release and (e) when the room temperature is reached.
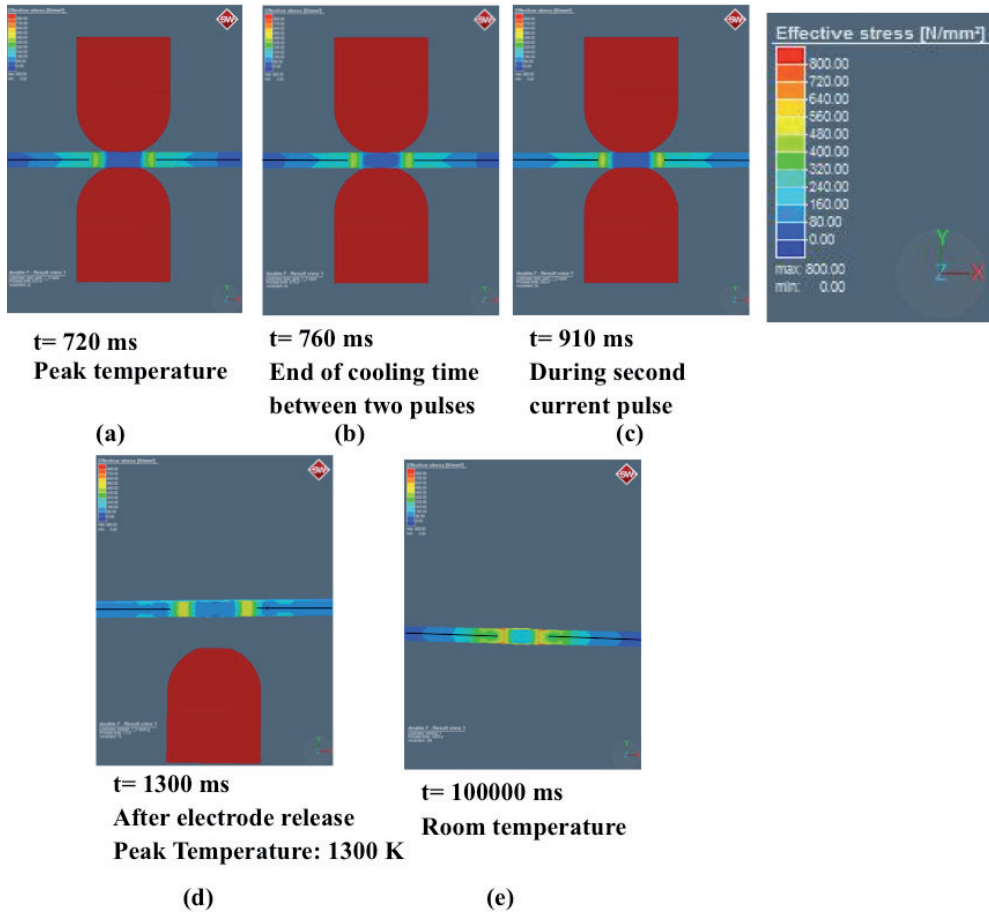
Fig. 6.14 Simulated von Mises stress evolution during RSW of a double pulse weld (*i.e.* sequence 3), (a) at peak temperature, (b) end of cooling time between two pulses, (c) during second current pulse, (d) during holding time and (e) when the room temperature is reached.

the von Mises stress at peak temperature is shown in Fig. 6.13 a. The stress within the material outside the weld pool is predicted to be high and the stresses in and closely around the weld are low due to the low strength of the hot material (Fig. 6.13 a). During holding time, the weld pool cools and starts to solidify and the stress within the material outside the weld pool, *i.e.* the HAZ, starts to increase (Fig 6.13 b and c). At the end of the entire welding cycle, the weld nugget is formed, the electrodes are released and the von Mises stress within the weld nugget and the HAZ develops during cooling (Fig 6.13 d). The residual von Mises stress within the weld nugget and the HAZ, when the temperature has reached room temperature (time=100 s), is shown in Fig 6.13 e.

The simulated von Mises stress evolution during double pulse welding is presented in Fig. 6.14. As mentioned for single pulse welding, when the welding current is applied, a weld pool is formed and the von Mises stress profile at the peak temperature is shown in Fig. 6.14 a. During the cooling time between two pulses, the weld pool becomes smaller as shown in Fig. 6.14 b. During the second current pulse with the same magnitude as the first current pulse, the weld pool size increases (Fig. 6.14 c). However, the size of this weld pool is smaller than the primary weld pool as the resistivity of liquid and the solid is lower than the resistivity of the solid-solid interface between two sheets (See section 4.1.1). During the holding time, the weld pool solidifies and after releasing the electrodes, the von Mises stress is developed within the weld nugget (Fig. 6.14 d). The residual von Mises stress of a double pulse weld is shown in Fig. 6.14 e, indicating about 200 MPa lower stresses within the weld nugget and the HAZ compared to a single pulse weld (Fig. 6.14 e).

6.1.3 Residual stress measurement of the single pulse welds with and without paint bake cycle

The measured x- and z-component of residual stresses (σ_x and σ_z) at the weld edge of a single pulse weld and a single pulse weld subjected to a paint bake thermal cycle (heat treatment of 180 °C for about 20 min) is shown in Fig. 6.15. The results show that after the paint baking thermal cycle is applied; the residual stress at the weld edge has decreased about 110 MPa in σ_x and about 130 MPa in σ_z. The difference between the two x- and z-stress components (σ_x and σ_z) for the single pulse weld and the sinlge+PB weld is attributed to the effect of the presence of the weld edge. The z-component (σ_z) is higher than the x-component (σ_x), because during cooling, there is no material in the z-direction to accommodate the stress due to the residual gap between the two plates, however, in the x-direction, the cold material accommodates the stress formed.

6.1.4 Micro-residual strain measurement of a weld using FIB ring-core milling technique

The weld edge area (indicated by a red square in Fig. 6.1 b) was selected from the weld cross-section for the assessment of stress levels obtained via the relaxation strains using the FIB ring-core milling technique. The experimental details of this technique are provided in section 3.4.3. The size of the selected area for this measurement is in the order of a few μm. No prior austenite grain boundaries are present within this area. As discussed in section 4.1.2, the microstructure at the weld edge is a lath martensite. Relaxation strain measured across the horizontal diameter of the pillar as a function of the milling progress; *i.e.,* milling distance with a milling step of about 0.02 μm is illustrated in Fig. 6.16. The results show that the relaxation strain during milling is negative, indicating that tensile stresses are present. After about 0.8 μm milling, no
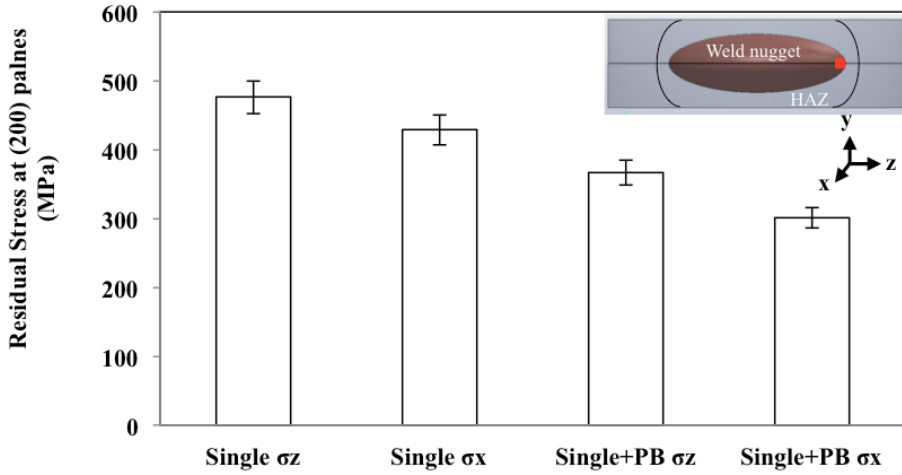
Fig. 6.15 Measured x and z-component of residual stress based on the (200) planes at the weld edge (red square in the insert figure) of the single pulse weld (6.2 kA) and single pulse+paint bake thermal cycle (PB) weld.
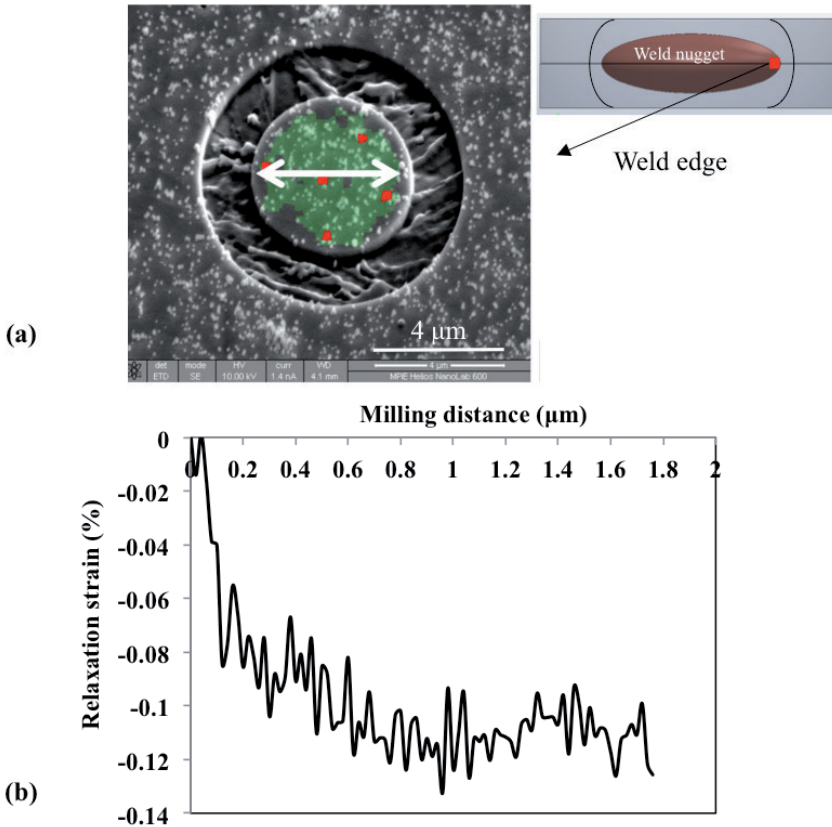
Fig. 6.16 (a) SEM image of the final milling step of the single pulse weld and (b) horizontal average relaxation strain of the pillar versus the applied milling distance as calculated using the Matlab® based DIC code [12].

additional change in relaxation strain is observed (Fig. 6.16) indicating that the residual stress is released. The micro-residual stress is tensile (in z-direction) at the weld edge of a single pulse weld and is calculated from the relaxation strain using Hooke's law to be 458 MPa.

The preparation for this technique requires cross sectioning of the sample, which will affect the stress state; therefore direct comparison with synchrotron X-ray diffraction results is not indicated. However, the tensile nature of the stress at this location can be confirmed.

6.2 Discussion

Residual stresses are defined as self-equilibrating stresses in materials without external loading. Generally, there are three types of residual stresses with respect to the scale over which they are acting [13]. The first type represents a macro-stress. The macro-stress acts over a long range of at least several grains. The second type is a micro-stress, which covers a distance of one grain or even smaller. The third type is the residual stress on an atomic scale. The measured residual stress via the synchrotron X-ray diffraction technique is of the first type. The FIB ring-core milling technique provides a combination of the first and second type of the residual stresses.

The residual stress simulation and measurement using synchrotron X-ray diffraction show a tensile residual stress within the weld nugget. This stress is due to solidification shrinkage of the molten nugget and thermal contraction during cooling until the ambient temperature is reached. The average residual stress within the weld nugget of a single pulse weld is about 480 MPa, which is considerable compared to the yield strength of the base material, 660 MPa and the strength of the martensitic weld nugget, which is in the order of 1000 MPa. The HAZ also exhibits a tensile stress due to thermal contraction. This contraction is constrained by the surrounding material. As a consequence, the base material shows compressive residual stresses near the weld to maintain equilibrium in the work piece.

The cross-section views of the simulated z-component of residual stresses and the von Mises stress for a single pulse weld, Fig 6.9 b and Fig. 6.13 e, respectively, show that the highest residual stress of about 650 MPa is predicted to be near the electrode and sheet interface in the HAZ. During welding, the sheet is plastically deformed at its interface with the electrodes due to the applied force by the electrodes and the thermal mechanical cycle applied to the material. In the area near the electrode and sheet interface in the HAZ, where no plastic indentation is observed, the residual stresses are high. As shown in Fig. 6.9 c, moving from the weld nugget and the HAZ towards the base

material, the residual stresses decrease in the base material near the weld, compressive residual stresses are calculated and the stresses tend to zero toward the edge of the plate.

An increase in the welding current (5.7 kA to 7.5 kA) results in a residual stress increase (380 MPa to 530 MPa) within the weld nugget (Fig. 6.3). A higher welding current produces a larger weld nugget and hence, the residual stresses obtained during solidification and contraction of the weld pool are higher compared to a weld subjected to a lower welding current [3]. It has also been reported by Anastassiou [14] that increasing the welding current increases the weld nugget size and residual stresses within the weld.

Uncertainties in the residual stress measurement and simulation results are related to several factors. The source of errors in the experimental results can be divided into errors from the source of X-ray (wavelength variations, sample positioning and definition of the exact location of the weld centre), errors originating from the sample (grain statistics, homogeneity of the sample and distribution of the alloying elements), and errors from the data processing (stress free lattice spacing, elastic constants and XRD peak fitting). It should be mentioned that in this work stress free lattice spacing was considered different to be in each weld region according to the microstructure *i.e.* at the weld nugget, the HAZ and the base material (described in section 3.4.2). The errors presented in this chapter are calculated from peak fitting statistics. As shown in Fig. 6.1 c, the error bars of residual stresses within the weld nugget of a single pulse weld is about ±50 MPa, however in the base material, the error bars are smaller. The errors in the measured residual stress of the weld nugget zone become lower in the base material due to the better diffraction peak quality in this zone. As can be seen in Fig. 6.2 and Fig. 6.5, the errors calculated within the weld nugget of the single and double pulse welds are in the order of ±100 MPa and are relatively high. The large errors within the weld nugget zones come from low XRD peak quality due to the large grain size. Moreover, the residual stresses measured in the half thickness of the plate in the double pulse weld (Fig. 6.4) have smaller error bars compared to the same locations in a single pulse weld (Fig. 6.1 c), this can again be related to the microstructural changes; *i.e.* grain refinement during double pulsing at the annealed zone (see section 4.1.1).

The source of errors in the simulation results comes from the input of temperature dependent material properties, the assumptions on the node constraints applied in the model (see section 3.5.2) and the limitation of the finite element model in the prediction of the microstructural changes such as grain growth and carbide precipitation. Given the errors in the experimental and the simulation results, the results obtained are in good agreement.

The simulated and measured residual stresses of single and double pulse welds can be related to the results of tensile shear strength (TSS) testing of the welds. This is due to the direction of the measured residual stresses using synchrotron X-ray diffraction. During TSS testing, shear loading is applied to the weld and the stress distribution is

shown in Fig. 6.17 [15]. In reality, the loading in TSS is complex and mode I loading at the weld edge also occurs. The in-plane stress components contribute in crack initiation during shear loading. The results obtained from TSS testing of the welds are presented in Table 6.1. The maximum load obtained for the single pulse weld (sequence 1) is 18.1 kN, while the maximum load for the double pulse weld (sequence 3) is 23.2 kN. The failure mode of the double pulse weld is improved and shows the favourable full plug failure (PF). In the single pulse weld, the tensile in-plane residual stress is higher than the double pulse case, thus during shear loading in the single pulse weld, the crack initiates easily and the failure mode is partial interfacial failure (PIF). However, in the double pulse weld, the lower tensile in-plane residual stress contributes in improved mechanical performance of the weld during TSS testing. The changes in microstructural features at the weld edge by double pulsing (as discussed in section 4.1.2) can affect the residual stress distribution (*i.e.* lower residual stress in the equi-axed grains compared to the dendritic grains) and the mechanical performance of the welds.

In a double pulse resistance spot weld, the residual stress within the weld nugget and the HAZ are also tensile, however the magnitude has decreased in comparison with the single pulse weld (Fig. 6.4). This can be attributed to the application of the second current pulse. Following the second current pulse, a smaller weld nugget than a primary weld nugget solidifies and forms the secondary weld nugget. The remaining area of the primary weld nugget is annealed, grain morphology and structure are modified and elemental segregation is reduced in this zone (see section 4.1.2) resulting in the residual stress reduction within the weld nugget and HAZ. After applying a paint baking cycle, the residual stress at the weld edge of the resistance spot welds is decreased by average of about 120 MPa, presumably due to ε-carbide precipitation during tempering of the martensite (see section 5.1.1).

The residual stress state can affect the mechanical performance of the work piece either favourably or adversely. The tensile residual stresses in the presence of external tensile loading can be detrimental. Therefore, the decrease in tensile residual stress of the weld nugget and HAZ after double pulsing and/or a paint bake cycle could possibly contribute in improving the tensile shear strength of the welds.

The micro-residual stress measurement of a single pulse weld using FIB ring-core milling shows a tensile residual stress at the weld edge of a single pulse weld on a micro-scale. The nature of the strain/stress (tensile) is in agreement with the residual stress measurements using synchrotron X-ray diffraction. It should be mentioned that Archie *et al.* [16] have measured the micro-residual stresses in a lath martensitic microstructure of a medium carbon steel by FIB core-ring milling. The residual strains were identified to be tensile. These micro-strains were attributed to the martensitic transformation of the steel and were a maximum of 0.07 %. However, in our case, the residual micro-strains
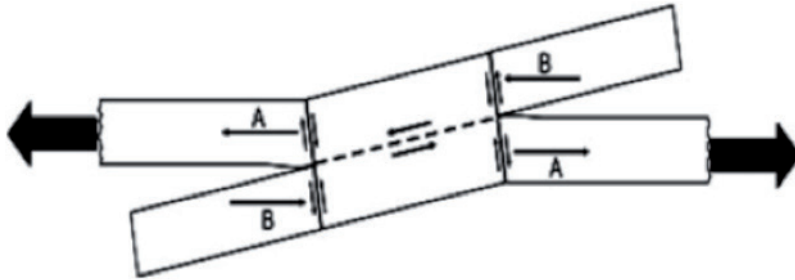
Fig. 6.17 Stress distribution at nugget centreline and circumference during TSS testing [15].

Table 6.1 Results obtained from TSS testing of the resistance spot welds.

Weld	TSS maximum load (kN)	Failure mode
Single pulse (6.2 kA) (Sequence 1)	18.1	PIF
Double pulse (6.2 kA-6.2 kA) (Sequence 3)	23.2	PF

are higher (maximum of 0.13 %) and this is attributed to the resistance spot welding process, which includes melting and solidification of the material and the effect of loads from electrodes during the whole welding process.

6.3 Conclusions

The residual stresses of a single pulse weld were simulated and verified using synchrotron X-ray diffraction data. Based on the results obtained in this chapter, the following conclusions can be drawn:

1. The changes in residual stresses, elemental distribution and microstructures at the weld edge of single and double pulse welds have been investigated and all these changes can have influence on the improved tensile shear strength test results, *i.e.* weld strength and the failure mode for a double pulse weld. However, their relative contributions cannot be determined.

2. Residual strain measurement at the weld edge of a spot weld using both FIB ring-core milling and synchrotron X-ray diffraction revealed tensile residual strains due to solidification shrinkage of the molten nugget and thermal contraction during cooling until the ambient temperature is reached.

3. The validated FE-based thermal-mechanical numerical model can be used to ascertain the residual stresses in spot welded AHSSs.

References

[1]   S.K. Khanna, X. Long, *Residual stresses in resistance spot welded steel joints*, Sci. Technol. Weld. Join. 13(3) (2008) 278–288.

[2]   I.R. Nodeh, I.R. Serajzadeh, A.H. Kokabi, *Simulation of welding residual stresses in resistance spot welding*, FE modeling and X-ray verification, J. Mater. Process. Technol. 205 (2008) 60–69.

[3]   H. Moshayedi, I. Sattari-Far, *Resistance spot welding and the effects of welding time and current on residual stresses*, J. Mater. Process. Technol. 214 (2014) 2545–2552.

[4]   B.W. Cha, S.J. Na, *A study on the relationship between welding conditions and residual stress of resistance spot-welded 304-type stainless steels*, J. Manufac. Sys. 22 (2003) 181–189.

[5]   D. Bae, I. Sohn, J. Hong, *Assessing the effects of residual stresses on the fatigue strength of spot welds– Residual stress at the nugget's edge was taken into consideration in the evaluation of fatigue strength for spot welds of various shapes and dimensions*, Weld. J. 82 (2003) 18–23.

[6]   M. Sedighi, D. Afshari, F Nazari, *Investigation of the effect of sheet thickness on residual stresses in resistance spot welding of aluminum sheets*, Proc. IMech Part C: Journal of Mechanical Engineering Science 232(4) (2018) 621-628, DOI: 10.1177/0954406216685124.

[7]   R.S. Florea, C.R. Hubbard, K.N. Solanki, D.J. Bammann, W.R. Whittington, E.B. Marin, *Quantifying residual stresses in resistance spot welding of 6061-T6 aluminum alloy sheets via neutron diffraction measurements*, J. Mater. Process. Technol. 212 (2012) 2358–2370.

[8]   K. Khanna, C.L. He, H.N. Agarwal, *Residual Stress Measurement in Spot Welds and the Effect of Fatigue Loading on Redistribution of Stresses Using High Sensitivity Moire ' Interferometry*, J. Eng. Mater. Technol. 123 (2001) 132-138.

[9]   A. Chabok, *Resistance spot welding of advanced high strength steels: Mechanical properties and failure mechanisms*, thesis, University of Groningen (2019).

[10] E.M. van der Aa, *Local cooling during welding: prediction and control of residual stresses and distortion*, thesis, Delft University of Technology (2007).

[11] M. Peel, A. Steuwer, M. Preuss, P.J. Withers, *Microstructure, mechanical properties and residual stresses as a function of welding speed in aluminium AA5083 friction stir welds*, Acta Mater.51 (2003) 4791-4801.

[12] M. Senn, *Digital Image Correlation and Tracking*, MathWorks, 02 July 2016 [Online]. Available: http://it.mathworks.com/matlabcentral/fileexchange/ 50994-digital-image-correlation-and-tracking (Accessed 1 August 2017).

[13] J. Lu, ed. *Handbook of Measurement of Residual Stresses*, The Fairmont Press, Georgia (1995).

[14] M. Anastassiou, *Residual stresses and microstructure distribution in spot-welded steel sheets: Relation with fatigue behaviour*, Mater. Sci. Eng. A125 (1990) 141-156.

[15] M. Pouranvari, H.R. Asgari, S.M. Mosavizadch, P.H. Marashi, M. Goodarzi, *Effect of weld nugget size on overload failure mode of resistance spot welds*, Sci. Technol. Weld. Join. 12(3) (2007) 217-225.

[16] F. Archie, M. Zeeshan Mughal, M. Sebastiani, E. Bemporad, S. Zaefferer, *Anisotropic distribution of the micro residual stresses in lath martensite revealed by FIB ring core milling technique*, Acta Mater. 150 (2018) 327-338.

6

CHAPTER 7

Study on effects of elastic and plastic loading on BCC phase transformations of CR700Y980T-DH-GI steel[1]

In this chapter, the effect of plastic and elastic mechanical loading on the FCC to BCC phase transformations of CR700Y980T-DH-GI steel during cooling, using *in-situ* synchrotron diffraction is described.

During steel production and in sheet forming processes as well as joining processes like resistance spot welding, mechanical loading is applied that affects the behaviour of solid-state phase transformations in the steel. It has been reported that in hot pressing processes, non-isothermal deformation in austenite promotes ferrite and/or bainite formation prior to the martensitic transformation and that the martensite start temperature (M_s) decreases [1-4]. If the austenite is plastically deformed, it will be strengthened. M_s decreases with an increase in yield strength of the austenite and this can be explained by a dislocation stabilization mechanism [5-8]. He *et al.* reported that M_s increases with strain after small deformations and decreases with strain after large deformations of austenite in the plastic regime [9].

In resistance spot welding, a constant load (stress range of 100-200 MPa) is applied by the two electrodes. It can be expected that the solid-state phase transformations occurring after the formation of the weld will be affected by this applied load. *In-situ* synchrotron diffraction is a suitable technique to study these solid-state phase transformations [10-16]. Dutta *et al.* observed that loading conditions below the yield strength of austenite, lead to elastic strains upon the martensitic transformation and M_s increases with an increase in the applied external tensile load [17].

From a thermodynamic point of view, a reduction in Gibbs free energy of a system indicates whether it is favorable for phase transformations to take place. The total Gibbs free energy is the sum of a chemical and a mechanical component. The chemical free energy component of austenite and martensite as a function of temperature is shown schematically in Fig. 7.1 [18]. At T_0 both austenite and martensite have equal Gibbs free energies. At a certain temperature (M_s) lower than T_0, the energy difference (ΔG_{Ms}) between the two phases becomes sufficient to initiate the transformation and martensite starts to form spontaneously (M_s). At temperatures between M_s and T_0 (for example T_1), although the martensite Gibbs free energy is lower than that of austenite, the transformation does not occur, as there is a free energy barrier that must be overcome for the transformation to occur. A critical elastic energy (U') is required to initiate the nucleation of martensite at T_1. To activate the martensitic transformation at temperatures between M_s and T_0, the Gibbs free energy should be enhanced by energy available from the applied external load [18].

The effects of mechanical loading above the yield stress of austenite and BCC phases on the microstructure development are not yet fully understood. In the present work, *in-situ* synchrotron X-ray diffraction experiments have been conducted to explore the effect of constant loading below and above the yield stress of austenite on the subsequent solid-state phase transformations. A schematic illustration of the thermal-mechanical cycles applied is shown in Fig. 7.2. The loads of 50, 100, and 150 N are approximately
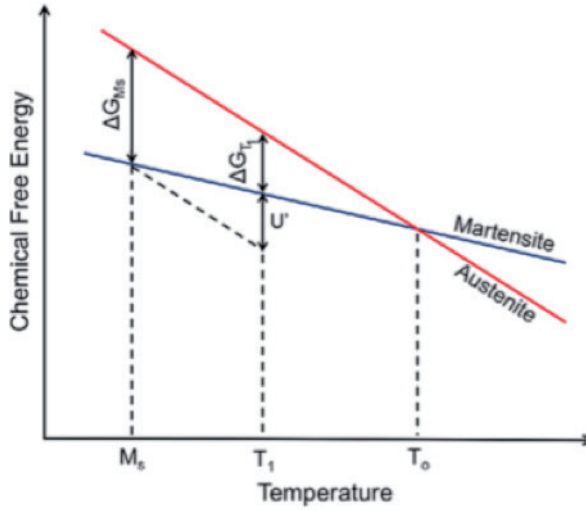
Fig. 7.1 Chemical component of the Gibbs free energy of austenite and martensite [18].
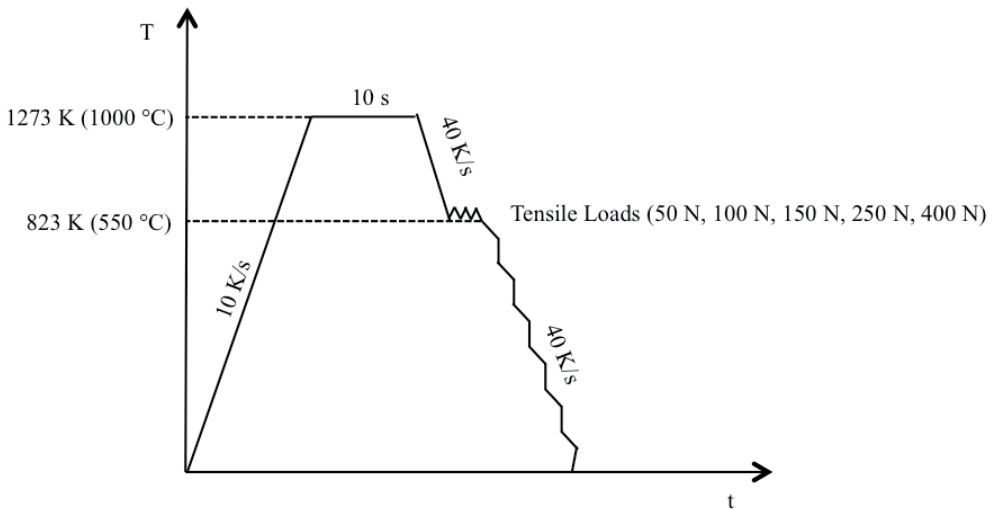
Fig. 7.2 Schematic illustration of the thermal-mechanical cycles applied.

equivalent to the stresses of 33, 67 and 100 MPa, which are below the yield stress of the material at 550 °C, while the 250 and 400 N loads (167 and 267 MPa) are equal to and higher than the yield stress. Time-temperature-load dependent diffraction patterns were recorded to study the phase fractions and kinetics of transformations for different thermal-mechanical cycles. It should be mentioned that the martensitic phase is included in the BCC fraction during analysis. Detailed experimental and data analysis procedures are reported in section 3.4.1.
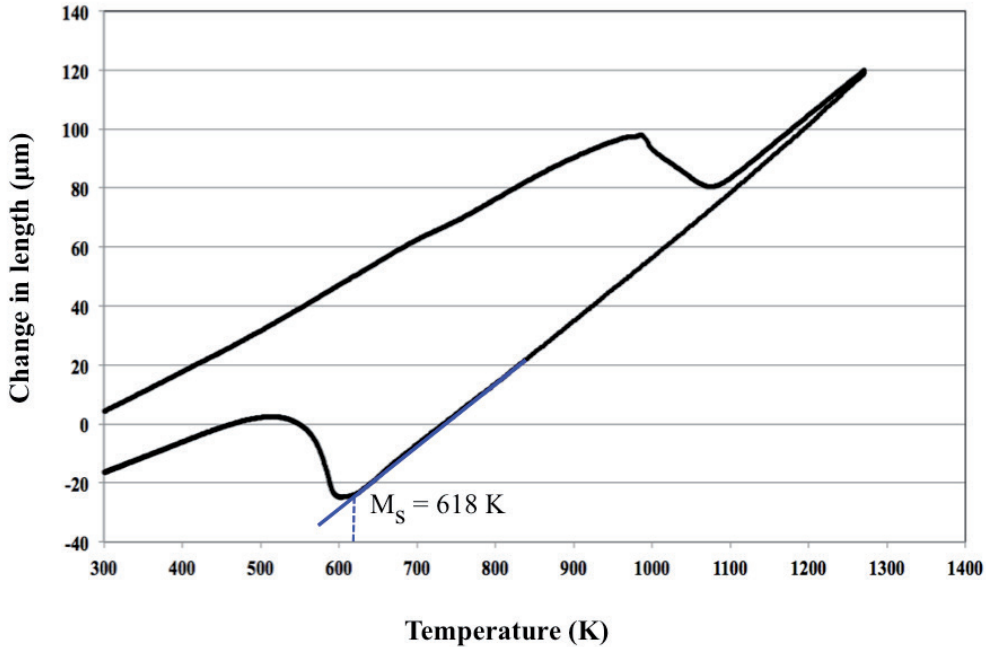
Fig. 7.3 Dilatometer curve for heating until 1273 K and subsequent quenching (a cooling rate of 400 Ks-1 to room temperature is derived from the dilatometer data).

7.1 Results

According to dilatometery experiments for the steel studied, M_s in the absence of loading is 618 K (345 °C), as shown in Fig. 7.3. The fraction of martensite and the kinetics of the martensitic transformation as a function of temperature obtained from the dilatometery data are shown in Fig. 7.4 a and b, respectively.

7.1.1 Phase transformations during cooling and the application of a load
The BCC phase volume fractions as a function of the temperature during cooling for different applied loads are shown in Fig. 7.5. The BCC volume fraction as a function of time between 873 K (600 °C) and 473 K (200 °C) is also presented in the insert.

a)   Initial BCC phase transformation (isothermal holding and application of load)

The initial BCC phase transformation occurs at 823 K (550 °C), where the load is applied (Fig. 7.5). As can be seen, by increasing the load, the BCC phase volume fraction at this constant temperature of 823 K (550 °C) increases. For all the samples, after applying the load at 823 K (550°C), the BCC phase fraction starts to increase. In the sample subjected to a 400 N load, a volume percent of 2% BCC phase is already present before applying the load (at 823 K (550 °C)). After applying the load, the BCC phase
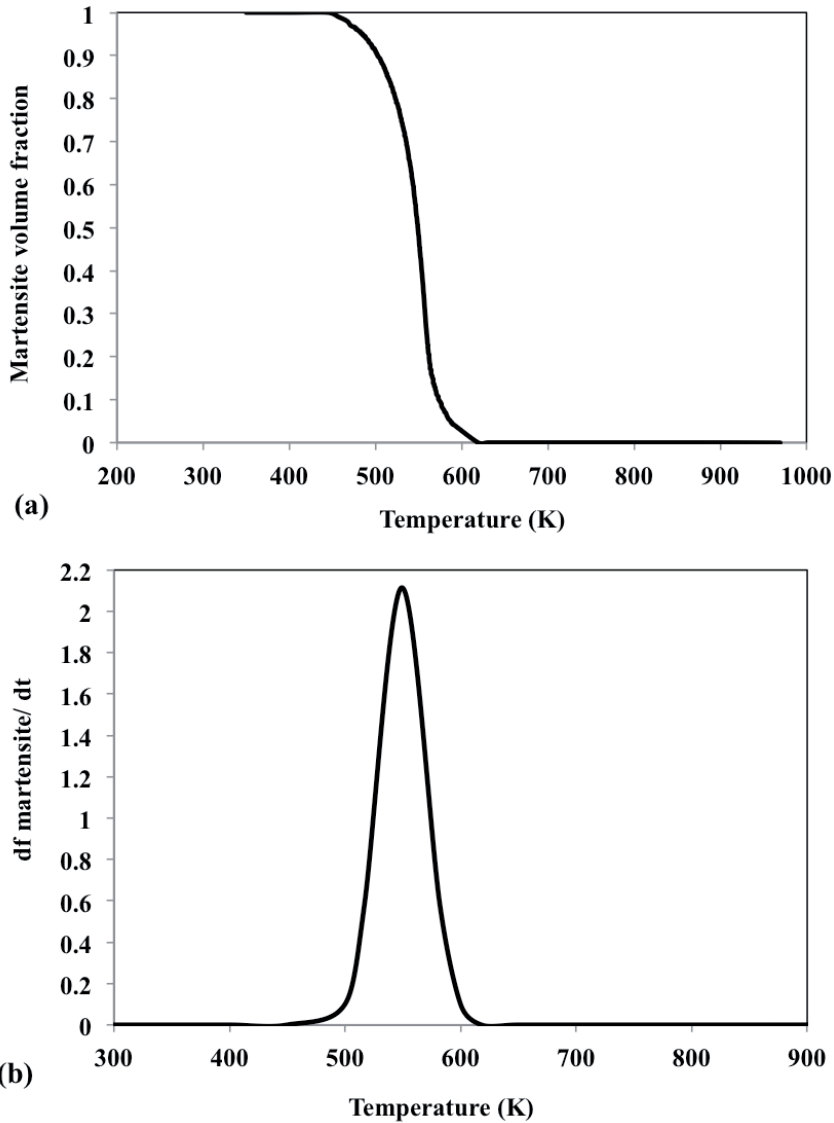
Fig. 7.4 (a) Martensite volume fraction as a function of temperature during cooling and (b) kinetics of martensitic transformation during cooling obtained from dilatometery.

fraction has increased to around 27 % and this sample has the highest increase in BCC phase fraction at 823 K (550 °C).

b) Phase transformation during subsequent cooling (Martensitic transformation)

Upon subsequent cooling, the BCC volume fraction gradually increases for each of the loads. A steep increase in the BCC phase fraction when cooling below a certain temperature, especially for small loads, gives evidence that the martensitic
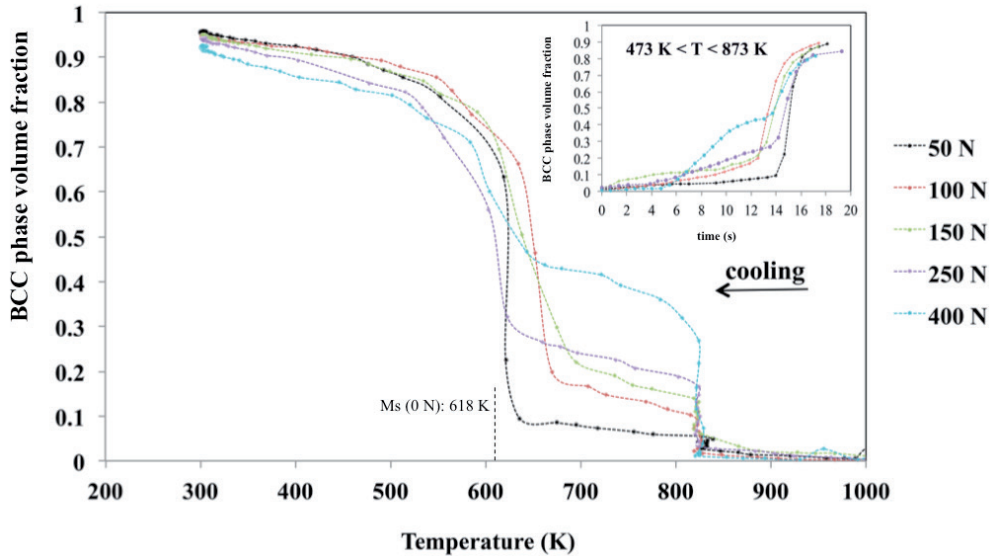
Fig. 7.5 BCC phase volume fraction as a function of temperature during cooling for different heat treatment cycles. The insert shows the BCC fraction a s a function of time, where t=0 is the time cooling starts at T=1000 K, at t=4.5 s the mechanical load is applied. Ms for 0 N loading condition obtained from dilatometer curve presented in Fig. 7.3.

Table 7.1 The martensite start temperature (Ms) for different samples

Sample	Estimated M_s K (°C)
0 N	618 K (345 °C)
50 N	636 K (363 °C)
100 N	670 K (397 °C)
150 N	695 K (422 °C)
250 N	623 K (350 °C)
400 N	663 K (390 °C)

transformation takes place (Fig. 7.5). It should be noted that the martensitic phase is included in the total BCC fraction as mentioned before.

The estimated martensite start temperature (M_s) from the available data for 50 N, 100 N, 150 N, 250 N and 400 N samples are shown in Table 7.1. M_s increases with increasing applied stress below the yield stress. In the case of a 250 N load, the applied stress is approximately at the yield stress of the material at 823 K, whereas at 400 N, it is higher than the yield stress. In these loading cases, M_s is reduced in comparison to M_s obtained from samples loaded in the elastic regime.

7.1.2 Kinetics of phase transformations during cooling

The kinetics of the phase transformation during cooling are presented in Fig. 7.6. The curves show the transformation rate as a function of the temperature. The kinetics of the
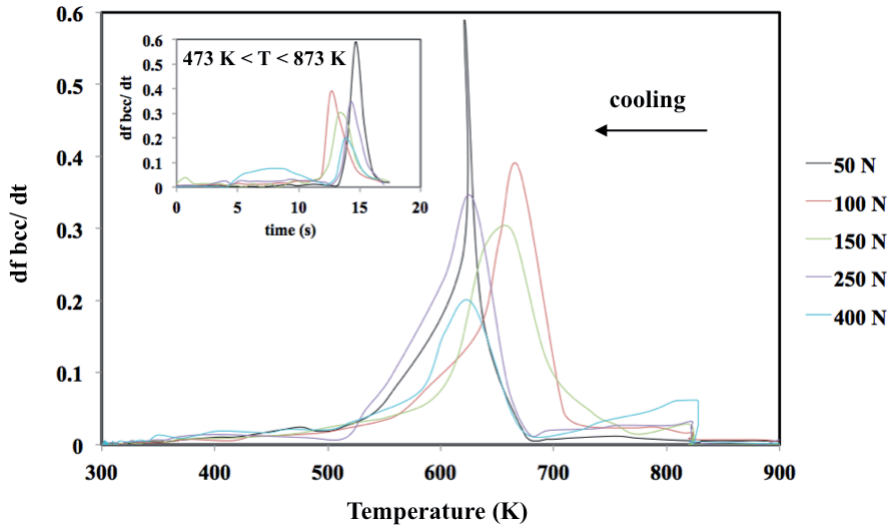
Fig.7.6 Kinetics of BCC phase transformations during cooling for heat treatment cycles.

BCC phase transformation versus time in the temperature range between 873 K (600 °C) and 473 K (200 °C) is presented in the insert in this figure.

The kinetics of the initial BCC phase transformation at 823 K (550 °C) increase with the level of the applied load and is highest for the sample subjected to 400 N in comparison with the other thermal-mechanical cycles.

Upon further cooling after the holding time, the maximum transformation rate in each load case is related to the martensitic transformation and it is achieved at different temperatures. In the sample subjected to a 50 N load, the martensite transformation kinetics is highest. For higher loads of 100 N, 150 N, 250 N and 400 N the martensitic transformation kinetics become slower. The slowest martensitic transformation is related to the sample subjected to a load of 400 N.

7.1.3 Austenite lattice parameter

The austenite lattice parameter obtained from the d-spacing of the austenite peaks for different thermal mechanical cycles is shown in Fig. 7.7. The austenite lattice parameter decreases during cooling. Under constant load at 823 K, the austenite lattice parameter increases. Applying higher loads results in a larger increase in the austenite lattice parameter. Upon further cooling again a reduction in austenite lattice parameter is found. It can be seen than between 700 K and 600 K, the reduction in austenite lattice parameter is most pronounced for the loading case of 50 N as the martensitic transformation takes place and the austenite lattice is under compression due to the large amount of martensite formed within the sample (volume fraction of BCC phase is about 0.65 at 623 K as shown in Fig. 7.5).
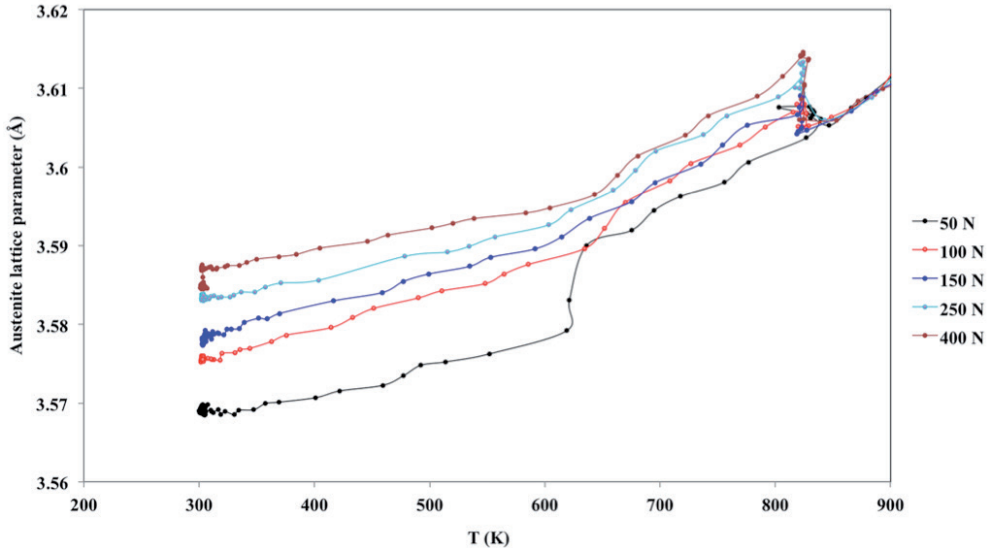
Fig. 7.7 Austenite lattice parameter versus temperature for different thermal-mechanical cycles.

7.1.4 Retained austenite

The BCC phase volume fraction at room temperature, and hence the retained austenite volume fraction, differs for each temperature-load history (Fig. 7.5). The retained austenite lattice parameter also shows higher levels with increasing applied load (Fig. 7.7). Extracted data on retained austenite volume fraction and the lattice parameter at room temperature after unloading are presented in Table 7.2. The fraction shows an increase with increasing applied load. The sample subjected to 400 N load contains the highest retained austenite volume fraction of approximately 7.6 %.

7.1.5 Microstructural characterization

The colour-etched microstructures of different samples are shown in Fig. 7.8. The samples are etched with LePera etchant. This etching changes the colours of retained austenite/ martensite into whitish blue, bainite into brown and ferrite into a tan colour [19, 20]. The sample subjected to a load of 50 N is almost fully martensitic (Fig. 7.8 a). By increasing the load to 100 N and ferrite decorates the prior austenite grain boundaries (Fig. 7.8 b-d). In the thermal mechanical treated sample subjected to a 400 N load, the presence of ferrite is most pronounced. Furthermore, the micrograph shows a heavily deformed microstructure (Fig. 7.8 e).

Table 7.2 Retained austenite volume percent and lattice parameter at RT for different loading conditions.

Sample	Retained austenite volume percent at room temperature (%)	Retained austenite lattice parameter (Å)
50 N	4.3	3.570
100 N	5.1	3.575
150 N	5.3	3.577
250 N	5.8	3.584
400 N	7.6	3.585
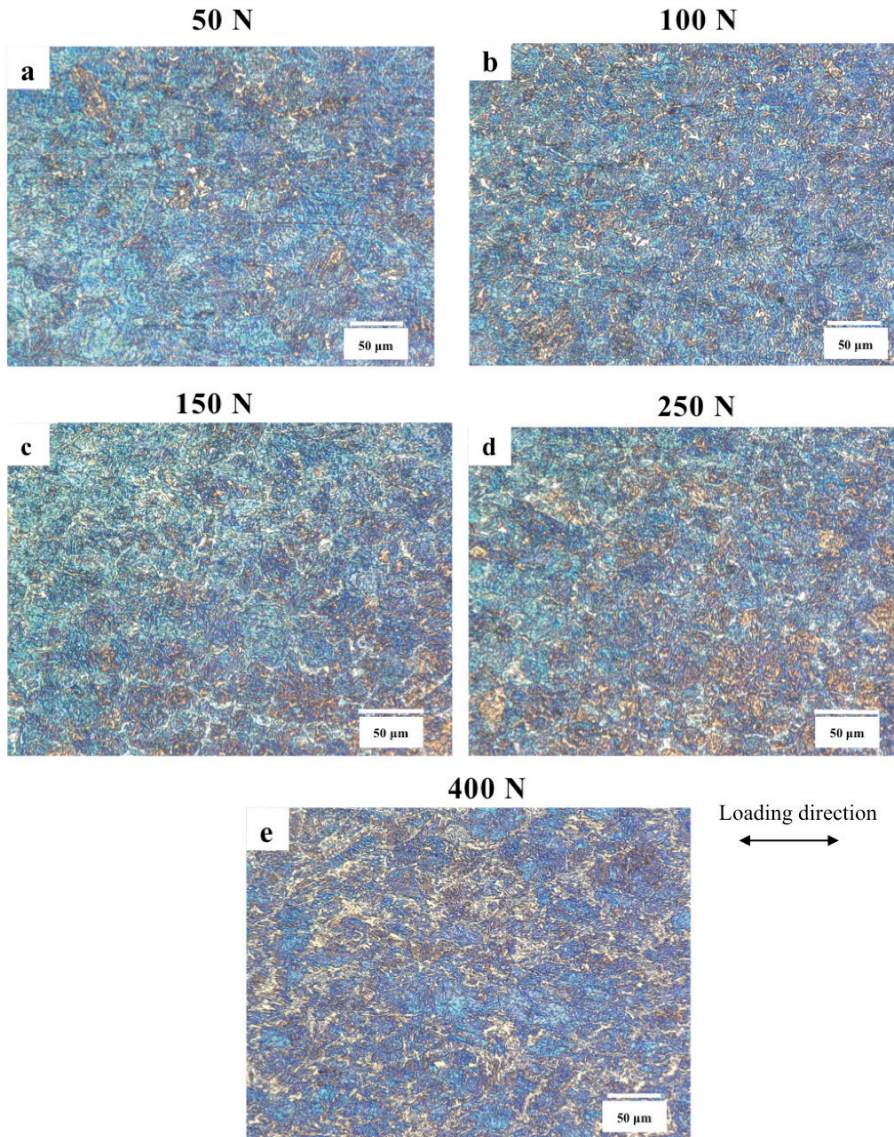
Fig. 7.8 Microstructures of samples subjected to loads of, (a) 50 N, (b) 100 N, (c) 150 N, (d) 250 N and (e) 400 N.

7.2 Discussion

In the BCC phase volume fraction diagram during the initial stage of cooling when the load is applied (Fig. 7.5), the increase in the BCC phase fraction is related to the ferrite transformation at 823 K (550 °C). From the results obtained, it can be seen that loading has a remarkable effect on the fraction of the initial BCC phase, formed isothermally. It appears that the ferrite transformation is a stress-enhanced transformation that is promoted by the increase in load (stress) at constant temperature of 823 K (550 °C). Matsuzaki *et al.* have also reported that in a FeCSiMn alloy, the bainitic ferrite transformation kinetics under isothermal condition have been accelerated by applying external loads [21]. With transformation of austenite to the BCC phase, due to the low solubility of carbon in the BCC phase, the carbon concentration of austenite increases and austenite becomes more stable. It should be mentioned that the 7 s isothermal holding is a sufficient time for carbon diffusion. In the sample subjected to 400 N, due to the formation of a large fraction of BCC phase, the austenite is expected to be more stable compared to lower loading cases. It is reported that carbon enrichment can contribute to austenite stability due to diffusion of carbon from transformed stress-induced ferritic phases into the austenite [22]. Furthermore, from the results obtained, an increase in the austenite lattice parameter under constant load at 823 K is observed (Fig. 7.7). This increase may result from two physical phenomena: The first is the effect of the mechanical elastic strain imposed on the lattice which leads to a shift in diffraction peak position and the second is a chemical contribution due to carbon-enrichment in austenite, leading to austenite stabilisation.

After the isothermal holding period of 7 s, the samples are subjected to cooling again. At a certain temperature, the volume fraction of BCC phase starts to increase steeply, indicating that martensite starts to form. For the cases that the applied load is below the yield strength of the material (50 N, 100 N and 150 N thermal-mechanical cycles), the initial BCC volume fraction is relatively low. The temperature at which the remaining austenite transforms to martensite increases when increasing the load from 50 N to100 N and 150 N. This is in agreement with the work of Dutta *et al.* [17] for loads in the elastic region. However, in samples subjected to 250 N (approximately at the yield stress) and 400 N load, a decrease in M_s is observed. Applying loads higher than the yield stress of austenite will change the austenite morphology. The austenite in the sample subjected to 400 N is elongated in the tensile loading direction and the morphology resembles a film-like austenite. This austenite morphology shows a higher stability than blocky austenite [23]. Furthermore, an increase in dislocation density of austenite associated with plastic deformation (work hardening) can also result in austenite stabilisation [24]. As mentioned before, another potentially important mechanism that can contribute

Table 7.3 Carbon content of retained austenite.

Sample	Carbon content of retained austenite (wt.%)
50 N	0.261
100 N	0.387
150 N	0.427
250 N	0.567
400 N	0.595

to austenite stability is carbon enrichment due to diffusion from transformed stress-induced ferritic phases into the austenite. The enrichment is less for small loads.

The elastic changes in the austenite lattice parameter by elastic loading can be derived from X-ray diffraction analysis. The plastic strain cannot be calculated from the X-ray data. Given that 250 N is at the elastic limit at 823 K (550 °C), the mechanical contribution on the lattice parameter change is expected to be the same in 400 N as the 250 N case. The higher ferrite transformation (higher carbon content in austenite) in the 400 N sample leads to a larger austenite lattice parameter in this sample in comparison with the 250 N sample. As the effects of mechanical loading and chemical composition (carbon content) during cooling are combined, the differentiation between these factors is not easy.

The carbon concentration of the retained austenite can be calculated from the lattice parameters of retained austenite. The carbon concentration ($C\gamma$) of retained austenite is obtained from Eq. (7.1) [25-28]:

$$a_\gamma = a_0 + k_C X_C + k_{Mn} X_{Mn} ...,$$ (Eq. 7.1)

where a_0 is the theoretical austenite lattice parameter (at 20 °C) for pure iron, being 3.556 Å [25], X_C is the concentration of carbon in wt.% and X_{Mn} is the concentration of manganese in wt.%, the coefficients k_C and k_{Mn} are determined to be 0.00453 nm/(wt.%) C and 0.000095 nm/(wt.%) Mn, respectively, as indicated in reference [25].

The calculated carbon content of retained austenite, shown in Table 7.3 is higher within the samples subjected to higher loads. The bulk carbon concentration of the steel studied is about 0.215 wt.%.

The Gibbs free energy of austenite, martensite and carbon enriched austenite are shown schematically in Fig. 7.9. Carbon enriched austenite shows a lower free energy. Austenite carbon enrichment, stabilization by plastic deformation and changes in morphology increase the yield stress of austenite, thereby retarding the martensitic transformation [24]. These mechanisms can explain the decrease in M_s for samples subjected to 250 N and 400 N loads. Comparing the two samples of 250 N and 400 N, the M_s has increased

7

with increasing load. This could be related to the limited set of data points available to determine M_s, since there is a temperature change of 28 K between consecutive data points.

The microstructures of different samples are in good agreement with the BCC phase volume fraction-temperature diagrams. As expected from the phase fraction diagram (Fig. 7.5), the 50 N sample has the highest volume fraction of martensite, and the 400 N sample, contains a high volume fraction of ferrite and a lower fraction of martensite. As shown in Fig. 7.8, the ferrite phase has decorated the prior austenite grain boundaries. The micrograph of the sample subjected to 400 N shows elongated grains, which are related to high external load applied in this sample.

The sample subjected to 400 N shows the highest retained austenite at room temperature. As reported by Xiong *et al.* [23], the stability of retained austenite is affected by the carbon content and the morphology. The increase in the retained austenite volume fraction with increased load can be related to the more stabilized austenite due to the mechanisms already discussed.

The effect of loading magnitude and carbon content of austenite on the martensitic transformations according to the results obtained in this study is summarized in Fig. 7.9. Increasing the loads below the yield stress (*i.e.* the elastic regime), increases the M_s. However, applying a load higher than the yield stress, accompanied by carbon enrichment of the austenite due to former Widmanstätten ferrite transformation, results in a decrease in M_s.

During resistance spot welding, a constant load (stress range of 100-200 MPa) is applied by the electrodes to the workpiece. During the hold time, the FCC to BCC phase transformations take place in the HAZ of resistance spot welds. These solid-state phase transformations occurring after the weld formation in the HAZ are affected by the electrode load. It should be mentioned that the electrode force on the steel sheets during spot welding is compressive, however, the material at the weld edge is under tension and the stress state is complicated (see chapter 6 for the stress state in resistance spot welding, it should be mentioned that during cooling of the HAZ, the tensile in-plane residual stresses are developed). In CR700Y980T-DH-GI resistance spot welds, the weld nugget and HAZ microstructure is fully martensitic (see section 4.1.1) due to the relatively high alloying element content of the steel and the high cooling rate during welding (with a holding time of 200 ms, the cooling rate is approximately 4000 Ks^{-1}. Therefore, the effect of electrode force on the martensitic transformation (such as M_s) is not high. However, in the welds with a multiphase HAZ microstructure; *i.e.* HSLA steel resistance spot welds, the electrode force can affect the FCC to BCC phase transformations including the martensite start temperature and the amounts of martensite and retained austenite and hence the mechanical performance of the welds.
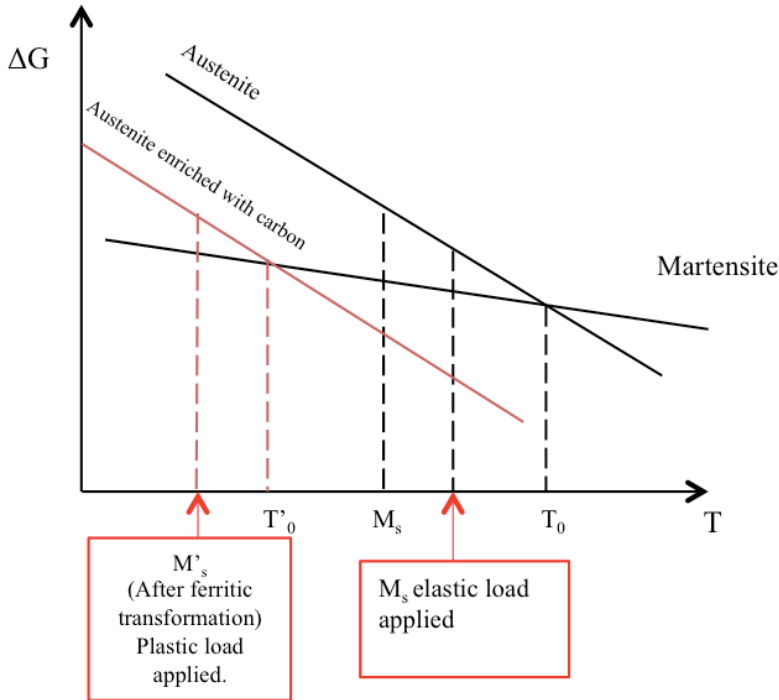
Fig. 7.9 Schematic illustration of Ms changes under different loading conditions studied in this work. Increasing the loads lower than the yield stress, increases the Ms. However, applying a load higher than yield in accompanying with carbon enrichment in austenite due to former BCC phase transformation is resulted in decrease in Ms.

7.3 Conclusions

Based on the results obtained in the current work, the following conclusions can be drawn:

1. At a constant temperature of 823 K (550 °C), applying a load increases the BCC phase volume fraction. The BCC phase volume fraction increases with increase in load.

2. Applying stresses lower than the yield stress of the material, increases M_s, conversely applying loads higher than the yield stress decreases M_s, possibly due to an increase in austenite dislocation density, change in morphology and carbon enrichment.

3. The samples subjected to higher loads show higher retained austenite volume fractions and a larger retained austenite lattice parameter as a result of changes in austenite morphology and austenite carbon enrichment.

References

[1]   Z.M. Shi, Jian Li, B. Chi, J. Pu, Y.S. Zhang, M.Q. Wang, J. Shi, H. Dong, *Martensitic Phase Transformation from Non-isothermally Deformed Austenite in High Strength Steel 22SiMn2TiB*, Metall. Mater. Trans. A 44A (2013) 4136-4142.

[2]   M. Naderi, A. Saeed-Akbari, W. Bleck, *The effects of non-isothermal deformation on martensitic transformation in 22MnB5 steel*, Mater. Sci. Eng. A 487 (2008) 445–455.

[3]   M. Naderi, A. Saeed-Akbari, W. Bleck, *Quantitative and qualitative investigation of the heterogeneous microstructures using surface hardness mapping and dilatation data*, Mater. Lett. 62 (2008) 1132–1135.

[4]   Z. Shi, K. Liu, M.Q. Wang, J. Shi, H. Dong, J. Pu, B. Chi, Y.S. Zhang, L. Jian, *Effect of non-isothermal deformation of austenite on phase transformation and microstructure of 22SiMn2TiB steel*, Mater. Sci. Eng. A 535 (2012) 290–296.

[5]   T.Y. Hsu, J. Li, Z.P. Zeng, *Metallography*, 19(3) (1986) 305–316.

[6]   T.Y. Hsu, *An approximate approach for the calculation of M_s in iron-base alloys*, J. Mater. Sci. 20 (1985) 23–31.

[7]   T.Y. Hsu, H.B. Chang, S.F. Luo, *On thermodynamic calculation of M_s and on driving force for martensitic transformations in Fe-C*, J. Mater. Sci. 18(11) (1983) 3206–3212.

[8]   M. Maalekian, E. Kozeschnik, S. Chatterjee, H.K.D.H. Bhadeshia, *Mechanical stabilisation of eutectoid steel*, Mater. Sci. Technol. 23 (2007) 610-612.

[9]   B.B. He, W. Xu, M.X. Huang, *Increase of martensite start temperature after small deformation of austenite*, Mater. Sci. Eng. A 609 (2014) 141-146.

[10]   R.K. Dutta, R.M. Huizenga, R.H. Petrov, M. Amirthalingam, A. King, H. Gao, M.J.M. Hermans, I.M. Richardson, *In-Situ Synchrotron Diffraction Studies on Transformation Strain Development in a High Strength Quenched and Tempered Structural Steel—Part I. Bainitic Transformation*, Metall. Mater. Trans. A 45(1) (2014) 218-229.

[11]   R. Blond, E. Jimenez-Melero, L. Zhao, J.P. Wright, E. Brck, S. van der Zwaag, N.H. van Dijk, *High-energy X-ray diffraction study on the temperature-dependent*

mechanical stability of retained austenite in low-alloyed TRIP steels, Acta Mater. 60(2) (2012) 565–577.

[12] R. Blond, E. Jimenez-Melero, N.H. van Dijk, E. Brck, L. Zhao, J. Sietsma, S. van der Zwaag, *Diffuse.* Defect Data Part B 172 (174) (2011) 196–201.

[13] S.E. Offerman, N.H. van Dijk, J. Sietsma, E.M. Lauridsen, L. Margulies, S. Grigull, H.F. Poulsen, S. van der Zwaag, *Phase transformations in steel studied by 3DXRD microscopy*, Nucl. Instrum. Methods Phys. Res. Sect. B 246 (1) (2006) 194–200.

[14] S.E. Offerman, N.H. van Dijk, J. Sietsma, S. Grigull, E.M. Lauridsen, L. Margulies, H.F. Poulsen, M.T. Rekveldt, S. van der Zwaag, *Grain Nucleation and Growth During Phase Transformations*, Science 298 (5595) (2002) 1003–1005.

[15] H. Dai, J.A. Francis, H.J. Stone, H.K.D.H. Bhadeshia, P.J. Withers, *Characterizing Phase Transformations and Their Effects on Ferritic Weld Residual Stresses with X-Rays and Neutrons*, Metall. Mater. Trans. A 39 (2008) 3070–3078.

[16] H.J. Stone, H.K.D.H. Bhadeshia, P.J. Withers, *In Situ Monitoring of Weld Transformations to Control Weld Residual Stresses*, Mater. Sci. Forum 571-572 (2008) 393–398.

[17] R.K. Dutta, R.M. Huizenga, R.H. Petrov, M. Amirthalingam, A. King, H. Gao, M.J.M. Hermans, I.M. Richardson, *In-Situ Synchrotron Diffraction Studies on Transformation Strain Development in a High Strength Quenched and Tempered Structural Steel—Part I. Bainitic Transformation*, Metall. Mater. Trans. A 45 (2014) 230-238.

[18] R.W. Neu, H. Sehitoglu, *Stress-induced transformation in a carburized steel—Experiments and analysis*, Acta Metall, 40(9) (1992) 2257–2268.

[19] F.S. LePera: *Metallography* 12 (1979) 263–268.

[20] A.K. De, J.G. Speer, D.K. Mattock, *Color tint-etching for multiphase steels*, Advanced Materials & Processes (2003) 27–30.

[21] A. Matsuzaki, H.K.D.H. Bhadeshia, H. Harada, *Stress affected bainitic transformation in a Fe-C-Si-Mn alloy*, Acta Metal. Mater. 42(4) (1994) 1081-1090.

7

[22] T.Y. Hsu, Li Xuemin, *Diffusion of carbon during the formation of low-carbon martensite*, Scr. Metall. 17 (1983) 1285-1288.

[23] X.C. Xiong, B. Chen, M.X. Huang, J.F. Wang, L. Wang, *The effect of morphology on the stability of retained austenite in a quenched and partitioned steel*, Scr. Mater. 68(5) (2013) 321–324.

[24] Z.M. Shi, J. Li, B. Chi, J. Pu, Y.S. Zhang, M.Q. Wang, J. Shi, H. Dong, *Martensitic Phase Transformation from Non-isothermally Deformed Austenite in High Strength Steel 22SiMn2TiB*, Metall. Mater. Trans. A 44(9) (2013) 4136-4142.

[25] N.H. van Dijk, A.M. Butt, L. Zhao, J. Sietsma, S.E. Offerman, J.P. Wright, S. van der Zwaag, *Thermal stability of retained austenite in TRIP steels studied by synchrotron X-ray diffraction during cooling*, Acta Mater. 53(20) (2005) 5439–5447.

[26] C.P. Scott, J. Drillet, *A study of the carbon distribution in retained austenite*, Scr. Mater. 56(6) (2007) 489-492.

[27] M.X. Zhang, P.M. Kelly, *Determination of Carbon Content in Bainitic Ferrite and Carbon Distribution in Austenite by Using CBKLDP*, Mater. Charact. 40(3) (1998) 159–168.

[28] N. Ridley, H. Stuart, L. Zwell, *Lattice parameters of Fe-C austenite at room temperature*, Trans. Metall. Soc. AIME 245 (1969) 1834-1836.

7
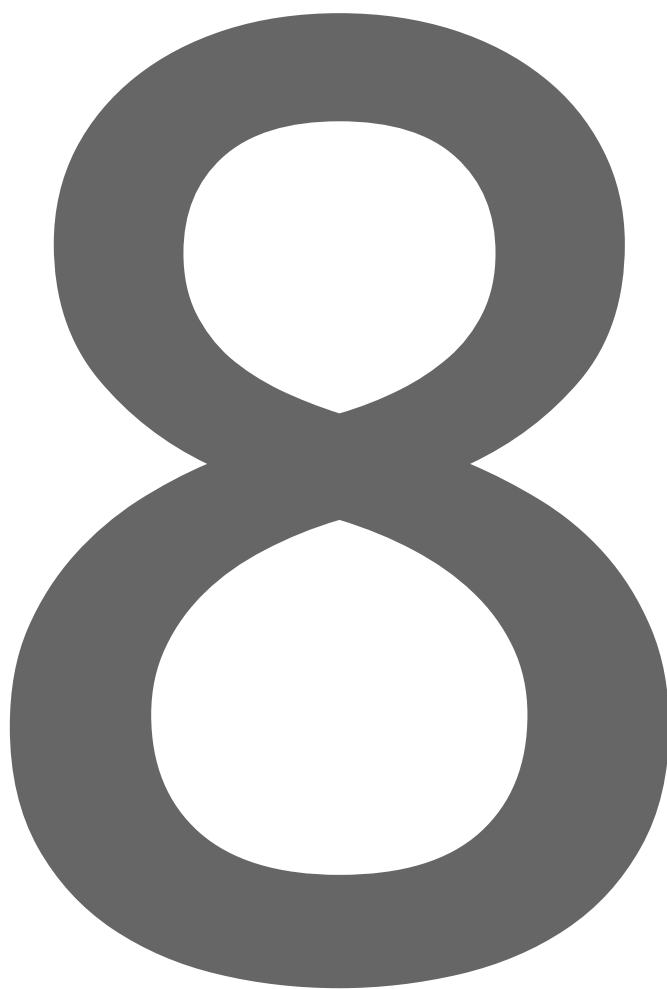
CHAPTER 8

General Discussion

In this chapter, the information already given in the previous chapters are combined to draw together the most important aspects of this research.

The favourable combination of strength and formability of advanced high strength steels (AHSS) makes them ideal for automotive applications, in particular to produce lightweight vehicles with low carbon emissions, without compromising safety standards [1]. These mechanical properties are the result of carefully designed multiphase microstructures, which are obtained by adding alloying elements and by the application of designed heat treatments. However, higher alloying contents and new coating technologies have led to challenges regarding the resistance spot welding (RSW) of these steels. As mentioned in section 2.5, the unacceptable failure behaviour and the reduction in mechanical strength of spot welds are important issues. The cross tension strength test performance of the AHSS resistance spot welds is inferior to that of conventional mild steels (see Fig. 2.13). The aim of this study is to come to a better understanding of the microstructural evolution and the relationship between microstructure and mechanical response in order to improve this failure behaviour.

Three major factors contributing to the mechanical response of resistance spot welds are the welding conditions imposed on the material, the characteristics of the material to be welded and the residual stresses; as shown in Fig. 8.1.

Welding process conditions include mechanical loading due to the applied electrode force, the welding current and time, the holding time and the heating and cooling rates. In addition, the electrode material, the electrode shape and the effectiveness of the water-cooling, *i.e.* the electrode surface temperature, are also contributing factors [3,4]. The welding current, welding time and electrode force must be such that a sufficiently large weld nugget is formed (see section 2.2).

The material related factors consist of chemical composition, type and fractions of phases, grain size, inclusions, texture, crystallographic orientation and thickness of the sheet and coating. As discussed in section 3.2, the materials studied are advanced high strength steels (AHSS) delivered by Tata Steel Europe. The work focuses on a 3rd generation 1 GPa AHSS CR700Y980T-DH-GI, received in a cold-rolled and galvanised condition with a thickness of 1.3 mm.

The thermal-mechanical cycle in resistance spot welding destroys the designed multiphase microstructure of the AHSS and results in a chemically and mechanically heterogeneous solidification microstructure in the weld nugget. Solidification that takes place during cooling results in a columnar solidification microstructure with grains oriented along the maximum temperature gradient, see Fig. 2.8. The solidification results in a fully martensitic microstructure due to relatively high carbon equivalent of the steel and high cooling rates during resistance spot welding (see section 4.1.1.1). The solidification is also accompanied by micro-segregation of alloying elements due to high cooling rates.
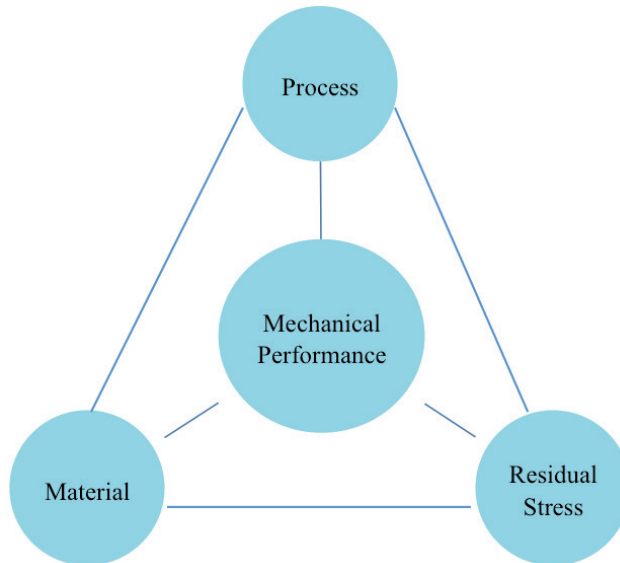
Fig. 8.1 Interaction of factors involving in mechanical performance of resistance spot welds.

During welding, the imposed thermal-mechanical cycle alters the microstructure in the heat affected zone (HAZ) around the weld and during cooling, solid-state phase transformations occur. The microstructure of the HAZ of the welds studied is also predominantly martensitic (see section 4.1.1.1).

Another factor affecting the mechanical response of the resistance spot welds is the residual stress distribution. In resistance spot welding, the mechanical and thermal constraints due to the electrode force in combination with a local high heating and cooling rate introduce residual stresses within a resistance spot weld, which influence the mechanical performance of the welds. The residual stresses are measured using synchrotron X-ray diffraction and a finite element model using Simufact was constructed and validated by the measured data. Furthermore, the novel FIB ring-core milling technique was used to measure the micro-residual strain at the weld edge of a resistance spot weld (see section 6.1.4).

First of all, the temperature distribution for a single pulse weld obtained from SORPAS and Simufact was studied. Both models can predict the weld nugget size. However, the super heating for the weld centre cannot be predicted using SORPAS due to its limitations in determining liquid metal temperature. In Simufact, the temperature at the centre reaches a peak temperature of about 3374 K, which is more realistic. This is the reason for calculating the stresses via Simufact.

The results show the in-plane residual stress components (σ_x and σ_z) are tensile within the weld nugget of the resistance spot weld and this is attributed to solidification shrinkage
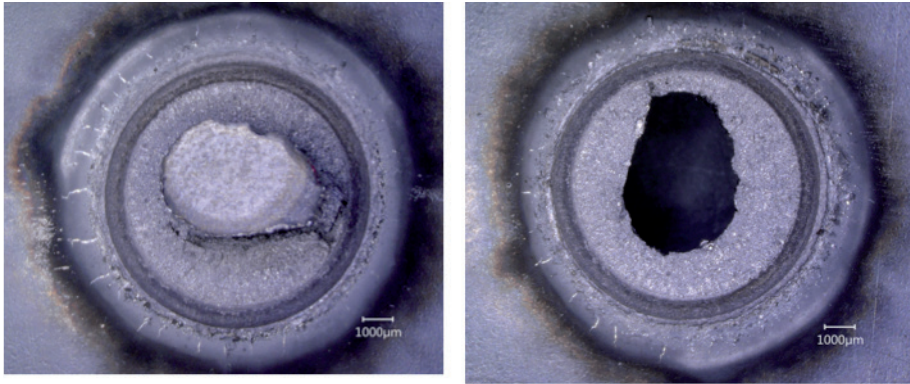
Fig. 8.2 Representative failure mode of an AHSS resistance spot weld for cross tension strength testing, showing partial interfacial failure.

of the molten nugget and thermal contraction during cooling to room temperature. The HAZ also exhibits tensile in-plane stress components due to the thermal contraction. To maintain equilibrium in the work piece, the base material shows compressive residual stresses near the weld.

The mechanical response of the welds is evaluated with microhardness measurement, cross tension strength (CTS) and tensile shear strength (TSS) testing of the welds. The failure modes obtained from CTS and TSS tests determine assessment of the quality of the spot welds. Furthermore, the fracture toughness of the simulated HAZ microstructures has also been investigated.

Fracture toughness of a material indicates the ability of the material to resist the crack propagation. Due to the low fracture toughness of the martensitic weld nugget and the phosphorous enrichment at the dendritic boundaries [5], a crack can easily propagate through the weld nugget resulting in weld metal failure, which is an unfavourable failure mode during cross tension strength (CTS) testing [6, 7]. During the CTS testing of the welds, the crack propagates through the weld nugget zone resulting in interfacial or partial plug failure, with low load bearing capacity and displacement (Fig. 4.13 and Table 4.4, see sequence 1). A representative failure mode of a single pulse weld cross tension strength test is shown in Fig. 8.2, indicating a partial interfacial failure (PIF). The loading condition during the CTS testing is most severe at the weld edge (weld notch). To improve the mechanical performance, strategies to strengthen this area are required.

8.1 Strategies to obtain safe microstructures in AHSS resistance spot welds

Application of a heat treatment after welding (postweld heat treatment) is intended primarily as a stress-relief treatment to improve the mechanical response of the welds

and such treatments have already been applied for decades [8-10]. The postweld heat treatment procedure has to be designed for each specific case depending upon the material properties and the welding technique. In this study, a strategy is applied to improve the microstructure of the weld edge as well as the residual stress distribution in the weld nugget with application of a second current pulse. Furthermore, the application of a typical paint bake cycle is also considered as a heat treatment to improve the mechanical response of the welds.

8.1.1 Double pulse welding

A strategy to modify the microstructures of resistance spot welds is to apply a second current pulse (chapter 4). The effect of the second current pulse on the microstructure is governed by the current level, the time over which the current is applied, the cooling time between current pulses and the cooling rate.

As mentioned before, in a resistance spot weld, the weld nugget is dendritic with martensitic microstructure and the alloying elements are segregated at the dendrite boundaries. When applying a second current pulse with the current amplitude lower than the first current pulse (sequence 2) or an equal weld current amplitude (sequence 3), a second weld nugget somewhat smaller than the primary weld nugget is formed (less heat is generated as the interface resistant is lower). However, numerical calculation and microstructural evaluation confirm that the microstructure of the weld edge remains austenitic and nucleation and grain growth occur during the second pulse. Recrystallisation and grain growth take place at the weld edge as a result of high temperature and the plastic deformation induced by electrodes. Therefore, the microstructure at the weld edge is modified and equai-axed grains are formed. It should be mentioned that the microstructure is still martensitic at the weld edge, in the weld nugget and in the HAZ. Moreover, in the double pulse welds (sequence 2 and 3), redistribution of phosphorous, manganese and silicon takes place during the second current pulse. As sequence 3 experiences the highest peak temperature during the second pulse, the redistribution of phosphorous in this weld is most pronounced (Fig. 4.5 c to 4.7 c). During the second current pulse at the weld edge of the sequence 3, where the temperature is about 1760 K for 25 ms, phosphorous can diffuse about 30 μm (see section 4.1.2). An overview of the effects of double pulse welding on the microstructure and the mechanical performance of the welds is shown in Fig. 8.3.

The mechanical testing of welds shows that sequence 3 has the highest CTS and a favourable failure mode. The presence of equi-axed grains instead of dendritic grains at the weld edge affects the crack path during peel loading (CTS testing) (Fig. 4.15). It appears that the fracture path always follows prior austenite grain boundaries, where the phosphorous is segregated. Therefore, the phosphorous distribution plays a dominant role in the mechanical properties of the welds examined. The higher maximum load bearing
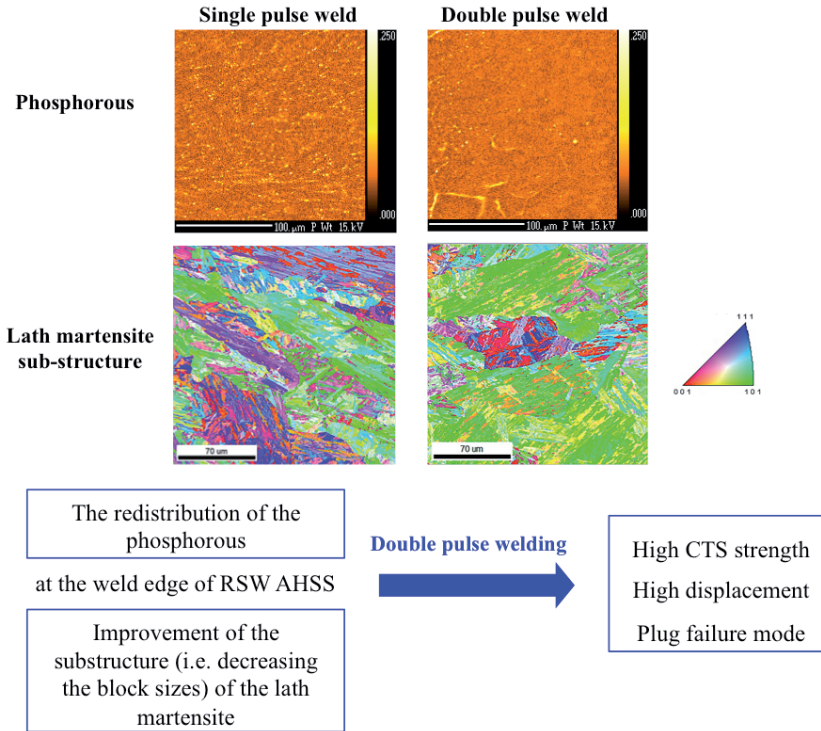
Fig. 8.3 Overview of the effect of double pulse welding on the microstructure and the mechanical response of the resistance spot welds (See chapter 4).

capacity and larger displacements during CTS testing of a double pulse weld indicates a higher energy absorption during peel loading, *i.e.* an increased crashworthiness [11]. Moreover, the measured and simulated residual stress of the single and double pulse welds (sequence 1 and 3, respectively) shows that the in-plane tensile residual stress at the weld nugget of a double pulse weld is lower in magnitude than a single pulse weld (see section 6.1.2). The smaller solidified dendritic weld nugget (secondary weld nugget) of a double pulse weld compared to a single pulse weld (primary weld nugget) is the reason for the stress reduction. This reduction contributes to the improved mechanical performance of the welds during tensile shear strength (TSS) loading. The results of TSS testing of double pulse welds show higher maximum load and displacement (Table 6.1). During TSS testing, the shear loading (mode II loading) is applied to the weld and the in-plane residual stress components at the weld edge play a role in the response of the material to the shear loading (see section 6.2); the lower the tensile in-plane residual stress components, the higher the shear load bearing capacity.

8.1.1.1 Simulated residual stress and correlation with CTS results

Synchrotron X-ray experiments allow measurement of the x and z-component of residual stress (σ_x and σ_z). Measurement of the residual stress perpendicular to the plane was not feasible using the available 70 keV as the X-ray beam should pass through the length of the resistance spot weld plate and the collected peak intensity will not be large enough to provide any relevant data. Moreover, the residual stress measurement is time-consuming and difficult due to the small nugget size and the presence of the notch at the weld edge. The FE-based thermal-mechanical model constructed using Simufact and validated with experimental results in section 6.1.2 provides a prediction of the y-component of residual stress (through thickness of the plate) for single and double pulse welds, sequence 1 and 3 respectively, and results are shown in Fig. 8.5. The residual stress profile of a single pulse weld (Fig. 8.5 a) at the weld nugget centre shows a tensile value of about 200 MPa while in front of the weld notch, a compressive stress of about -160 MPa develops. The simulated y-component of stress for the double pulse weld shows lower residual stress values at the weld centre in comparison with the single pulse weld, around 180 MPa and the compressive residual stress is about -60 MPa at the weld edge.

Lloyd [12] has reported that the crack growth rate is affected by the residual stresses normal to the crack plane during mode I loading, *i.e.* CTS testing of the resistance spot welds (Fig. 8.4). The CTS test results in section 4.1.1.4 revealed that the double pulse welds (sequence 3) have a higher cross tension strength and displacement than a single pulse welds (sequence 1). Indeed, during the CTS testing of a single pulse weld, the high elemental segregation and dendritic structure in front of the notch contribute to the initiation of the crack through the weld metal and at the later stage the high tensile y-component of residual stress at the weld nugget centre facilitates the propagation of the crack within the weld, resulting in interfacial failure. However, in a double pulse weld, the elemental redistribution and the microstructural changes in front of the weld notch due to the double pulsing changes the crack initiation and propagation direction and results in a plug failure mode. The low tensile y-component of residual stress at the weld centre also contributes to an increase in the load bearing capacity of the weld. Therefore, not only the elemental segregation and microstructural changes at the weld edge but also the decrease in tensile residual stress at the weld centre of the double pulse welds can contribute to higher load bearing capacity and improve the CTS performance of these welds.

Chabok *et al.* [13] measured the residual stress normal to the plane of the notch at the weld edge of the spot weld using a slit milling DIC technique. There is a good agreement between the results of our model and the reported measurements by Chabok *et al.* [13] on the residual stress nature in the through thickness direction at the weld edge. The results show that the nature of this residual stress component is compressive at the weld edge.
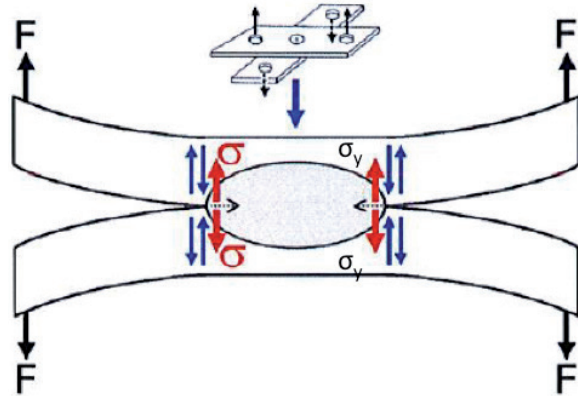
Fig. 8.4 A schematic representation of a cross tension strength sample under loading.
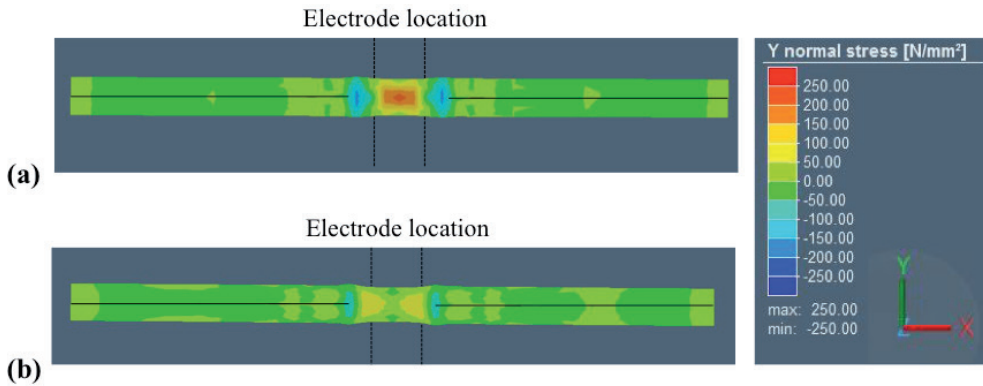
Fig. 8.5 Simulated y-component of residual stress at the cross-section view of (a) single pulse and (b) double pulse weld.

8.1.2 Effect of paint bake cycle

In the automotive industry, after assembly, the body-in-white is subjected to a paint bake cycle that typically subjects the painted material to a temperature of about 180 °C for 20 min. Further improvement in microstructure and thereby mechanical performance of the resistance spot welds was obtained by application of a paint bake cycle after welding (chapter 5). This low temperature post weld heat treatment results in tempering of the martensite with precipitation of ε-carbide within the weld nugget and the HAZ, which was detected using transmission electron microscopy. It has been reported that the presence of ε-carbide in martensite is associated with preferable mechanical properties, including high strength and toughness [14]. This precipitation leads to higher maximum load and an increased displacement in CTS testing of the welds.

The strength improvement mechanism with ε-carbide formation is precipitation strengthening, $\sigma_{pcpt}^{\varepsilon}$ (MPa), which is expressed by Eq. 8.1 [15]:

$$\sigma_{pcpt}^{\varepsilon} = \left(\frac{13320\sqrt{f_{\varepsilon}}}{d_{\varepsilon}\left(\sqrt{\pi} - 2\sqrt{f_{\varepsilon}}\right)}\right) \ln\left(\frac{d_{\varepsilon}}{0.496}\right),$$ (Eq. 8.1)

where f_{ε} is the volume fraction of the ε-carbide and d_{ε} (nm) is the diameter of the ε-carbide.

Considering the d_{ε} to be about 15 nm and f_{ε} to be about 0.04 in the paint-baked sample from Fig. 5.7, the calculated $\sigma_{pcpt}^{\varepsilon}$ is about 400 MPa. It should be mentioned that the statistics are not considered in this calculation and the purpose is to estimate the order of magnitude of the contribution of the ε-carbide to strengthening of the welds. Thus, the ε-carbide formation can considerably improve the strength of the welds. However, calculation of the strength improvement due to the ε-carbide formation from CTS testing results is not possible as the load-displacement curves also include contributions from the base material deformation.

The pop-ins in the load versus displacement curves obtained from CTS testing mean that the load bearing suddenly decreases and this corresponds to quick propagation of a crack, which is rapidly arrested [16]. The pop-ins occur at higher displacements for the paint baked samples, indicating that the fracture toughness of the welds is increased. It means that the ability of the weld to resist the fracture is increased. A series of experiments were designed to compare the fracture toughness of the martensitic microstructure (simulated to be similar to the coarse grained HAZ of the as-welded sample) and paint baked microstructure, *i.e.* tempered martensite (simulated to be similar to the coarse grained HAZ of a weld subjected to baking cycle after welding). The results show that the fracture toughness, *i.e.* crack tip the paint-baked sample is about 0.16 mm relatively larger than that of the martensitic sample.

The residual stress measurement of the welds and paint baked welds reveal that the welds subjected to the paint bake cycle show lower in-plane tensile residual stress levels at the weld edge in comparison with welds not subjected to this bake cycle (section 6.1.3). Brown *et al.* [17] have reported that in steels with carbon content of 0.45-0.95 (wt.%), internal stresses generated on quenching are partly relaxed by allowing carbon to diffuse during tempering but an enhanced relaxation is associated with ε-carbide, which preferentially grows on planes that minimize the mismatch with the matrix and surface energies. More relaxation occurs when a plastic zone, caused by the volumetric change during precipitation is generated around ε-carbide [18]. The decrease in residual stress of a weld after a paint bake cycle therefore can be attributed to the stress relaxation during ε-carbide formation.

The lower tensile residual stress of the paint-baked welds contributes in increased load bearing during the TSS testing of the welds. During TSS testing, a shear loading is applied and thus the in-plane residual stresses play a role in the crack initiation.

It should be mentioned that the retained austenite volume fraction has not changed appreciably due to the paint bake cycle. The only observed microstructural evolution

8

is precipitation of ε-carbide. Particularly, the Al and Si content of this steel provide the possibility of precipitation of ε-carbide during tempering of the martensite subjected to the low temperature post weld heat treatment [18].

There is limited information available in the literature on the thermodynamics of ε-carbide formation, but kinetic data accumulated during tempering studies have led to an estimation of the formation energy. Jang *et al.* [19] have reported calculations to estimate various thermodynamic parameters for iron carbides. The energy of ε-carbide formation was calculated to be 106 kJ/mol. Models that simulate the ε-carbide precipitation generally consist of random nucleation of a seed, growth of a stable particle by diffusion of atoms through the matrix followed by coarsening [20-21].

The optimised double pulse welding condition for the CR700Y980T-DH-GI steel involves application of the highest acceptable first current pulse to obtain the largest acceptable weld nugget size. Then, a second current pulse is applied equal to the first current pulse to anneal the weld edge without melting it, resulting in a reduction of the alloying element segregation at the weld edge and consequent grain size and morphology modification. Application of a typical paint bake cycle (heat treatment at 180°C for 20 min) after welding allows further improvement of the microstructure by precipitation of the ε-carbide. Therefore, the application of a double pulse resistance spot weld combined with a typical paint bake cycle allows microstructural modification resulting in an improved mechanical response of the spot welds.

8.2 Comments on the residual stress measurement and simulation

The errors in the residual stress measurement are related to several factors. These can be divided into errors from the X-ray source, the sample and the data processing. The errors from the X-ray source can be wavelength variations. The error from the sample positioning is about ±0.1 mm (shown as error bars in the x-direction Fig. 6.1). This error is obtained from a comparison of the data points and the optical micrographs of the cross-sections of the welds. The errors originating from the sample include grain statistics and texture. The errors from the data analysis can come from the choice of elastic constants, diffraction peak fitting and stress free lattice parameter determination. It is quite important to have an accurate knowledge of the stress free lattice spacing to determine the stress using the strain scanning methods. The stress free lattice spacing is measured separately from the stress free samples for the weld nugget zone, HAZ and the base material (section 3.4.2) as the variation in composition and the microstructure can affect the stress free lattice spacing value.

It should be mentioned that the diffraction peak quality is lower in the weld nugget zone than in the base material due to the dendritic structure of the weld nugget. However,

the base material has a fine-grained equiaxed microstructure and the diffraction peak quality is high. Thus, the errors originating from the diffraction peak fitting to determine the lattice spacing and the residual strain/stress are higher in the weld nugget zone than the base material (indicated as error bars in the y-direction in Fig. 6.1).

The uncertainties in the residual stress simulation come from the temperature dependant material properties, the assumption of the node constraints in the model, the finite element model limitation in the simulation of microstructural changes such as grain refinement and redistribution of alloying elements during double pulse welding and the ε-carbide precipitation during martensite tempering with application of the paint bake thermal cycle. Nevertheless, a good match was obtained between the residual stresses obtained from the models and the measurements.

8

References

[1]   N. Baluch, Z.M. Udin, C.S. Abdullah, *Advanced high strength steel in auto industry: an overview*, Eng. Tech. Appl. Sci. Res. 4 (2004) 686–689.

[2]   S. Furusako, G. Murayama, H. Oikawa, T. Nose, F. Watanabe, H. Hamatani, Y. Takahashi, *Current Problems and the Answer Techniques in Welding Technique of Auto Bodies (First Part)* - Nippon Steel Technical Report, 103 (2013) 69-75.

[3]   ANSI/AWS/SAE D8.9-97, *Recommended practices for test methods and evaluation the resistance spot welding behavior of automotive sheet steels* (1997).

[4]   SEP 1220-2: *'Testing and documentation guideline for the joinability of thin sheet of steel-part 2: resistance spot welding'*, Technical report 08, VDEh standard (2007).

[5]   M. Amirthalingam, E.M. van der Aa, C. Kwakernaak, M.J.M. Hermans, I.M. Richardson, *Elemental segregation during resistance spot welding of boron containing advanced high strength steels*, Weld. World. 59 (2015) 743–755.

[6]   S. Dancette, D. Fabregue, V. Massardier, J. Merlin, T. Dupuy, M. Bouzekri, *Experimental and modeling investigation of the failure resistance of advanced high strength steels spot welds*, Eng. Fract. Mech. 78(10) (2011) 2259–2272.

[7]   C. Sawanishi, T. Ogura, K. Taniguchi, R. Ikeda, K. Oi, K. Yasuda, A. Hirose, *Mechanical properties and microstructures of resistance spot welded DP980 steel joints using pulsed current pattern*, Sci. Technol. Weld. Join. 19(1) (2014) 52–59.

[8]   R.S. Parmer, *Welding Engineering and Technology*, Khanna publishers, second edition, ISBN: 81-7409-028-2 (2010).

[9]   A.G. Olabi, M.S.J. Hashemi, *The effect of post-weld heat-treatment on mechanical-properties and residual-stresses mapping in welded structural steel*, J. Mater. Proces. Technol. 55 (1995) 117-122.

[10]   V.S. Raghunathan, V. Seetharaman, S. Venkadesan, P. Rodriguez, *The influence of post weld heat treatments on the structure, composition and the amount of ferrite in type 316 stainless steel welds*, Metall. Trans. A 10(11) (1979) 1683-1689.

[11]   M. Pouranvari, S.P.H. Marashi, *Critical review of automotive steels spot welding: process, structure and properties*, Sci. Technol. Weld. Join. 18 (2013) 361–403.

[12]   J.R. Lloyd, *The effect of residual stress and crack closure on fatigue crack growth*, Doctor of Philosophy thesis. In Department of materials engineering. University of Wollongong (1999).

[13]   A. Chabok, E. van der Aa, I. Basu, J. De Hosson, Y. Pei, *Effect of pulse scheme on the microstructural evolution, residual stress state and mechanical performance of resistance spot welded DP1000-GI steel*, Sci. Technol. Weld. Join. 23(8) (2018) 649–658.

[14]   S.A.J. Forsik, P.E.J. Rivera-Diaz-del-Castillo, *Martensitic steels: Epsilon carbides in tempered, Encyclopedia of Iron, Steel and Their Alloys* (2015) 2169-2181.

[15]   S. Maropoulos, J. D. H. Paul, N. Ridley, *Microstructure–property relationships in tempered low alloy Cr–Mo–3.5Ni–V steel*, Mater. Sci. Technol. 9 (1993) 1014-1020.

[16]   F. Krajcarz, A.F. Gourgues-Lorenzon, E. Lucas, A. Pineau. *Fracture toughness of the molten zone of resistance spot weld.* International Journal of Fracture, Springer Verlag, 181 (2013) 209-226.

[17]   R.L. Brown, H.J. Rack, M. Cohen, *Stress relaxation during the tempering of hardened steel*, Mater. Sci. Eng. 21 (C) (1975) 25–34.

[18]   S. Murphy, A. Whiteman, *The precipitation of epsilon carbide in twinned martensite*, Metall. Mater. Trans. 1(4) B (1970) 843–848.

[19]   J.H. Jang, I.G. Kim, H.K.D.H. Bhadeshia, ε-*Carbide in alloy steels: First-principles assessment*, Scr. Mater. 63(1) (2010) 121–123.

[20]   H.K.D.H. Bhadeshia, *Advances in the kinetic theory of carbide precipitation*, Mater. Sci. Forum (2003) 426–432, 35–42.

[21]   N. Fujita, H.K.D.H. Bhadeshia, *Modelling simultaneous alloy carbide sequence in power plant steels*, ISIJ Int. 42 (2002) 760–767.

8

CHAPTER 9

Conclusions and recommendations for future research

9.1 General Conclusions

The mechanical performance of resistance spot welded advanced high strength steel (AHSS) is a crucial issue in the automotive industry. The relatively high alloying element content of AHSSs and ultra fast cooling rates during the resistance spot welding result in a fully martensitic weld nugget microstructure. During mechanical testing of these welds, cracks easily propagate within the brittle weld metal and result in weld metal failure (interfacial failure), which is not a favourable failure mode. Improving the microstructure of the welds results in the improvement of mechanical performance of these welds. In this thesis, strategies such as double pulse welding and application of a paint bake cycle are discussed to improve the microstructure and mechanical response of the resistance spot welded AHSS. Based on the work in this thesis, the following conclusions are drawn:

- The redistribution of the alloying elements (*i.e.* phosphorous) and the improvement of the substructure (*i.e.* decreasing the block sizes) of the lath martensite at the weld edge of a resistance spot weld subjected to a double pulse welding scheme are the determining factors in the mechanical response of the CR700Y980T-DH-GI welds.
- Double pulse welding reduces the elemental segregation of alloying elements such as phosphorous with redistribution of the element during the second current pulse and decreases the average prior austenite grain size and the block width at the primary weld nugget edge. The ellipticity of prior austenite grains at the primary weld nugget edge decreases during the second current pulse and the elongated grains become more equi-axed.
- A typical paint baking cycle significantly increased the cross tension strength and energy absorption capability of both single and double pulse resistance spot welded CR700Y980T-DH-GI steel. Precipitation of ε-carbides and an increase in the fracture toughness of the martensite after the paint baking cycle are thought to be the dominant factors in improved cross tension strength properties of the welds.
- The experimental and simulated results show a tensile in-plane residual stress in the weld nugget due to the molten nugget solidification shrinkage and thermal contraction at the end of the weld cycle. The HAZ also exhibits a tensile in-plane stress due to the contraction during cooling. The base material shows compressive in-plane residual stresses near the weld to maintain stress equilibrium in the work piece.
- The in-plane residual stresses of a double pulse weld are lower than a single pulse weld in the weld nugget, the HAZ and the base material. This is attributed the smaller weld nugget zone of a double pulse weld and the microstructural changes during the second current pulse.

- In double pulse welding of CR700Y980T-DH-GI steel, during the cooling time between two current pulses, liquid metal is continuously present and by application of the second pulse the size of the weld pool increases, however, it is smaller than the primary weld nugget. This conclusion can only be obtained from the simulations, as temperature measurement during resistance spot welding were not possible.
- The investigation of the effect of mechanical loading on the solid-state phase transformation show that applying a load at a constant temperature of 823 K (higher than M_s), increases the BCC phase volume fraction. The BCC phase volume fraction increases with an increase in load. Furthermore, applying stresses lower than the yield stress of the material, increases M_s, conversely applying loads higher than the yield stress decreases M_s, possibly due to an increase in austenite dislocation density, change in morphology and carbon enrichment.
- The application of the mechanical load before and during the martensitic transformation could help to increase the retained austenite volume fraction in the final microstructure.

9.2 Recommendations for future research

The following suggestions are given for future research:
- It was found that the alloying elements such as phosphorous play a major role in the mechanical performance of the resistance spot welds. The decrease in phosphorus content of the initial material is expected to result in improved mechanical properties of the spot welded AHSS. A study of steels with different phosphorous content will help to better understand the limits for phosphorous content in the steels to obtain a safe microstructure in AHSS resistance spot welds.
- The measurement of the hydrogen content of resistance spot welds before and after the application of the paint bake cycle will reveal useful information regarding the contribution of hydrogen to the fracture of the welds.
- In the current research, the residual stress within a resistance spot weld subjected to a paint bake cycle was measured. The modeling of the ε-carbide formation due to the application of a paint bake cycle on the residual stress of the resistance spot welds will help to better understand the mechanisms involved. The thermodynamics and kinetics of ε-carbide formation can be studied using phase field modeling and high energy X-ray diffraction.
- The effect of tensile mechanical loading on the phase transformation of the AHSS using synchrotron X-ray diffraction was studied. Investigating the effect of compressive mechanical loading will be more relevant to the effect of electrode force during spot welding.

Appendix

Temperature dependent material properties
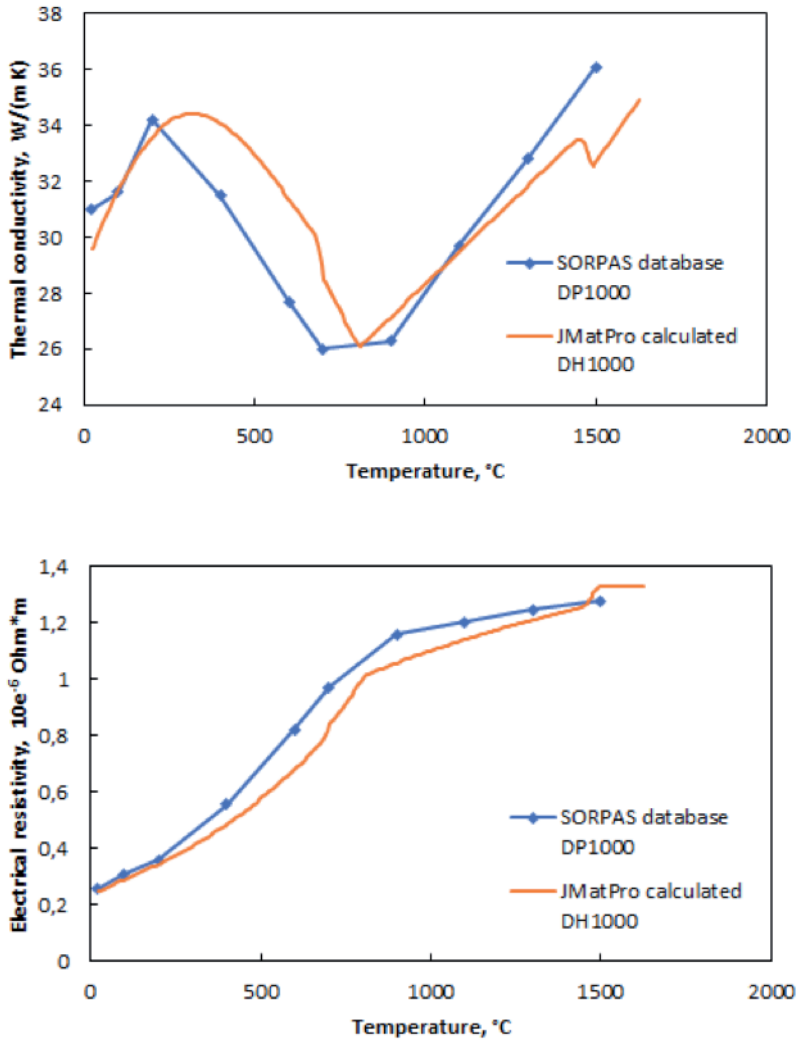
Fig. A.1 Comparison of the temperature dependant material properties (a) thermal conductivity and (b) electrical resistivity extracted from JMatPro and SORPAS.
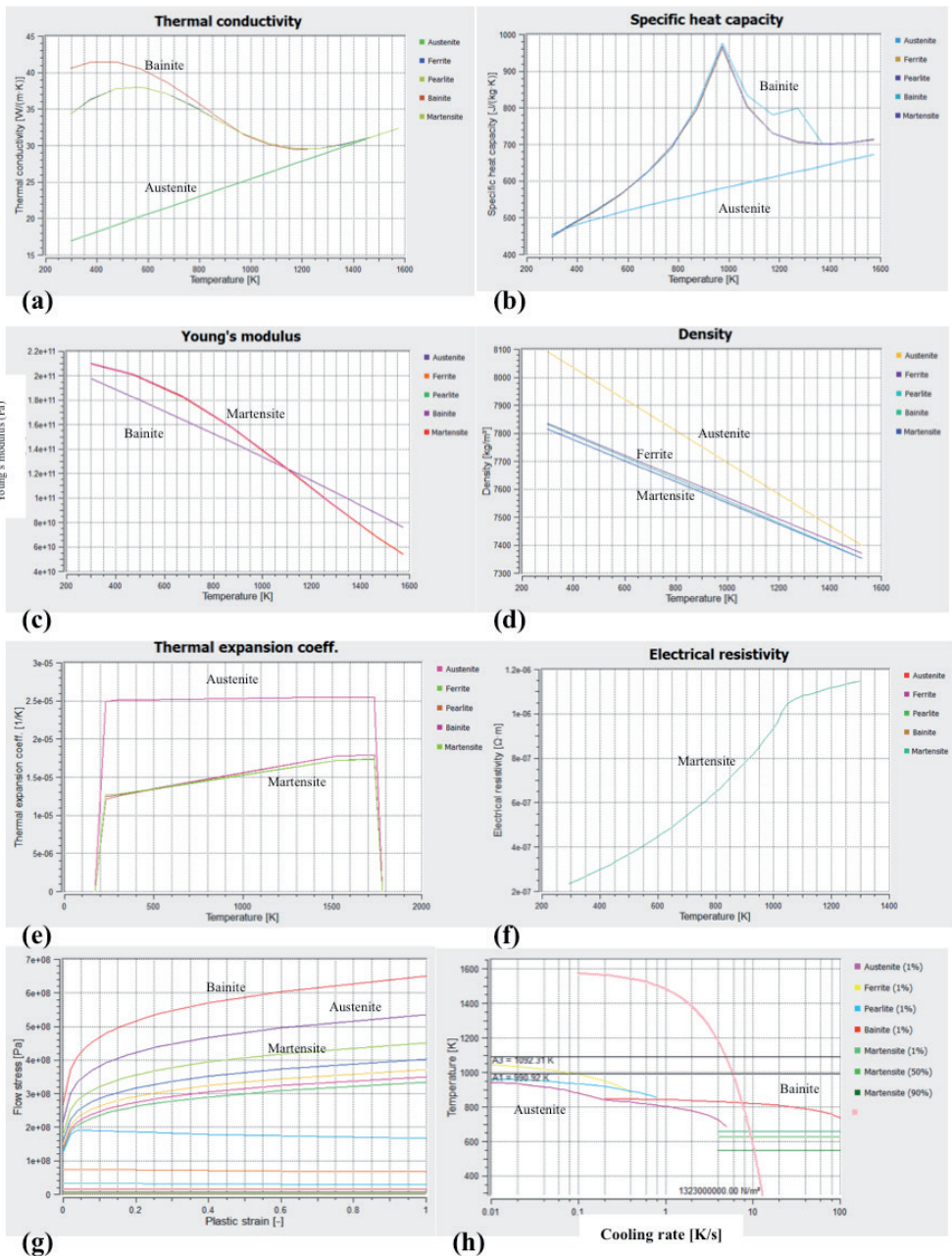
Fig. A.2 Temperature dependent material properties, (a) thermal conductivity, (b) specific heat capacity, (c) Young's modulus, (d) density, (e) thermal expansion coefficient, (f) electrical resistivity, (g) flow stress and (h) phase diagram (the pink line indicates a cooling rate of 100 Ks-1) [17].

Summary

The potential for weight reduction, ease of manufacturing and improved crashworthiness makes advanced and ultra high strength steels attractive for automotive applications. Resistance spot welding is by far the most widely used joining method in the automotive industry due to the high operating speeds, the reliability of the process and the suitability for automation. Safe microstructures in resistance spot welds in AHSS and UHSS have to be assured to promote acceptance of these steels in the automotive industry. However, the higher alloying contents of AHSS/UHSS steels limit their weldability and unfavourable modes of weld failure are frequently observed.

The main aim of this research is to identify and understand the unfavourable failure of the AHSS welds and to modify the microstructure and thus the mechanical response of the welds. In this PhD thesis the results of alternative welding schedules to modify the microstructure and mechanical performance of the AHSS resistance spot welds are reported. The effects of a paint bake cycle on the microstructure of the welds have also been investigated and the predominant mechanisms involved were studied. The residual stress within these welds were measured and simulated to facilitate the residual stress prediction before welding.

Double pulse resistance spot welding with different second pulse current levels was applied to improve the microstructure of the weld edge. The second current pulse equal to the first pulse anneals the weld edge and modifies the weld edge microstructure. Microstructural analysis was performed using optical microscopy, scanning electron microscope, electron probe microanalysis (EPMA) and electron back scattered diffraction (EBSD). The double pulse weld showed a reduction in segregation of alloying elements such as phosphorous and a change in grain morphology from dendritic to a more equi-axed shape and smaller grain size. The results obtained from the mechanical testing *i.e.* cross tension strength test (CTS) and tensile shear strength test (TSS) showed enhanced cross-tension strength and energy absorption capability of the weld for the double pulse welds.

The effect of typical paint bake cycle on the microstructure and mechanical response of the single pulse and double pulse welds after welding was investigated. A typical paint bake cycle consists of a heat treatment at about 180°C for 20 min. The microstructural studies at the weld edge using transmission electron microscopy (TEM) of the single and double pulse welds subjected to the paint bake cycle heat treatment revel the presence of ε-carbide within lath martensite microstructure. The cross tension strength of both single and double pulse welds subjected to the paint bake cycle increase. The fracture toughness measurement using digital image correlation (DIC) of the simulated martensitic and tempered martensite (subjected to the bake cycle) shows that the CTOD of tempered martensite is considerably higher than a non-tempered martensitic microstructure.

The residual stress of single and double pulse welds was measured using synchrotron X-ray diffraction and simulated using the Simufact platform. The experimental and simulated results showed a tensile stress in the weld nugget due to the molten nugget solidification shrinkage and thermal contraction at the end of the weld cycle. The HAZ also exhibited a tensile stress mode due to the contraction. The base material showed compressive residual stresses near the weld to maintain stress equilibrium in the work piece. Further from the weld, stresses are relatively low and approach zero at the edge of the work piece. The residual stress is also measured using FIB ring-core milling, which reveals a tensile residual strain at the weld edge. The residual stresses of a double pulse weld are lower than a single pulse weld. Moreover, applying a typical paint bake cycle reduces the residual stresses at the weld edge of the spot welds. Furthermore, the constructed and validated finite element model can be utilised in residual stress prediction of the spot welds.

The effect of mechanical loading *i.e.* electrode load in resistance spot welding on the solid-state phase transformation of the AHSS is fundamentally studied using synchrotron X-ray diffraction and the results show that the mechanical load affects the martensite start temperature (Ms) and the amount of retained austenite in the samples. Applying stresses lower than the yield stress of the material, increases Ms, conversely applying loads higher than the yield stress decreases Ms, possibly due to an increase in austenite dislocation density, change in morphology and carbon enrichment. The samples subjected to higher loads show higher retained austenite volume fractions and a larger retained austenite lattice parameter as a result of change in austenite morphology and austenite carbon enrichment. In this research, the mechanical performance of the resistance spot welds of the AHSS studied is improved with an application of double pulse welding followed by a paint bake cycle.

Samenvatting

Het potentieel ten aanzien van gewichtsreductie, fabricagegemak en verbeterde crashbestendigheid maakt geavanceerde en ultra-hoge-sterke staalsoorten (AHSS en UHSS) aantrekkelijk voor automobieltoepassingen. Weerstandspuntlassen is veruit de meest gebruikte verbindingsmethode in de automobielindustrie vanwege de hoge bedrijfssnelheden, de betrouwbaarheid van het proces en de geschiktheid voor automatisering. Om acceptatie van weerstandpuntlassen van deze staalsoorten in de automobielindustrie te verzekeren, moeten 'veilige' microstructuren worden gecreëerd. Het hogere legeringsgehalte in beide hoge-sterkte staalsoorten beperkt de lasbaarheid en ongunstige faalmodes worden regelmatig waargenomen.

Het belangrijkste doel van dit onderzoek is het identificeren en begrijpen van de oorzaken voor dit ongunstige faalgedrag van de lassen in deze staalsoorten. Met de opgebouwde kennis kan de microstructuur en dus de mechanische respons van de lassen worden verbeterd. In dit proefschrift worden de resultaten van alternatieve lasschema's voor het modificeren van de microstructuur en de mechanische eigenschappen van de AHSS-weerstandspuntlassen gerapporteerd. Tevens zijn de effecten van een 'paint-bake' cyclus op de microstructuur van de lassen onderzocht. Restspanningen in en rond de lassen zijn gemeten. Een thermo-mechanisch model is geconstrueerd om de effecten van de lasschema's en warmtebehandeling op de restspanning te voorspelling.

Weerstandspuntlassen met een tweede stroompuls met verschillende stroomsterkte-niveaus is toegepast om de microstructuur aan de rand van de las te verbeteren. Een tweede stroompuls gelijk aan de eerste puls geeft een warmtebehandeling van de laszone en modificeert daardoor de microstructuur. De microstructurele analyse is uitgevoerd met behulp van optische microscopie, scanning elektronenmicroscopie, elektronen probe microanalyse (EPMA) en elektron backscattering diffractie (EBSD). Een dubbele puls met gelijke stroomsterkte resulteert in een vermindering in segregatie van legeringselementen, zoals bijvoorbeeld fosfor, een verandering in korrelmorfologie van dendritisch naar een meer equi-axed vorm en tevens een kleinere korrelgrootte. De resultaten verkregen uit de mechanische beproevingen, zijnde cross tension strength (CTS) en tensile shear strength testen (TSS), laten een verbeterde CTS sterkte en hogere energie-absorptievermogen van de las zien als een dubbel pulslasschema wordt toegepast.

Het effect van een typische 'paint-bake' cyclus op de microstructuur en de mechanische respons van de conventionele en dubbele pulslasschema's na het lassen is onderzocht. De 'paint-bake' cyclus bestaat uit een warmtebehandeling op ongeveer 180 °C, gedurende 20 minuten. Het microstructuuronderzoek met behulp van transmissie-elektronenmicroscopie (TEM) van de conventionele en dubbele pulslasschema's die zijn onderworpen aan deze warmtebehandeling tonen de aanwezigheid van e-carbide in de martensitische microstructuur. Hierdoor neemt de cross tension sterkte van zowel de

conventionele als de dubbele pulslassen toe. Breuktaaiheidsmetingen met behulp van digital image correlation (DIC) van de martensitische en getemperde martensitische structuur (onderworpen aan de 'paint-bake' cyclus) geeft aan dat de Crack Tip Opening Displacement (CTOD) van getemperd martensiet aanzienlijk hoger is dan van een niet-getemperde martensitische microstructuur.

De restspanning van conventionele en dubbele pulslassen is gemeten met behulp van synchrotron röntgendiffractie. De spanningsontwikkeling is gemodelleerd met behulp van het Simufact-platform. De experimentele en gesimuleerde resultaten tonen een trekspanning in de gestolde las als gevolg van de stollingskrimp en thermische contractie tijdens verder afkoelen. In de warmtebeïnvloede zone (WBZ) worden ook trekspanningen waargenomen als gevolg van de contractie. In het basismateriaal ontstaan drukspanningen nabij de las om het spanningsevenwicht in het werkstuk te handhaven. Verder weg van de las zijn de spanningen relatief laag en naderen nul aan de rand van het werkstuk. De restspanning is ook gemeten met behulp van FIB-ring core milling. Ook hieruit blijkt dat een trekspanning aanwezig is aan de rand van de las. De restspanningen van een dubbele puntlas zijn lager dan die van een conventionele lascyclus. Bovendien vermindert het toepassen van de 'paint-bake' cyclus het restspanningsniveau aan de rand van de puntlassen. Het geconstrueerde en gevalideerde eindige-elementen thermo-mechanische model is gebruikt voor het voorspellen van de restspanningen onder deze condities.

Het effect van mechanische belasting, dat wil zeggen de elektrode-aandrukkracht bij het weerstandspuntlassen op de fase-transformatie in de vaste stof van de AHS staalsoorten, is bestudeerd met behulp van synchrotron röntgendiffractie en de resultaten tonen aan dat de opgelegde mechanische belasting de martensiet-starttemperatuur (Ms) en de hoeveelheid restausteniet beïnvloedt. Het aanbrengen van spanningen lager dan de vloeispanning van het materiaal verhoogt Ms, terwijl bij belastingen hoger zijn dan de vloeispanning Ms vermindert. Dit is mogelijk het gevolg van een toename in dislocatiedichtheid in het austeniet, de verandering in korrelmorfologie en de verrijking van het austeniet met koolstof. De proefstukken onderworpen aan hogere belastingen vertonen hogere volumefracties restausteniet en een grotere roosterparameter van het restausteniet. In dit onderzoek komt naar voren dat het mechanische gedrag van de bestudeerde puntlassen van de hogesterkte staalsoorten verbetert met het toepassen van een dubbel puntlasschema gevolgd door een 'paint bake' cyclus.

Acknowledgement

List of Publications

Journal papers:

- P. Eftekharimilani, E.M. van der Aa, R. Petrov, M.J.M. Hermans, I.M. Richardson, *"Understanding the effect of a paint bake cycle on the microstructure- mechanical properties relationship of a resistance spot welded advanced high strength steel",* Metallurgical and Materials Transactions A, Vol. 49A, 2018, 6185-6196.
- P. Eftekharimilani, R.M. Huizenga, B. Kim, A. Bernasconi and M.J.M. Hermans, *"In-situ synchrotron X-ray diffraction studies on effects of plastic and elastic loading on bcc phase transformations of a 3rd generation 1 GPa advanced high strength steel",* Metallurgical and Materials Transactions A, 2017, Vol. 49A, 78-87.
- P. Eftekharimilani, E.M. van der Aa, M.J.M. Hermans, I.M. Richardson, *"The microstructural evolution and elemental distribution of a 3rd generation 1 GPa advanced high strength steel during double pulse resistance spot welding",* Welding in the World, 2017, Vol. 61(4), 691-701.
- P. Eftekharimilani, E.M. van der Aa, M.J.M. Hermans, I.M. Richardson, *"Microstructural characterisation of double pulse resistance spot welded Advanced High Strength Steel",* Science and Technology of Welding and Joining Journal, 2017, Vol. 22, No. 7, 545–554.

Conference presentation and proceedings

- P. Eftekharimilani, H. Gao, R.M. Huizenga, E.M. van der Aa, M. Amirthalingham, I.M. Richardson, M.J.M. Hermans, *"Residual stress measurements and model validation of single and double pulse resistance spot welded advanced high strength steel",* The 12th International Seminar "Numerical Analysis of Weldability", 23-26 Sep. 2018, Graz, Austria.
- P. Eftekharimilani, R.M. Huizenga, M.J.M. Hermans, I.M. Richardson, *"Investigation of residual stress distribution in a resistance spot welded 3rd generation Advanced High Strength Steel",* International Institute of Welding (Annual Assembly), July 15-20 2018, Bali, Indonesia.
- P. Eftekharimilani, B. Kim, R.M. Huizenga, M.J.M. Hermans, *"In-situ Synchrotron X-ray Diffraction Studies on Effects of Loading on bcc Phase Transformations of a 3rd Generation 1 GPa Advanced High Strength Steel"*, International Conference On Martensitic Transformations (ICOMAT), July 9-14 2017, Chicago, IL.
- P. Eftekharimilani, E.M. van der Aa, M.J.M. Hermans, I.M. Richardson, *"Effects of low-temperature post-weld heat treatment on microstructure and mechanical properties of a double pulse welded advanced high strength steel"*, International Institute of Welding (Annual Assembly), June 25-30 2017, Shanghai, China.
- P. Eftekharimilani, E.M. van der Aa, M.J.M. Hermans, I.M. Richardson, *"The microstructural evolution and elemental distribution of an advanced high strength steel during double pulse spot welding"*, International Institute of Welding (Annual Assembly), July 2016, Melbourne, Australia.
- P. Eftekharimilani, E.M. van der Aa, M. Amirthalingam, M.J.M. Hermans, I.M. Richardson, *"Effect of double pulsing on the microstructural evolution of low alloyed and 3rd generation 1 GPa advanced high strength steels during resistance spot welding"*, 9th International Seminar & Conference on Advances in Resistance Welding, April 12-15 2016, Florida, US.

About the author

Parisa was born on September 20, 1990 in Tabriz, Iran. After graduating with a high school diploma in mathematics and physics in 2008, she started the bachelor's program Metallurgy and Materials Engineering at the University of Tehran. She received her B.Sc. degree in September 2012 and entered to the M.Sc. program in Materials Science and Engineering at the University of Tehran. She completed her M.Sc. in September 2014 with a thesis on the preparation and characterization of Al matrix composites via Flake Powder Metallurgy (FPM).

In April 2015, she started her doctoral research entitled "Towards intrinsically safe microstructures in resistance spot welded advanced and ultra high strength automotive steels" in the Materials Science and Engineering (MSE) Department of Delft University of Technology (TU Delft). She has published several manuscripts in peer review journals and conference proceedings. From April 2019, she started to work at ASML.